An Integrated Framework for Image Acquisition, Processing, and Analysis Procedure for Automated Damage Evaluation of Concrete Surface

Haixu Zhang

Under supervision of:

Dr. Leandro F. M. Sanchez

Thesis submitted to the University of Ottawa in partial Fulfillment of

the requirements for the degree of

MASTER OF APPLIED SCIENCE

in Civil Engineering

Department of Civil Engineering

Faculty of Engineering

University of Ottawa

Abstract

In the last few decades, alkali-silica reaction (ASR) has been extensively discussed in numerous studies as a harmful distress mechanism that poses adverse effects to concrete structures. ASR can lead to the expansion of concrete members, resulting in the formation of cracks on their surfaces, loss in mechanical properties, and severe deformations. These cracks often serve as early indicators of structural degradation, making them crucial for condition assessments aimed at providing preliminary qualitative and quantitative damage extent results. Visual inspection, a commonly used and versatile technique, is employed to assess concrete degradation by visually detecting signs of damage on the surface. However, visual inspection tends to be qualitative and is therefore limited in providing accurate information regarding the extent of damage and its evolution. To address this limitation, researchers have introduced the Cracking Index (CI) as a crack mapping process capable of quantitatively assessing the extent of cracking on the surfaces of affected concrete members. Nevertheless, conventionally collecting data for CI calculation can be both time-consuming and reliant on the expertise of the operators, which can yield inaccurate results when applied in aggressive environments and/or within hard-to-access areas of a structure. To enhance the condition assessment process, the use of Artificial Intelligence (AI) can provide significant assistance by enabling automatic crack detection. However, to improve the performance of crack automating, it is imperative to intensively train a machine learning model, employing a substantial dataset of annotated images, and associated quantitative data. Questions remain regarding the required image quality and image collection methodology to ensure the model’s accuracy and reliability in crack detection. Therefore, this thesis introduces a comprehensive procedure for image acquisition and processing, further analyzing the outputs to explore the capabilities of damage diagnosis through the image-based crack measurement approach.

Keywords: *Condition assessment, Crack automation, Artificial intelligence (AI), alkali-silica reaction, concrete surface crack, Machine Learning, Cracking Index, Total Crack Length, Image analysis, Image processing.*

Acknowledgements

I wish to extend my heartfelt gratitude to my supervisor, Dr. Leandro Sanchez, for granting me the privilege to immerse myself in an extraordinary research environment. This experience has been nothing short of an enlightening journey, revealing to me what makes the consistency of science, shaping not only my academic endeavours but also my personal and professional growth.

I would also like to express my appreciation for my mentor, Cassandra Trottier. Cassandra's exceptional guidance and unwavering support have been the pillars of my academic journey. Whenever I found myself at a crossroads, uncertain of how to proceed, Cassandra provides guidance like a beacon of light, sparking my ideas and propelling me in the right direction. During challenging moments, her steadfast support has provided me with the confidence to overcome obstacles and continue my pursuit of excellence.

The team led by Dr. Sanchez, μStructure, has been nothing short of remarkable. This team was filled with outstanding and intelligent students who have not only offered unwavering support but have also served as a constant source of inspiration throughout this remarkable adventure. It has been an honor to witness the significant impact that these civil engineering students are making on the world.

Last but not least, I want to acknowledge two indispensable members of the University of Ottawa's Faculty of Civil Engineering: the technical officers (TOs) of the Materials and Structures Laboratory, Drs. Muslim Majeed and Gamal Elnabelsya. Their support was invaluable to ensure an efficient and safe work environment in the civil engineering lab.

Table of Content

List of Figures

List of Tables

Chapter 1 : Introduction

1.1. Synopsis

Among the various types of internal swelling reactions (ISR) that may affect concrete serviceability is the alkali-silica reaction (ASR), which is the most commonly reported type in Canada [1–3]. ASR is started from the chemical reaction between the alkali hydroxides (i.e., Na^+, K^+ and OH^-) from the pore solution and some unstable mineral phases (i.e., reactive silica) within the fine/coarse aggregates, further generate a gel form of production that can swells upon moisture uptake, leading to expansive pressure within the element. Cracks therefore begin from within the concrete and develop into macro cracks on its surface [4]. Cracks are a common type of deleterious damage that frequently appears on concrete surfaces, further increasing the concrete's permeability and allowing the ingress of harmful agents (i.e., water, de-icing salts, etc.). Unlike other defects, cracks can be readily visible, making them early indicators of potential damage in concrete structures. The crack monitoring over time leads to critical insights into the damage's progression, indicating the need for further investigation and/or intervention, since the presence of ASR can result in harmful distress of concrete mechanical properties, stiffness, serviceability, and durability [1]. Yet, assessing the presence and severity of cracks remains an initial step for evaluating the overall condition of the concrete from a structure [3].

Currently, the evaluation of concrete elements affected by ASR starts with a visual inspection process, aimed at qualitatively examining signs of deterioration on the surface. To perform a quantitative analysis of the damage extent, researchers have introduced a surface crack mapping technique known as the Cracking Index (CI). This non-destructive quantitative tool is utilized to assess the degree of damage thus estimating the concrete expansion by measuring the widths of cracks observed on the ASR-affected concrete surface [6,7]. To conduct the measurements of cracks towards the CI calculation, one begins by placing a square outline on the surface of the concrete element under investigation, by using a magnifying lens (e.g., 25x or 30x magnification) and a comparator card with graduations (e.g., 0.1mm to 1.5mm), the width of each crack is measured and recorded. The sum of crack widths that intersect the four lines of the square, expressed in millimeters per meter (mm/m), consists of the CI value [6]. However, the CI technique can be very subjective and sensitive to the inspector's experience, which can result in less accurate and less reliable assessments [7] notwithstanding its time-consuming and environment-sensitive nature (i.e., variability due to time of day, sunlight position, time of year, weather, overcast).

As such, image analysis techniques integrated with artificial intelligence (AI) have been increasingly proven efficient as a tool to capture such patterns on concrete surfaces. However, their application has been limited to qualitative assessments, such as crack identification without extending to the association with ASR damage or conducting a quantitative analysis of the observed damage in general [8,9]. Although the CI was developed as a practical tool decades ago, new technologies and the enhanced resolution obtained with conventional digital cameras allow the development of an automated procedure to capture ASR damage extent at the surface of a concrete element. However, existing research on crack automation models are mainly trained by datasets comprising a sufficient number of small-sized images (e.g., 336 x 339 pixels, 1cm x 1cm) that contain partial details of cracks [10–12]. CI aims to quantify damage by summarizing the crack measurements over a specific area (e.g., 25 cm x 25 cm, 0.5m x 0.5m). However, there is a shortage of datasets containing the required images to train machine learning models for quantifying the extent of cracking (i.e., minimal annotated datasets). Therefore, a rigorous protocol is essential to transform images into quantifiable features to advance recognition and damage quantification models.

1.2. Research Objectives and Scope of the Work

One of the main objectives of this study is to develop a flexible image acquisition and processing protocol to accommodate varying conditions (i.e., digital camera type and size of analyzed area). The ultimate goal is to facilitate a reliable quantitative evaluation of cracked concrete surfaces using image analysis. In this context, an image acquisition procedure will be established and serve as input precursor for machine learning (ML) training (e.g., Mask R-CNN[8]). The database of this project refers to annotated images capturing crack size at the concrete surface along with crack tracing to measure both the quantity and length of cracks. To ensure the reliability and quality of the training, images will be analyzed under different light conditions, crack quantifying approaches, and comparative assessments between manual and digital evaluations. It is imperative the data reflects known causes and extents of damage; therefore, images were taken from laboratory-made concrete blocks affected by ASR-induced damage within a controlled environment. These blocks have reached their optimum expansion level, as detailed in the study by Zahedi et al. (2021) [7]. In this current project, seven concrete blocks varying the reinforcement (i.e., plain concrete, 1 directional reinforcement, and 2 directional reinforcement) and ASR source (i.e., reactive coarse or fine aggregate) were used for data acquisition. Once the crack measurement data had been collected, the correlation between various outputs was performed. This included a comparison between the CI performed manually (i.e., ground truth) and CI derived from digital images. Additionally, characteristics of the crack pattern within the defined square boundary were evaluated, focusing on crack intensity (i.e., Total Crack Length as the total cracking length per unit analyzed area, mm/cm^2) and preferential crack orientation. Establishing appropriate metrics for quantitatively describing the damage extent when utilizing digital imaging techniques is crucial to developing reliable datasets through standardized image acquisition, processing, and annotation processes for further machine learning solutions when quantifying ASR damage.

1.3. Thesis Organization

This thesis is structured into four chapters and is presented in a paper-based format. The first chapter serves as an introduction to the fundamental concept of alkali-silica reaction (ASR) and provides an overview of current visual inspection methods and automated crack detection and quantification techniques. The second chapter entails a comprehensive literature review of ASR, covering studies from its occurrence to its consequences. Additionally, this chapter explores concrete condition assessment, detailing the protocol for visual inspection and its limitations, and proposes an AI-based solution to overcome such limitations. Furthermore, it drives into research related to the machine learning (ML) process of a crack automation algorithm. In the third chapter, the main topic is expanded, presented in a paper format providing a detailed procedure for collecting images from sample concrete surfaces and processing them into a format easily adapted for image analysis purposes. It also discusses the results output to give an insight into the performance of image analysis regarding the concrete surface damage assessment. It showcases the necessary process of an automated crack detection and damage quantification model using AI and ML processes, emphasizing the importance of a standardized image acquisition and image processing. The final chapter serves as the conclusion of the thesis, summarizing the entire process and work conducted, highlights the contribution made toward to the first step into an automated crack detection and damage quantification system. The chapter also provides recommendations and suggestions for future work to overcome limitations and optimize the result outcome from the image further. The thesis concludes by offering valuable insights and providing recommendations for potential future advancements in the field of damage assessment through an image-based approach.

Chapter 2 : Background and Literature Review

Chapter 2 focuses on a series of research related to this thesis. It encompasses an investigation into the ASR mechanism, the influence of ASR on concrete properties, and the evaluation of existing concrete condition assessment methods associated with ASR. While conducting concrete condition assessments can offer a preliminary result into structural health based on crack analysis (i.e., tolerable crack widths), it is essential to acknowledge certain limitations concerning operational efficiency and result reliability. Thus, the chapter delves into the domain of artificial intelligence (AI) technology and machine learning (ML), exploring recent works and approaches pertaining to concrete crack detection.

2.1. Alkali-Aggregate Reaction in Concrete

2.1.1. Introduction to AAR

Alkali-aggregate reaction (AAR) is a chemical process that occurs between the alkali hydroxide from the concrete pore solution and specific types of mineral phases from aggregates. Two types of AAR can potentially harm concrete structures: alkali-silica reaction (ASR) and alkali-carbonate reaction (ACR) [1,2]. The phenomenon of ASR was first recognized by T.E. Standon in 1940 [13], who noticed cracking and other forms of damage in concrete structures that contained certain types of aggregates. Since then, ASR has been widely recognized and studied in United States structures built during the 1940s and subjected to extensive research in concrete durability problems [13]. ASR is a physicochemical reaction between alkali hydroxides (i.e., Na+, K+, OH-) from the concrete pore solution and certain unstable silica mineral phases found in fine or coarse aggregates. As shown in Figure 2.1 [3], ASR produces a hygroscopic secondary reaction product often referred to as “gel” that swells upon absorbing water, leading to expansion, exceeding the tensile strength of the concrete and causing significant damage to concrete structures through cracking. In contrast, ACR represents another harmful chemical reaction associated with carbonate rocks. Its mechanisms are less understood and are less common compared to ASR. As such, this thesis will only describe ASR.

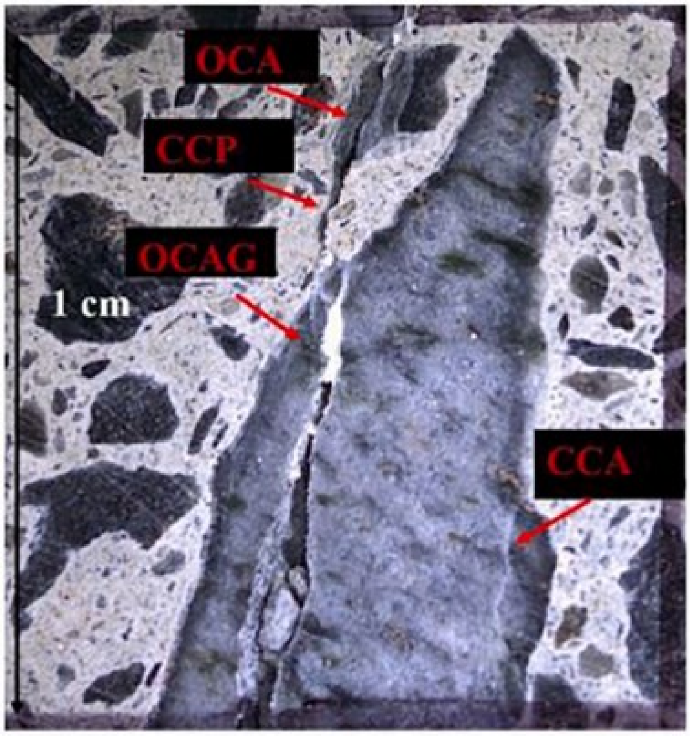

Figure 2.1: Concrete cracks filled with products of ASR within the aggregate were labeled as an open crack in the aggregate with "gel" - OCAG (white color) [3]. Micrograph of 1 cm^2.

Typically, the extent of ASR-related concrete damage is gauged by its volumetric expansion. While the correlation between expansion and deterioration isn't always direct, it's generally believed that greater expansion signifies more pronounced degradation, including reduced mechanical properties, structural integrity, and rigidity. Sanchez et al. (2014) has developed a qualitative model (Figure 2.2) to describe the damage generation and propagation caused by ASR [1]. At low levels of expansion (0.05%), sharp (A), onion-skin-like cracks can be observed within the reactive aggregate particles, represented as A and B in Figure 2.2 [1]. As the reaction progresses, not only the formation of new cracks within these aggregate particles appears, but more critically, the previously developed cracks undergo an increase in both length and width, notably occurring at moderate expansion levels, e.g., 0.12%, and potentially extending slightly into the cement paste. With the further development of ASR, these pre-existing cracks ultimately reach the cement paste at both ends of the aggregate, typically around 0.20% expansion, significantly compromising the physical integrity and mechanical properties of the affected material [1]. Lastly, at extremely high levels of expansion, like 0.30%, the cracks originating from various aggregate particles begin to interconnect, creating a substantial network of cracks within the affected concrete, this further lead to the reduction in durability and mechanical properties of concrete elements [20].

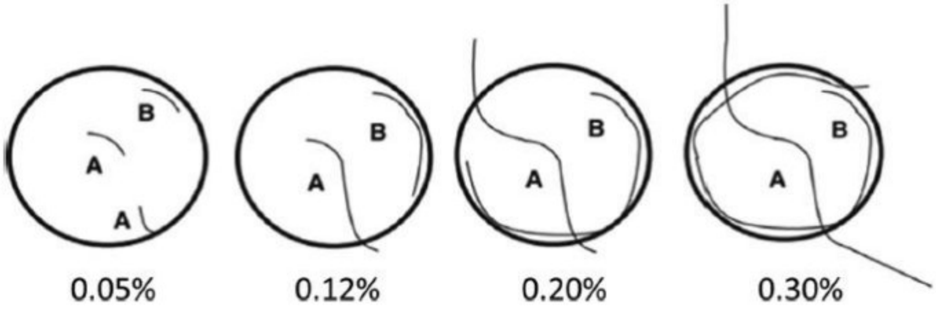

Figure 2.2：Descriptive ASR Damage propagation model [1].

2.1.2. Factors affecting ASR.

As shown in *Figure 2.3* [1], ASR development can be influenced by three essential factors. Each of these factors can act as a critical variable influencing the rate of concrete expansion when they are all present in a concrete element:

-Reactive silica phases in aggregates

-Alkali content from cementitious materials

-Presence of efficient moisture (e.g., > 80%)

Figure 2.3: Three essential elements to trigger AAR [1].

Silica minerals in aggregates are generally in a stable form, but there are exceptions. According to the Federal Highway Administration (FHWA) report, many aggregate sources are not well-crystallized, examples include tridymite, acidic quartz volcanic glass, and basalt glass. These contain a high concentration of reactive silica and show a significant potential for ASR when exposed to highly alkaline solutions [5]. Reactive aggregate contains a form of silica minerals that is often amorphous, many lattices defect or exists in a poor crystalline state, which creates more surface area that can chemically react than crystalline forms of silica [1,14].

The formation of ASR gel in concrete is influenced by the quantity and kind of reactive silica, as well as the concentration of alkali hydroxide in the concrete's pore solution. Alkali hydroxides in the pore solution can react rapidly with the reactive forms of silica in the aggregate. As the reactivity of the aggregate increases, gel reaction products can be formed even with lower alkali concentrations [15,16]. If the alkali concentration is sufficiently high, the alkali hydroxides can even break the stronger silicon bonds found in less reactive aggregates to form the gel reaction product.

Moisture also facilitates the movement of alkali ions to reactive sites, and the formed gel can subsequently absorb water and leading to volume expansion. Moreover, repeated cycles of wetting and drying can amplify the alkali concentrations. As moisture transport through the concrete, dissolved alkalis move in the solution and remain when the moisture evaporates from the concrete surface. This phenomenon, known as alkali migration, can elevate the alkali concentrations on evaporative surfaces, resulting in more severe damage to the concrete's surface compared to its interior [1,14,17].

2.1.3 Loss of mechanical properties

The effects of ASR on mechanical properties have been extensively studied through numerous experimental and analytical studies [3,18,19]. Many of these investigations highlight the correlation between the degradation of concrete properties and expansion levels. In general, the volumetric expansion and cracking induced by ASR can lead to a significant reduction in the compressive strength, tensile strength, and modulus of elasticity of affected concrete. Consequently, all these effects can significantly compromise the serviceability and durability of concrete structures. Sanchez et al. (2014) has conducted a series of experiments to report the concrete mechanical property loss under ASR affection combining reactive aggregates, concrete qualities, and combined mechanisms [20].

In Figure 2.4, Sanchez et al. (2014) presented the result of mechanical properties reduction under free expansion condition for different 35 MPa mixtures combinations [1]. The compressive strength loss is approximately 10% at an expansion of 0.05%, rising to between 10% and 20% at

0.12% expansion, and then to 20% - 30% for expansions of 0.20% and above. Overall, with increasing expansion, the compressive strength of ASR-affected concrete shows a modest reduction at low to medium expansion levels (i.e., from 0.05% to 0.12%), and the reduction becomes significant at high expansion level (i.e., from 0.20% to > 0.30%).

Regarding the reduction in tensile strength, at a low expansion level of 0.05%, there's already a noticeable loss in tensile strength, showing reductions ranging from 15% to 70%. However, as the expansion level exceeds 0.12%, the reduction of tensile strength starts to stabilize, remaining relatively consistent until higher expansion levels.

For the 35 MPa mixtures, the modulus of elasticity reduction shows a gradual increase at a low expansion level (0.12%), with a broad range from 10% to 45%. However, as the expansion level rises to a high threshold (0.30%), the rate of reduction decelerates slightly, settling the modulus of elasticity reduction within a range from 40% to 65%.

These findings evidence that concrete exposed to ASR-induced expansion experiences a severer reduction in tensile strength and elastic modulus, especially at medium to low expansion levels (0.05% and 0.12%) when compared to the reduction in compressive strength. At high expansion levels (0.30% and above), all mechanical properties witness a substantial reduction yield to 60%. Moreover, the results above insights that mixtures containing different types of aggregate present a distinct influence (up to 30%) on mechanical properties under the same expansion level [1].

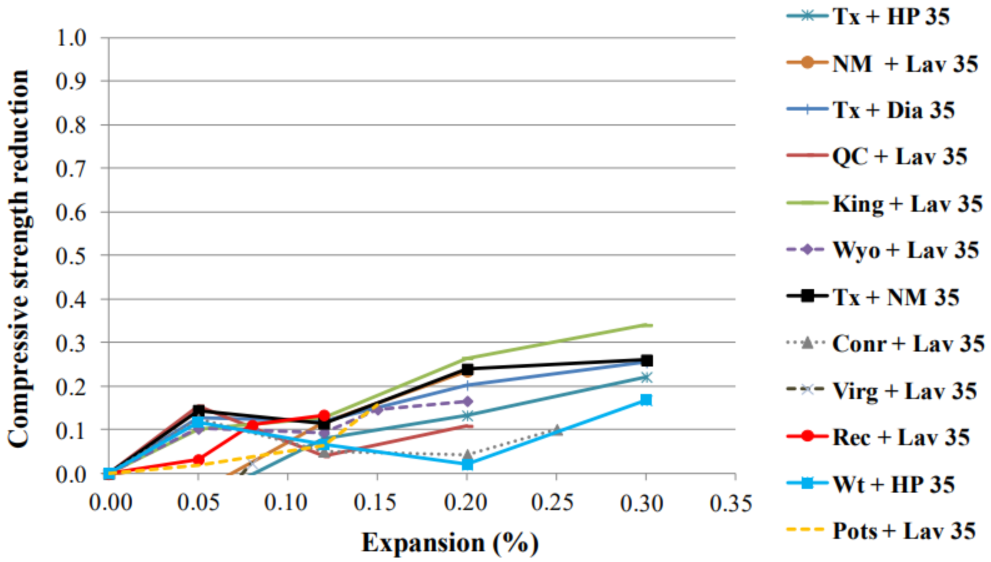
Compressive strength reduction
1.0
0.9
0.8
0.7
0.6
0.5
0.4
0.3
0.2
0.1
0.0
0.00
0.05
0.10
0.15
0.20
0.25
0.30
0.35
Expansion (%)
Tx + HP 35
NM + Lav 35
Tx + Dia 35
QC + Lav 35
King + Lav 35
Wyo + Lav 35
Tx + NM 35
Conr + Lav 35
Virg + Lav 35
Rec + Lav 35
Wt + HP 35
Pots + Lav 35

(a)

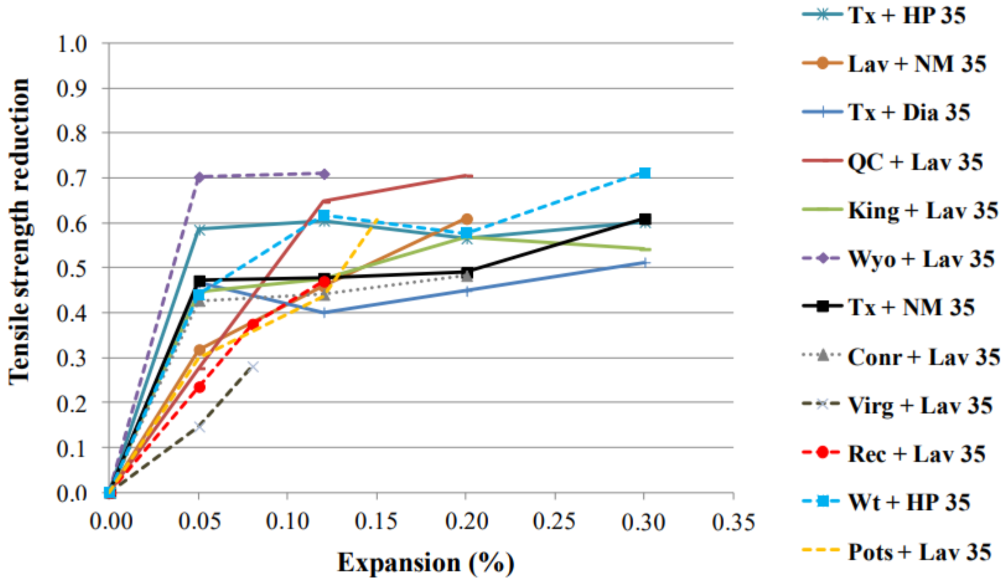
Tensile strength reduction
1.0
0.9
0.8
0.7
0.6
0.5
0.4
0.3
0.2
0.1
0.0
0.00
0.05
0.10
0.15
0.20
0.25
0.30
0.35
Expansion (%)
Tx + HP 35
Lav + NM 35
Tx + Dia 35
QC + Lav 35
King + Lav 35
Wyo + Lav 35
Tx + NM 35
Conr + Lav 35
Virg + Lav 35
Rec + Lav 35
Wt + HP 35
Pots + Lav 35

(b)

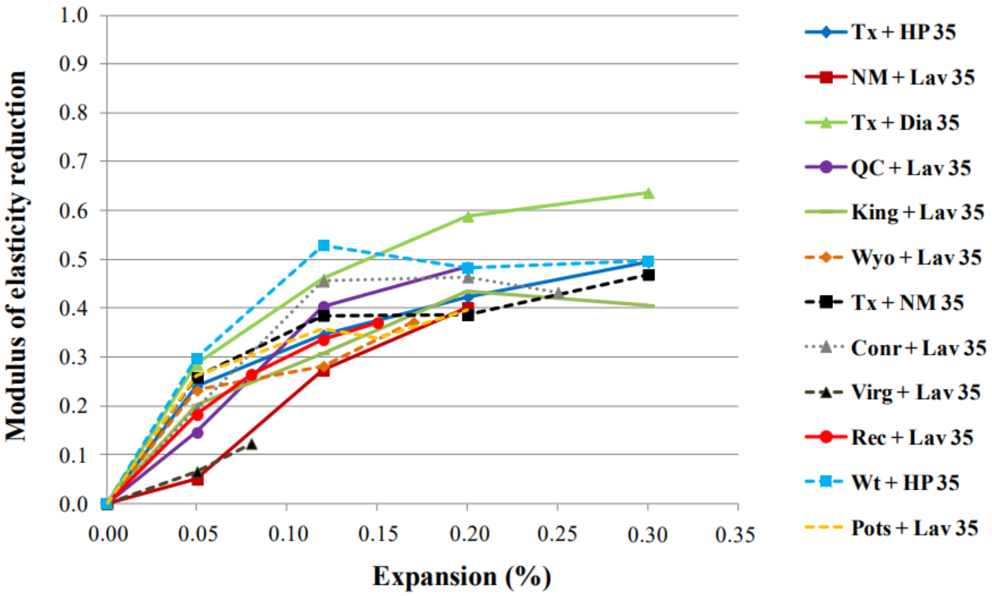

(c)

Figure 2.4: Mechanical properties loss due to ASR for 35 MPa concrete mixtures [1].

2.1.4. Macro consequence of ASR on concrete structures

ASR has become a typical threat to many existing concrete structures in terms of long-term durability [3,18]. Figure 2.5 [3,15] depicts damaged concrete elements severely affected by ASR. In addition to affecting the mechanical properties of concrete elements, ASR also can cause permanent deformation, cracking, spalling, extrusion of joint materials, and 'ASR gel' exudation. According to CSA A864-00 (2005) [21], ASR begins with the presence of a minimal amount of 'ASR gel' . As ASR progresses to moderate or significant levels, surface-level cracking and micro-cracking become evident, along with the darkening of the cement paste around known reactive aggregate particles. In severely affected concrete, expansion induced by swelling pressure can be positively identified at locations ASR-gel emanates from aggregates that have reacted and cracked, extending into the adjacent cement paste, signification amount of gel can be observed in cracks and spaces associated with reactive aggregate particles, either with the corrected-to-normal vision or minimal magnification.

Figure 2.5: Typical ASR damaged concrete element with presence of spalling, deformation, joint closing, map cracking with the presence of gel product [3].

Recent studies have specifically focused on the impact of ASR on critical infrastructure elements, including concrete dams and bridges [18,22,23]. In the mid-1980s, both Canada and the United States discovered that the Mactaquac Dam in New Brunswick, Canada, which had been commissioned for hydroelectric power generation in the 1960s, had been adversely affected by ASR. Millions of dollars are spent annually to reduce the expansion and prolong the service life of the dam since the discovery of ASRin the concrete material of the dam [24]. Consequently, the decision was made to decommission the dam due to the prohibitive cost of repairs. Notably, the Mactaquac Dam has experienced an expansion in height of approximately 230 mm since its initial construction in early 1980s, and extensive cracks can be observed throughout the entire structure (Figure 2.6). The dam has since been the subject of the “Life Achievement” project aiming to achieve its intended 100-year service life [24].

Figure 2.6 : Mactaquac Dam in New Brunswick, Canada affected by ASR [24].

The Robert-Bourassa/Charest (RBC) overpass, located in Quebec, Canada (*Figure 2.7*), was a highway bridge constructed in 1966 using alkali-silica reactive limestone aggregate. Over the past 50 years, the RBC's structural elements exhibited numerous damages, largely attributed to the effects of ASR and freeze-thaw cycles, including extensive steel corrosion and concrete delamination/spalling on the bridge deck, as well as map cracking, scaling, disintegration, and pop-outs on the massive concrete foundations of the reinforced concrete supporting columns. The overpass was commissioned for demolition in 2010/2011.

Researchers have conducted a multi-level assessment of the damage extent to various concrete elements demolished from RBC [3]. Compressive strength tests showed that a significant number of samples from foundation blocks and bridge decks had strength results lower than the expected design values, with stiffness loss up to 50%, compress strength loss up to 20%, and tensile strength loss up to 60%, raising concerns about the overpass's integrity to bear service loads as designed and in accordance with Canadian standards and safety protocols.

Figure 2.7: Robert-Bourassa/Charest (RBC) overpass affected by ASR in 50 years of service [3].

Such cases are most severe where map-cracking had appeared well before reaching this state of disrepair. Nevertheless, reliable and time-efficient monitoring techniques can indeed indicate volumetric expansions on their earlier on-site [18], where mitigation and rehabilitation strategies could be applied to counteract the effects of ASR on a concrete structure.

2.2. Condition assessment of ASR-Affected Concrete

Condition assessment is dedicated to employing experimental analyses to provide a comprehensive diagnosis and prognosis to evaluate the condition of the concrete element corresponding to a structure, including identifying the causes of concrete component damage, quantifying the extent of the damage, establishing current condition criteria, and predicting the structure's future performance [6] By gaining a thorough understanding of these aspects, it becomes possible to develop an improved strategy for structure rehabilitation and management [5]. Currently, various types of condition assessment methodologies have been proposed and advocated in studies including assessing the concrete damage affected by ASR [1,25,26]. For instance, the assessment process usually can start from visual inspection and non-destructive tests (NDT), some popular NDTs include Rebound/Schmidt hammer method, Ultrasonic pulse velocity (UPV) method, and Half-cell test [5,25]. These techniques allow an indirect property measurement through the surface of the concrete without causing damage to the tested elements. Moreover, the stiffness damage test (SDT) and damage rating index (DRI) belong to categories of multi-level assessment methods proposed by [1,20,27], that can evaluate the mechanism properties through core samples under laboratory experiments [27].

2.2.1. Current protocols and tools to detect damage at the surface of concrete.

2.2.1.1. Visual inspection

Visual inspection is one of the fundamental NDT methods that allow the evaluation of concrete components' condition and integrity by analyzing information collected from the appearance of damaged elements. It is usually performed periodically after the building construction throughout the building service life [26]. According to the visual inspection guidelines from ACI 201.1R-08

[28], a comprehensive visual inspection identifies visible signs of distress, damage, and deterioration (e.g., cracking, scaling, delamination, and disintegration). It provides information about the overall condition of the concrete structure, determines subsequent testing requirements, and recommends necessary maintenance and mitigation strategies [28].

The accuracy of visual inspection largely relies on the inspector's experience. When an inspector observes damage and deterioration in the concrete, the observations related to environmental exposure, durability, and performance must be properly documented, and review the concrete material records and construction practices as needed. However, while the guideline provides a checklist of visible defect signs that might indicate potential distress in the concrete, determining the exact extent of damage often requires support from NDT or destructive tests; the latter is especially true for concrete affected by ASR.

2.2.1.2. General appearance of cracking on concrete surface

The development and extent of surface cracking on concrete structures exposed to the elements, particularly in the case of concrete members affected by ASR, are influenced by various factors. When concrete undergoes internal expansion due to ASR, surface cracking can occur and may also have distinctive characteristics [29]. ASR-induced cracks, for instance, often exhibit a map-like pattern and may show signs of aggregate expansion through pop-outs and ASR gel formation leaching from the surface [30].

Cracking patterns or signatures observed at the surface of concrete can provide valuable information about the underlying distress mechanisms. Whether the distress is caused by external factors such as environmental exposure or internal factors like material properties or construction practices, different cracking patterns can be associated with specific mechanisms or a combination of multiple mechanisms. For example, shrinkage cracks are commonly observed in concrete due to the drying and volume reduction that occurs during the curing process. These cracks typically appear as hairline cracks and are often evenly distributed across the concrete surface [31]. On the other hand, loading cracks can result from excessive applied loads or structural overloading. These cracks may exhibit a more irregular pattern and can be wider and more prominent compared to shrinkage cracks [31]. The distinction between such cracks and cracks due to ASR is necessary to determine if the mechanism causing cracking is active or was a one-time event [14]. Such distinction can be a challenge upon a single inspection therefore, routine monitoring is necessary to capture the potential of cracking due to ASR. In some cases of large infrastructures such as bridges and dams which can be remote and at long distances from urban centers, opting for remote inspections can be an attractive replacement to routine monitoring however, limitations remain in such protocols which will be further discussed in the next sections.

2.2.1.3. Quantitative damage assessment method: Cracking index

The Cracking Index (CI) is a technique for mapping cracks that quantitatively evaluates the degree of surface cracking in structural concrete elements. This method includes measuring and summing the widths of cracks along lines that are drawn as square boundaries to the primary restraints on the concrete surface under examination [6]. Inspectors visually examine the concrete surface, measuring the width of cracks encountered along each grid line. The measured crack widths are then recorded and added together along each line, resulting in a cumulative crack width value for that specific line. The calculation for the cracking index is expressed by equation 2.1 which was proposed by a research report from Fournier et al. (2010) [6]:

$$CI = \frac{\sum Crack\ openings}{Base\ length} \qquad \text{Equation 2.1}$$

To perform the CI measurement, a square frame with four lines is created on the severely damaged concrete surface. Typically, these lines are drawn parallel and perpendicular to the main restraint(s). The square is usually drawn as 0.5m by 0.5m on structure elements, and the size of the ROI frame can be adjusted for the smaller damage area. As such, the spacing between the lines may vary depending on the size and complexity of the concrete element. To obtain a reliable assessment of cracking using the CI method, it is recommended to create multiple CI reference grids on the surface of the most severely cracked structural components [6]. These components are typically the ones exposed to moisture and harsh environmental conditions, as well as areas where ASR is expected to have occurred to a significant degree.

As shown in Figure 2.8, each CI reference grid should contain a “measurable amount of cracking”. These grids serve as visual reference points for quantifying and documenting the extent of cracking in the concrete structure. By strategically placing the reference grids on the most affected areas, a quantifying evaluation can be conducted to assess the severity of cracking. To measure the width of cracks on the surface of the investigated element, a magnifying lens with a plastic crack comparator card is required for precision. Each line drawn on the surface should be divided by 10 intervals as reference points and tabulating the crack amount and width in 10 steps for each side, this is to help the measurement can be documented correctly and efficiently.

Figure 2.8: A typical cracking index layout on a concrete surface using a 3D-printed reference grid.

The CI measurement method allows for a systematic and less-objective evaluation of the extent of cracking in concrete elements when compared to descriptive analysis. It provides valuable information for assessing the condition and performance of the structure, aiding in the determination of appropriate maintenance, repair, or rehabilitation measures [6,7]. As the protocol suggested, after carefully examining the cracks and obtaining the measurement, the following criteria can be purposed as a reference to justify for further investigation: the CI measured on the most exposed concrete component, which typically represents the most severe signs of deterioration from ASR, it also can provide a rough estimate of the expansion experienced by the element under investigation.

The CI was however developed as a practical tool to assess damage to concrete caused by ASR in which crack widths along straight lines can easily be measured. Although the CI does allow for directional interpretation of the results by providing a value for cracks parallel and perpendicular to the reinforcements, it remains a 1-directional analysis where widths of cracks are measured along lines. Measuring crack orientation and total crack lengths between the boundaries of the CI square remains a challenge on the field in practice therefore, a shift towards digitizing the images and applying image analysis techniques to improve time and objectivity of the crack quantification result is necessary. Although the surface cracking may appear as severe yet internally, the concrete is sound and vice-versa [3] this does not inhibit the development of a standardized protocol for image acquisition, processing, and analysis such that various parameters can further be used in combination with internal damage data (i.e., multi-level assessment) to provide more a reliable diagnosis. Without such established and standardized approaches, condition assessments will remain subjective and could result in inaccurate diagnoses, misdiagnoses or capturing an active mechanism in a later stage at which mitigation, rehabilitation and repair can become inefficient and more costly.

2.3. Automated crack detection techniques through machine learning (ML)

Various studies have highlighted that traditional manual inspection, while esteemed for crack detection, suffers from limited efficiency and a lack of quantitative analysis for evaluating structural conditions [11,12,32]. As a result, automatic image-based crack detection emerges as a replacement for effective non-destructive testing. This section will delve into several existing machine learning techniques present in the literature, examining both current challenges and achievements within the automatic crack detection field.

2.3.1. An Overview

Image analysis, in alignment with Artificial Intelligence (AI) and Machine Learning (ML), plays a significant role in various domains such as medical diagnosis, autonomous driving, object detection, and computer vision tasks [10,33]. In the field of civil engineering, there is a growing interest in crack detection as an efficient approach to inspect and monitor concrete structures and infrastructure. To overcome the limitations of human-based crack inspection methods, researchers are turning to automated crack detection techniques using machine learning algorithms [10,12,33]. Machine learning techniques, such as object classification and segmentation, are widely employed to identify and separate regions of interest within images. These techniques involve training a developed model with image datasets to accurately classify and separate specific objects or regions within the images[12].

The use of ML in object segmentation enables automation and efficiency in tasks that would otherwise require manual effort and expertise [10,34]. Munawar et al (2021). presents a basic architecture of ML for crack detection application as shown in Figure 2.9 [12]. Initially, a dataset containing surface cracks, intended for detection via the ML model, must be created. These images undergo preprocessing by using techniques in image processing to reduce noise, eliminate shadows, and adjust other properties like size and brightness. Subsequently, the cracks in these images undergo pixel-wise annotation or labeling, where defective pixels are marked in the image. This annotation step can be executed manually or through a labeling tool. One example of labeling involves setting crack pixels as white or "1" in the image while the rest are set as black or "0". After the model is trained by annotated images, another set of images will be input to the model to determine its capability in accurately classifying the regions containing cracks within the image [12]. ML techniques are crucial for developing an automated image-based crack detection system, which can effectively locate and quantify cracks on concrete surfaces, offering an efficient and cost-effective method for non-destructive concrete damage assessment.

Figure 2.9: Machine Learning Methods Schematic for Crack Detection [12].

2.3.2. Machine Learning (ML) models

A suitable ML model for crack detection is required to build the crack detection system, the review also identified several typical ML models has been proposed in studies such as Artificial neural networks (ANNs) [35].Different types of ML models address different methodologies to identify and extract information from the image along with object segmentation purposes. As shown in Figure 2.10 [10], classification can divide images into small patches, identifying and locating the presence of cracks from each small patch. However, classification (Figure 2.10 (a)) can only generate binary results of crack presence, lacking some important measurements, such as crack length, width, and count. Object detection (Figure 2.10 (b)) can create a bounding box involving the area where a crack exists, resulting in object categorization and quantification of different features based on annotated data input. Segmentation (Figure 2.10(c)) involves creating detailed pixel predictions of cracks in the image, where each pixel is classified as cracked or non-cracked. Segmentation can provide a precise description of fracture location and structure and has great significance for the classification and extraction of basic crack characteristics [10].

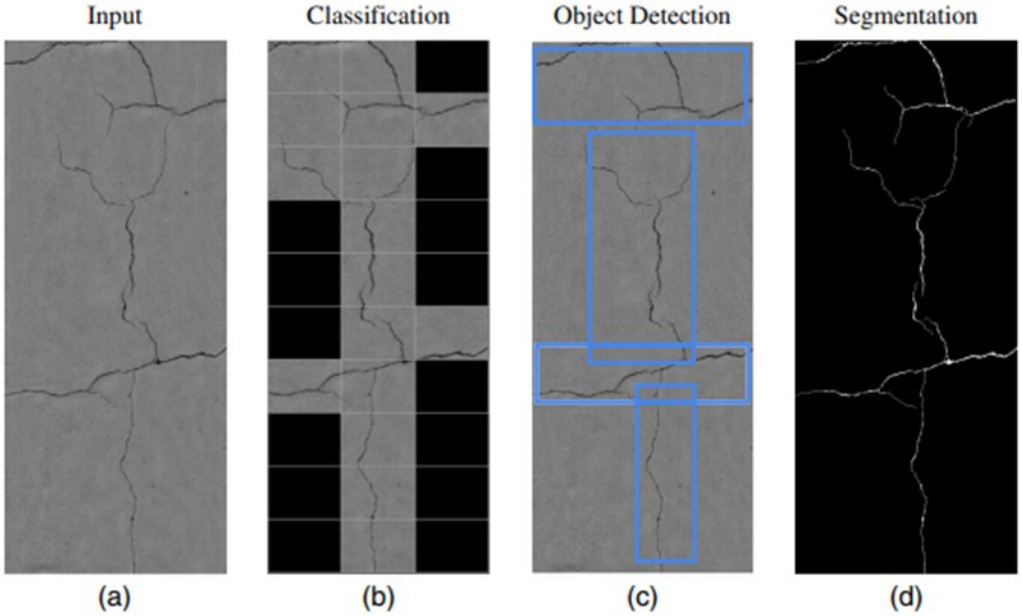

Figure 2.10: Different Deep Learning methods for crack identification and location: a) raw input, b) crack classification from sectional image grid. c) crack identification output. d) crack identified and measured at pixel level [10].

ANN were applied to address road condition-related issues such as defects and road roughness reconstruction as well as crack detection [36], the primary drawbacks of ANN methods include their slow training process, the complexity of designing the hidden layer and its nodes, which can lead to suboptimal results if the number of neurons is underestimated and their reduced performance in handling noisy data [37].

SVMs represent another supervised classification method. The fundamental concept of SVMs involves constructing a set of hyperplanes to classify data based on their distance from them [38]. Typically, a variety of potential settings are examined and cross-validated to determine the most suitable option for each problem. Consequently, SVMs exhibit low speed during the training phase [37]. Conversely, the complexity of the model remains unaffected by the number of features selected for the training phase, which constitutes a benefit of the method. SVMs are widely favored for binary classifications; however, they appear less suitable for the classification of multiple defects [10,36].

The most commonly model found in literatures is the Convolutional Neural Network (CNN) [33,39,40]. CNNs are deep learning algorithms that derived from ANNs, they are proficient and effective in image classification and object recognition. CNN incorporates more than one convolution operation, applying a feature detection layer to learn from training data. The CNN model consists of three layers of neurons: the convolutional layer, pooling layer, and fully connected layer. An optimized CNN model can execute the procedure that are implemented in the code to find patterns or make decisions effectively from a previously unseen dataset. CNNs have many types of variation and semantic segmentation networks proposed in research (i.e., CrackNet and Region-based CNN: R-CNN) [10,33]. A key advantage of CNN is their weight sharing mechanism, where neurons on the same feature mapping surface share the same weight, simplifying the feature extraction process [10,32,39]. Figure 2.11presents the general training process of CNN [40].

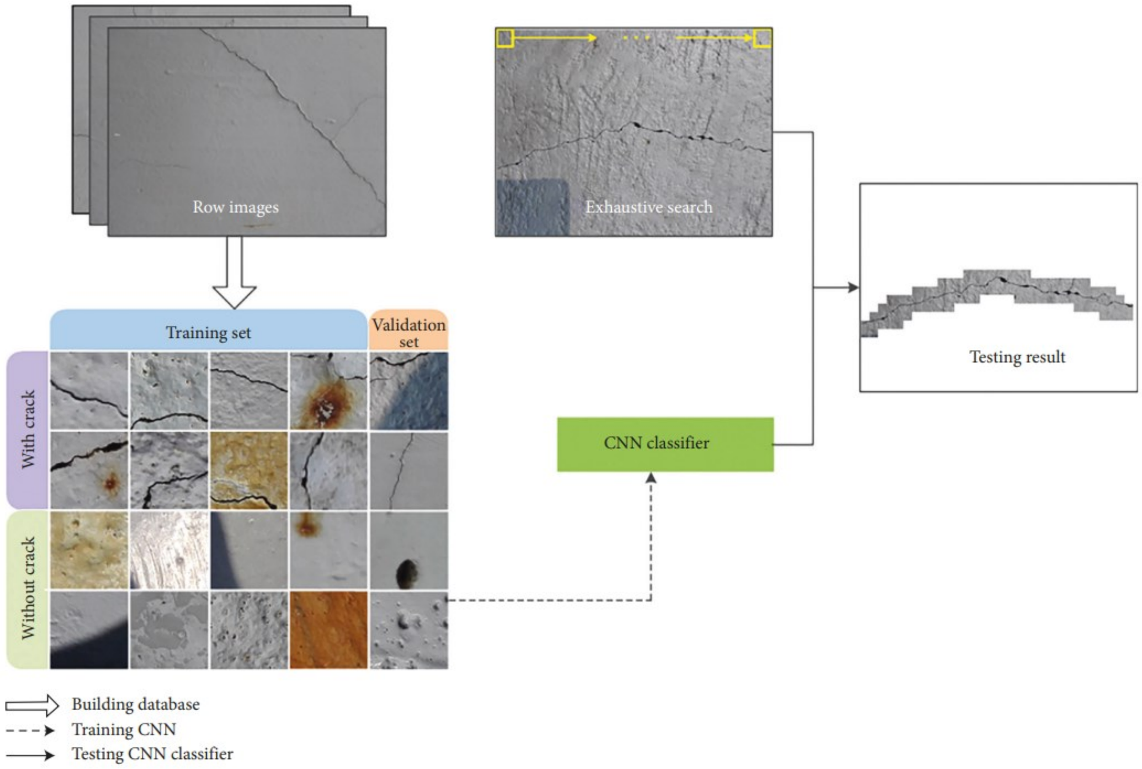

Figure 2.11: Flow chart for detecting cracks using a CNN [40].

2.3.3. Image dataset

The image dataset is essential for training and enhancing model performance. Mohan et al. (2015) [11] have identified that one of the main challenges in identifying concrete defects autonomously is to provide the machine with enough knowledge to identify the damage of concrete. While traditional datasets often comprise a collection of images displaying various crack patterns or segments from different surfaces (e.g., walls, pavement), the images lack processing and annotated information. This absence of annotation, especially when combined with potential issues in image quality, can compromise the accuracy of damage quantification. Kulkarni et al. (2022) highlighted this inconsistency in crack detection by benchmarking the R-CNN model against three datasets: AigleRN (38 images) [41], CFD dataset (118 images) [42], and the HTR dataset (134 images that are not available to public). As depicted in Figure 2.12 [42], the results highlight the inaccuracies that stem from training on unannotated images, potentially compromising the precision of damage estimation. Consequently, datasets enriched with crack annotations become a potential asset to address this limitation.

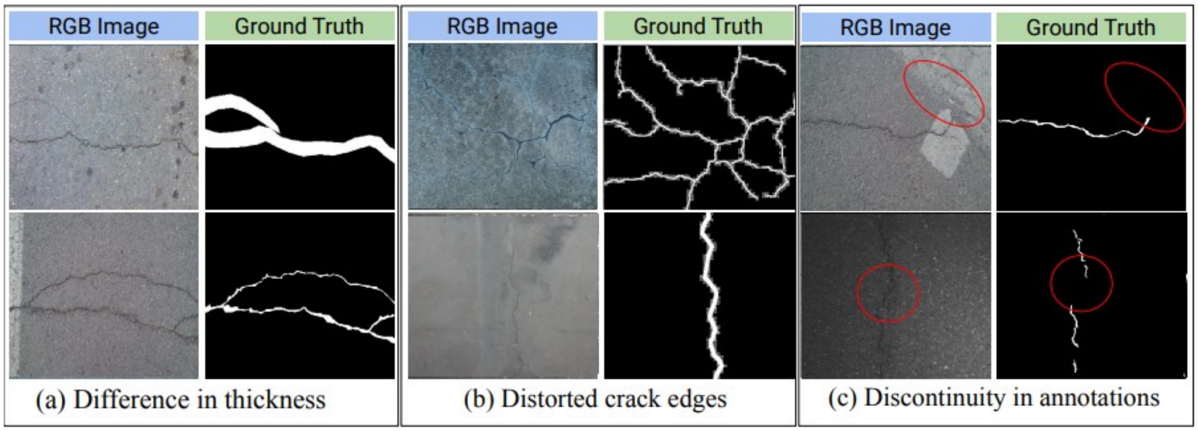

(a) Difference in thickness (b) Distorted crack edges (c) Discontinuity in annotations

Figure 2.12: Inconsistent crack detection result through a trained R-CNN model [43].

Notably, in the context of concrete damage caused by Alkali-Silica Reaction (ASR), there is a deficiency in available datasets, especially in terms of images required for proper machine training. Additionally, the quantification of damage based on crack characteristics faces challenges due to the lack of high resolutions images capable of capturing necessary features like visible crack openings in imaging. Nevertheless, with the increasing accessibility of such cameras, standardized datasets can be developed to further train ML models and advance the condition assessment protocols for ASR-affected concrete.

2.3.4. Crack segmentation through Machine Learning (ML) methods.

Many ML models have been developed and introduced in research literature, with many derived and enhanced from the Convolutional Neural Network (CNN) architecture. For image classification applications, CNNs take as input images with numerical values in each pixel, organized spatially along width, height, and depth, typically comprising three RGB layers. The main architecture is designed to generate a probability score indicating an image's classification into a specific class [40]. This is achieved by learning from the spatially arranged numerical values through operations such as pooling and convolutions. However, many existing CNN models such as AlexNet [44], VGG [45], GoogleNet [46], and ResNet [47] are primarily utilized for automated feature extraction for the classification of different types of objects in images. Deep learning frameworks like Faster R-CNN and YOLO have remarkable accuracy and speed in object detection tasks [48].

With the rapid advancement of deep learning, various attempts have been made to apply it to crack detection. Cha et al. (2017)[33] implemented a deep CNN architecture to detect cracks on concrete surfaces across different environmental variables; the trained network achieved accuracies of 98.22% with training by 322 high-resolution images. Zhang et al. (2016) proposed an automatic detection method for road maintenance called ConvNet [49], optimized based on D-CNN (Deep Convolutional Neural Network). It was trained using 500 pavement images of size 3264 x 2448, divided into 640,000 samples. The results demonstrated that the detection achieved a precision of 86.96%. However, these ML models are trained for binary class crack detection (Crack or Non-crack); they lack the potential for learning cracking segmentation.

Yang et al. (2018) trained an FCN model [50], an end-to-end, pixel-to-pixel convolutional network, for semantic segmentation. Utilizing over 800 images with resolutions ranging from 72 dpi to 300 dpi, the FCN demonstrates the capability to identify and segment intricate crack patterns with a precision level of 81.73%. However, the accuracy of predicting crack length and width for thin cracks falls below expectations, with relative errors ranging from -48.03% to 177.79% and -13.27% to 24.01%, respectively.

He et al. (2018) presents the Mask R-CNN, a variant of CNN that merges the functionalities of Faster R-CNN and FCN [51]. It has been noted since its architecture goes beyond the traditional object detection method and focuses on instance segmentation [8]. It has the potential to identify and delineate unique objects from the labeled data with bounding box annotations and pixel-level segmentation masks for each object. Kim et al. (2018) has introduced the architecture of Mask R-CNN consists of three main components as illustrated in Figure 2.13: a backbone network, a region proposal network (RPN), and a mask prediction network [8]. They trained the Mask R-CNN model using 376 images with varying resolutions but constrained within 2000 x 2000 pixels. There were 1,102 crack regions identified across these 376 images. To conserve storage space for training images, each image had a 50% probability of being horizontally flipped and a 50% probability of being vertically flipped during each iteration. Flipped images would be treated as new images for further training purposes. To evaluate the performance of the trained model, the crack detection results were validated by 73 images with resolution 6000 x 4000 pixels taken by a regular photography camera. Results showed that there were 453 cracks in total, but 103 cracks were missed in images. Fortunately, 84 of the 103 missed cracks were thinner than 0.1 mm, which is negligible for ASR evaluation. The literature has selected 10 points on the damaged concrete surface for crack width quantification analysis, with most points falling within the error of 0.054mm. However, 2 points with major errors at 0.154 mm and 0.254 mm may have been caused by noise from the surrounding environment. The paper suggests that employing higher resolution images or additional super-resolution techniques may help mitigate such errors.

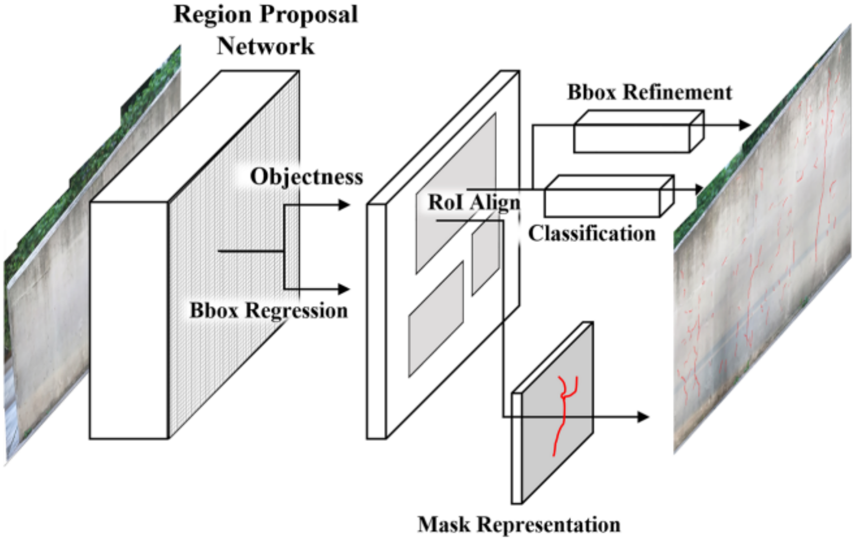

Figure 2.13: General architecture of Mast R-CNN [8].

There is a growing interest in image-based crack detection as a non-destructive testing (NDT) approach for assessing concrete conditions. These methods provide quantitative results, representing an improvement over inspections reliant solely on conventional visual approaches. Machine learning (ML) has emerged as a primary approach for automating crack detection, necessitating a significant input of raw images with varying crack features, as proposed in numerous studies [8,38,40]. Overall, the Mask R-CNN, as a novel crack detection method, demonstrated its advantages as an automated structural inspection approach. It requires a smaller database size while maintaining acceptable accuracy in crack detection and crack width quantification performance. The integration of the Mask R-CNN architecture is expected to optimize the image acquisition and processing procedure for automated crack quantification analysis.

2.4. Research Gaps and Objectives

Condition assessment is a methodology that remains essential for evaluating damage to concrete due to ASR and other forms of deterioration. Visual inspection is a commonly employed strategy, and when used effectively, it can provide descriptive, qualitative, and quantitative results that indicate the level of element deterioration. Yet, it presents some drawbacks in terms of efficiency, accuracy, and thus the reliability of the results, leading to their subjective interpretation. AI technology presents an efficient approach for conducting visual inspections. However, current research in crack detection lacks the capability to quantify the extent of damage. Typically, datasets containing images without annotated cracks are used primarily for qualitative analysis, which cannot be utilized for machine learning to ascertain the extent of damage. Therefore, the project proposes to follow two streams to enhance the use of the visual inspection technique: A) development of an image-based measurement procedure by utilizing conventional images to extract data representing ASR damage, and the creation of an image database for future model training; and B) evaluate the result output from image analysis, assessing the performance of damage quantification, taking into account other crack measurements that are often observed, especially in reinforced concrete members.

2.5. References

[1] L.F.M. Sanchez, Contribution to the assessment of damage in aging concrete infrastructures affected by alkali-aggregate reaction, Université Laval, 2014.

[2] E.O. Fanijo, J.T. Kolawole, A. Almakrab, Alkali-silica reaction (ASR) in concrete structures: Mechanisms, effects and evaluation test methods adopted in the United States, Case Studies in Construction Materials 15 (2021) e00563. https://doi.org/10.1016/j.cscm.2021.e00563.

[3] L.F.M. Sanchez, B. Fournier, D. Mitchell, J. Bastien, Condition assessment of an ASR-affected overpass after nearly 50 years in service, Construction and Building Materials 236 (2020) 117554. https://doi.org/10.1016/j.conbuildmat.2019.117554.

[4] M.D. Cohen, J. Olek, W.L. Dolch, Mechanism of plastic shrinkage cracking in portland cement and portland cement-silica fume paste and mortar, Cement and Concrete Research 20 (1990) 103–119. https://doi.org/10.1016/0008-8846(90)90121-D.

[5] A. Zahedi, C. Trottier, L.F.M. Sanchez, M. Noël, Condition assessment of alkali-silica reaction affected concrete under various confinement conditions incorporating fine and coarse reactive aggregates, Cement and Concrete Research 153 (2022) 106694. https://doi.org/10.1016/j.cemconres.2021.106694.

[6] B. Fournier, M.-A. Bérubé, M. Thomas, Report on the Diagnosis, Prognosis, and Mitigation of Alkali-Silica Reaction (ASR) in Transportation Structures, (2010) 156.

[7] A. Zahedi, L.F.M. Sanchez, M. Noël, Appraisal of visual inspection techniques to understand and describe ASR-induced development under distinct confinement conditions, Construction and Building Materials 323 (2022) 126549. https://doi.org/10.1016/j.conbuildmat.2022.126549.

[8] B. Kim, S. Cho, Image-based concrete crack assessment using mask and region-based convolutional neural network, Struct Control Health Monit (2019) e2381. https://doi.org/10.1002/stc.2381.

[9] F. Thériault, M. Noël, L.F.M. Sanchez, Simplified approach for quantitative inspections of concrete structures using digital image correlation, Engineering Structures 252 (2022) 113725. https://doi.org/10.1016/j.engstruct.2021.113725.

[10] Y.-A. Hsieh, Y.J. Tsai, Machine Learning for Crack Detection: Review and Model Performance Comparison, J. Comput. Civ. Eng. 34 (2020) 04020038. https://doi.org/10.1061/(ASCE)CP.1943-5487.0000918.

[11] A. Mohan, S. Poobal, Crack detection using image processing: A critical review and analysis, Alexandria Engineering Journal 57 (2018) 787–798. https://doi.org/10.1016/j.aej.2017.01.020.

[12] H.S. Munawar, A.W.A. Hammad, A. Haddad, C.A.P. Soares, S.T. Waller, Image-Based Crack Detection Methods: A Review, Infrastructures 6 (2021) 115. https://doi.org/10.3390/infrastructures6080115.

[13] T.E. Stanton, Expansion of Concrete through Reaction between Cement and Aggregate, T. Am. Soc. Civ. Eng. 107 (1942) 54–84. https://doi.org/10.1061/TACEAT.0005540.

[14] A. Zahedi, C. Trottier, L.F.M. Sanchez, M. Noël, Evaluation of the induced mechanical deterioration of alkali-silica reaction affected concrete under distinct confinement conditions through the Stiffness Damage Test, Cement and Concrete Composites 126 (2022) 104343. https://doi.org/10.1016/j.cemconcomp.2021.104343.

[15] J.A. Farny, B. Kerkhoff, Diagnosis and Control of Alkali-Aggregate Reactions in Concrete, (n.d.).

[16] M.T. de Grazia, Contribution to the understanding of fresh and hardened state properties of low cement concrete, University of Ottawa, 2018.

[17] S. Multon, F. Toutlemonde, Effect of moisture conditions and transfers on alkali silica reaction damaged structures, Cement and Concrete Research 40 (2010) 924–934. https://doi.org/10.1016/j.cemconres.2010.01.011.

[18] H. Ahmed, A. Zahedi, L.F.M. Sanchez, P.-L. Fecteau, Condition assessment of ASR-affected reinforced concrete columns after nearly 20 years in service, Construction and Building Materials 347 (2022) 128570. https://doi.org/10.1016/j.conbuildmat.2022.128570.

[19] N. Smaoui, M.-A. Bérubé, B. Fournier, B. Bissonnette, B. Durand, Evaluation of the expansion attained to date by concrete affected by alkali–silica reaction. Part I: Experimental study, Can. J. Civ. Eng. 31 (2004) 826–845. https://doi.org/10.1139/l04-051.

[20] L.F.M. Sanchez, T. Drimalas, B. Fournier, D. Mitchell, J. Bastien, Comprehensive damage assessment in concrete affected by different internal swelling reaction (ISR) mechanisms, Cement and Concrete Research 107 (2018) 284–303. https://doi.org/10.1016/j.cemconres.2018.02.017.

[21] CANADIAN STANDARDS ASSOCIATION, A864-00 (R2005): Guide to the Evaluation and Management of Concrete Structures Affected by Alkali-Aggregate Reaction, (2005).

[22] E. Fathalla, Y. Tanaka, K. Maekawa, Effect of Crack Orientation on Fatigue Life of Reinforced Concrete Bridge Decks, Applied Sciences 9 (2019) 1644. https://doi.org/10.3390/app9081644.

[23] L. Kristufek, A. Zahedi, D. Tawil, L. Sanchez, B. Martin-Perez, M. Noël, Preliminary evaluation of Pier cap from an ASR affected bridge in Central Canada, MATEC Web Conf. 364 (2022) 03005. https://doi.org/10.1051/matecconf/202236403005.

[24] P. Oke, Environmental Impact Assessment Registration: Mactaquac Life Achievement Project, (2023).

[25] P. Cotič, E. Niederleithinger, V. Bosiljkov, Z. Jagličič, NDT Data Fusion for the Enhancement of Defect Visualization in Concrete, KEM 569–570 (2013) 175–182. https://doi.org/10.4028/www.scientific.net/KEM.569-570.175.

[26] 221.1R-98 State-of-the-Art Report on Alkali-Aggregate Reactivity, (n.d.).

[27] L.F.M. Sanchez, B. Fournier, M. Jolin, J. Bastien, Evaluation of the stiffness damage test (SDT) as a tool for assessing damage in concrete due to ASR: Test loading and output responses for concretes incorporating fine or coarse reactive aggregates, Cement and Concrete Research 56 (2014) 213–229. https://doi.org/10.1016/j.cemconres.2013.11.003.

[28] J.P. Busel, Specification for carbon and glass fiber-reinforced polymer bar materials for concrete reinforcement, 1st ed, American Concrete Institute, Farmington Hills, MI, 2008.

[29] C. Trottier, R. Ziapour, A. Zahedi, L.F.M. Sanchez, F. Locati, Microscopic characterization of alkali-silica reaction (ASR) affected recycled concrete mixtures induced by reactive coarse and fine aggregates, Cement and Concrete Research 144 (2021) 106426. https://doi.org/10.1016/j.cemconres.2021.106426.

[30] L.F.M. Sanchez, B. Fournier, T. Drimalas, J. Bastien, D. Mitchell, M. Noel, SEMI-QUANTITATIVE CONDITION ASSESSMENT OF CONCRETE DISTRESS THROUGH THE DAMAGE RATING INDEX, (n.d.).

[31] M.A. El-Reedy, Assessment, evaluation, and repair of concrete, steel, and offshore structures, First edition, CRC Press, Boca Raton, FL, 2019.
[32] C. Koch, K. Georgieva, V. Kasireddy, B. Akinci, P. Fieguth, A review on computer vision based defect detection and condition assessment of concrete and asphalt civil infrastructure, Advanced Engineering Informatics 29 (2015) 196–210. https://doi.org/10.1016/j.aei.2015.01.008.
[33] Y.-J. Cha, W. Choi, O. Büyüköztürk, Deep Learning-Based Crack Damage Detection Using Convolutional Neural Networks: Deep learning-based crack damage detection using CNNs, Computer-Aided Civil and Infrastructure Engineering 32 (2017) 361–378. https://doi.org/10.1111/mice.12263.
[34] U.H. Billah, A. Tavakkoli, H.M. La, Concrete Crack Pixel Classification Using an Encoder Decoder Based Deep Learning Architecture, in: G. Bebis, R. Boyle, B. Parvin, D. Koracin, D. Ushizima, S. Chai, S. Sueda, X. Lin, A. Lu, D. Thalmann, C. Wang, P. Xu (Eds.), Advances in Visual Computing, Springer International Publishing, Cham, 2019: pp. 593–604. https://doi.org/10.1007/978-3-030-33720-9_46.
[35] S. Kabir, Imaging-based detection of AAR induced map-crack damage in concrete structure, NDT & E International 43 (2010) 461–469. https://doi.org/10.1016/j.ndteint.2010.04.007.
[36] S.C. Radopoulou, I. Brilakis, Automated Detection of Multiple Pavement Defects, J. Comput. Civ. Eng. 31 (2017) 04016057. https://doi.org/10.1061/(ASCE)CP.1943-5487.0000623.
[37] S.B. Kotsiantis, Supervised Machine Learning: A Review of Classification Techniques, (n.d.).
[38] X. Wu, V. Kumar, J. Ross Quinlan, J. Ghosh, Q. Yang, H. Motoda, G.J. McLachlan, A. Ng, B. Liu, P.S. Yu, Z.-H. Zhou, M. Steinbach, D.J. Hand, D. Steinberg, Top 10 algorithms in data mining, Knowl Inf Syst 14 (2008) 1–37. https://doi.org/10.1007/s10115-007-0114-2.
[39] P. Savino, F. Tondolo, Automated classification of civil structure defects based on convolutional neural network, Front. Struct. Civ. Eng. 15 (2021) 305–317. https://doi.org/10.1007/s11709-021-0725-9.
[40] S. Li, X. Zhao, Image-Based Concrete Crack Detection Using Convolutional Neural Network and Exhaustive Search Technique, Advances in Civil Engineering 2019 (2019) 1–12. https://doi.org/10.1155/2019/6520620.
[41] Chambo, S, Results with AigleRN images, (n.d.). https://www.irit.fr/~Sylvie.Chambon/AigleRN.html.
[42] A. Ahmadi, S. Khalesi, M. Bagheri, Automatic road crack detection and classification using image processing techniques, machine learning and integrated models in urban areas: A novel image binarization technique, (n.d.).
[43] S. Kulkarni, S. Singh, D. Balakrishnan, S. Sharma, S. Devunuri, S.C.R. Korlapati, CrackSeg9k: A Collection and Benchmark for Crack Segmentation Datasets and Frameworks, (2022). http://arxiv.org/abs/2208.13054 (accessed October 24, 2023).
[44] A. Krizhevsky, I. Sutskever, G.E. Hinton, ImageNet classification with deep convolutional neural networks, Commun. ACM 60 (2017) 84–90. https://doi.org/10.1145/3065386.
[45] E. Guerra, J. De Lara, A. Malizia, P. Díaz, Supporting user-oriented analysis for multi-view domain-specific visual languages, Information and Software Technology 51 (2009) 769–784. https://doi.org/10.1016/j.infsof.2008.09.005.
[46] C. Szegedy, W. Liu, Y. Jia, P. Sermanet, S. Reed, D. Anguelov, D. Erhan, V. Vanhoucke, A. Rabinovich, Going Deeper with Convolutions, (2014). https://doi.org/10.48550/ARXIV.1409.4842.

[47] K. He, X. Zhang, S. Ren, J. Sun, Deep Residual Learning for Image Recognition, (2015). http://arxiv.org/abs/1512.03385 (accessed July 18, 2023).
[48] S. Ren, K. He, R. Girshick, J. Sun, Faster R-CNN: Towards Real-Time Object Detection with Region Proposal Networks, (2016). http://arxiv.org/abs/1506.01497 (accessed July 18, 2023).
[49] Yue Zhang, Xinxiang Zhang, Effective real-scenario Video Copy Detection, in: 2016 23rd International Conference on Pattern Recognition (ICPR), IEEE, Cancun, 2016: pp. 3951–3956. https://doi.org/10.1109/ICPR.2016.7900252.
[50] X. Yang, H. Li, Y. Yu, X. Luo, T. Huang, X. Yang, Automatic Pixel-Level Crack Detection and Measurement Using Fully Convolutional Network, Computer Aided Civil Eng 33 (2018) 1090–1109. https://doi.org/10.1111/mice.12412.
[51] K. He, G. Gkioxari, P. Dollár, R. Girshick, Mask R-CNN, (2018). http://arxiv.org/abs/1703.06870 (accessed November 29, 2023).
[52] N. Gehri, J. Mata-Falcón, W. Kaufmann, Automated crack detection and measurement based on digital image correlation, Construction and Building Materials 256 (2020) 119383. https://doi.org/10.1016/j.conbuildmat.2020.119383.
[53] G. Lemaire, G. Escadeillas, E. Ringot, Evaluating concrete surfaces using an image analysis process, Construction and Building Materials 19 (2005) 604–611. https://doi.org/10.1016/j.conbuildmat.2005.01.025.
[54] L.F.M. Sanchez, B. Fournier, M. Jolin, D. Mitchell, J. Bastien, Overall assessment of Alkali-Aggregate Reaction (AAR) in concretes presenting different strengths and incorporating a wide range of reactive aggregate types and natures, Cement and Concrete Research 93 (2017) 17–31. https://doi.org/10.1016/j.cemconres.2016.12.001.
[55] Md.A.-M. Khan, S.-H. Kee, A.-S.K. Pathan, A.-A. Nahid, Image Processing Techniques for Concrete Crack Detection: A Scientometrics Literature Review, Remote Sensing 15 (2023) 2400. https://doi.org/10.3390/rs15092400.
[56] C. ASTM, Standard test method for concrete aggregates by determination of length change of concrete due to alkali-silica reaction, (1995). https://doi.org/10.1520/C1293-20A.
[57] Rasband, W.S, Image J, (1997). https://imagej.nih.gov/ij/.
[58] O. Stankiewicz, G. Lafruit, M. Domański, Multiview video: Acquisition, processing, compression, and virtual view rendering, in: Academic Press Library in Signal Processing, Volume 6, Elsevier, 2018: pp. 3–74. https://doi.org/10.1016/B978-0-12-811889-4.00001-4.
[59] I. Culjak, D. Abram, T. Pribanic, H. Dzapo, M. Cifrek, A brief introduction to OpenCV, (n.d.).
[60] Z. Zhang, A flexible new technique for camera calibration, IEEE Trans. Pattern Anal. Machine Intell. 22 (2000) 1330–1334. https://doi.org/10.1109/34.888718.
[61] GIMP, (2019). https://www.gimp.org.

Chapter 3 : Developing an Image Acquisition and Processing Procedure for Automated Damage Quantification of a Concrete Surface

3.1. Abstract

Quantification of the damage extent of concrete through visual inspections has been limited to practical methods that may result in subjective interpretation of the outcomes and image analysis without association with the cause of the damage. The presence of cracks can indicate some form of distress mechanism through their characteristic pattern; however, the extent of that damage along with the time-consuming nature to obtain a quantitative result in which it can be monitored over time is often limited. With emerging technologies such as machine learning, namely mask R-CNNs, used to detect, segment, and classify objects observed in images along with accessibility to high-resolution digital cameras, quantitative visual inspections used to monitor the progression of damage to concrete are required. Although some works have been developed to detect surface cracking and remove certain artifacts from images, quantifying the outputs from image analysis and associating it to certain distress mechanisms such as alkali-silica reaction (ASR) remains a challenge. Moreover, the lack of a standard approach for image acquisition and processing can limit usable datasets for machine learning in which the key features (i.e., cracks) are not annotated, scaled, or clearly visible/recognizable in the images. Consequently, there's a growing need to develop refined and more accurate visual inspection methods through digitalization. This effort is essential in improving condition assessment and establishing protocols for maintaining infrastructure affected by ASR deterioration. As such, this work aims to provide a standardized methodology for image acquisition and processing for quantitative image analysis purposes. A comparison between operators during on-site manual measurements was further conducted to

understand the influence of the operator on the results meanwhile comparing manual and digital measurements. Moreover, conventional crack quantification (i.e., cracking index – CI) was compared to a novel metric used to quantify and characterize cracks at the concrete's surface through its intensity (i.e., Total Crack Length – TCL) as cracking length over the total analyzed area) combined with crack orientations. This comparison aims to validate the reliability of assessment outcomes produced through the application of an image-based measurement approach.

3.2. Introduction

In the context of concrete condition assessment, visual inspection is a significant technique to monitor the structure health by identify and define various of defection signs appears on element surface over the time. Correspondingly, a trained model that can effectively identify and measure cracks on concrete surfaces. This method offers a non-destructive approach to evaluating damage, eliminating human subjectivity in the analysis. However, the challenge lies in providing the machine with sufficient and accurate knowledge of damaged concrete. Artificial Intelligence (AI) encompasses the development of computer systems capable of emulating human intelligence, involving learning and applying knowledge to new situations. Machine Learning (ML), a subset of AI, focuses on enhancing computer performance through data-driven learning and making decisions based on statistical models. Recently, ML and its more advanced counterpart, Deep Learning (DL) have been applied to concrete condition assessment, particularly in automating crack detection, offering quantitative results [52,53]. The Mask R-CNN method stands out as a novel approach for detecting and quantifying cracks through image processing [8,47]. Concerns regarding image quality criteria may affect the accuracy of damage quantification results. The integration of ML and DL into concrete condition assessment has the potential to revolutionize the field, improving accuracy and efficiency in damage detection and quantification. However, challenges related to data (i.e., image) quality must be addressed for optimal results.

Alkali-silica reaction (ASR), a form of internal swelling reaction, is a distress mechanism that compromises the functionality of concrete infrastructure. ASR entails a sequence of chemical reactions that lead to the formation of hygroscopic "ASR gel", causing an expansion in volume and thereby inducing the propagation of cracks throughout the concrete element [1,14,54]. The development and extent of surface cracking on concrete structures exposed to the environment, particularly in the case of concrete members affected by ASR, are influenced by various factors (i.e., aggregate reactivity, pore solution alkalinity, presence of moisture, wind, heat, etc.). Yet, ASR-affected elements often exhibit a map-like crack pattern and may show signs of the element expansion and ASR gel presence [6,7]. Over time, these cracks progress in width and length, underscoring the progressive nature of the reaction's damaging effects.

Cracking patterns or signatures observed at the surface of concrete can provide valuable information about the underlying distress mechanisms. Whether the distress is caused by external factors such as environmental exposure or internal factors like material properties or construction practices, different cracking patterns can be associated with specific mechanisms or a combination of multiple mechanisms. For example, shrinkage cracks are commonly observed in concrete due to the drying and volume reduction that occurs during the curing process. These cracks typically appear as hairline cracks and are often evenly distributed across the concrete surface [1]. On the other hand, loading cracks can result from excessive applied loads or structural overloading. These cracks may exhibit a more irregular pattern and can be wider and more prominent compared to shrinkage cracks [1]. Nevertheless, the distinction between the causes of the cracking may be difficult to determine from a single inspection. As such, monitoring protocols and quantitative-based inspections have been developed to capture the progression of damage, indicating an active mechanism such as ASR. Among the protocols is the cracking index (CI) developed to capture changes in volume measured at the surface of the concrete. The CI entails tracing a square of 50 cm by 50 cm at the surface of a concrete element (which can be adjusted based on the size, configuration, and accessibility of the analyzed area) and measuring crack openings that cross the perimeter of this square. This method was developed as a practical way to quantify damage observed at the surface of the concrete while on site which can distinguish the directionality of the cracking pattern through vertical and horizontal comparisons. However, the CI can be time-consuming, and present some subjectivity in result interpretation and variability among operators requiring specified environmental conditions (i.e., time of day/year and meteorological). With the rise of new technologies such as machine learning (i.e., Mask R-CNNs and transfer learning) and accessibility to high-resolution digital cameras, the digitalization of such protocols has gained interest in the visual inspections and non-destructive testing field of work. Although the accessibility and applications of such tools are ever-growing, a standardized approach for image acquisition remains a major constraint in the further developments of automated monitoring systems able to quantify damage to concrete. Very limited datasets are currently available [11,55], thus hindering the application of machine learning to concrete deterioration quantification. Moreover, practical manual approaches used to annotate and measure cracking to concrete on the field in comparison to digital methods may limit the overall assessment (i.e., the information contained within the boundaries of the square/image). Very few metrics of damage quantification have been developed to validate the use of digital images [11,53].

3.2.1. Scope of the work

As previously stated, the cracking index (CI) can serve as an indicator to evaluate the concrete damage extent by obtaining crack measurements along the border of a square frame drawn on the concrete surface. However, there are potential limitations in terms of accuracy and accessibility when conducting these measurements. Therefore, there is an ongoing need to develop efficient methods with the aid of digital technology. Presently, machine learning techniques are gaining prominence and proving to be a powerful tool for detecting, segmenting, and classifying observed objects thus providing an opportunity to automate the crack measurement process. This automation can address the validation of image aspects to ensure that they accurately capture and reflect real measurements (i.e., ground truth). This advancement marks the initial step towards automating the crack measurement process for the purpose of assessing concrete damage. In this paper, an image acquisition and processing protocol was developed and assessed in which the optimal light conditions, operator sensitivity, and transition toward digital processing were verified through image and statistical analysis.

3.3. Methodology

3.3.1. Material

Seven concrete blocks of 450 mm by 450 mm by 675 mm were used for the analysis of this study. These blocks had been manufactured in a laboratory environment and had previously been the subject of investigation in studies [7,14]. The concrete mixtures of the blocks included highly reactive coarse (i.e., Springhill) and fine (i.e., Texas) aggregates. The blocks also featured various reinforcement configurations, detailed in the previous study [7,14] and shown in Table 3.1.The concrete blocks were produced following the ASTM C1293 [56] mixture proportions and stored under conditions of 38°C and 100% relative humidity in order to expedite the development of alkali-silica reaction (ASR). The blocks used in this current study were kept in the same conditions until they reached their ultimate expansion, at which point they were removed for use in this study. These blocks were selected because they have exposure environment controlled in the laboratory (to minimize variables such as sunlight, temperature), known level of damage (measured through expansion since the beginning of casting by [7,14]), abundance of cracking at the surface, and surface characteristics (flat, clean, free of defects, etc.) as shown in Figure 3.1. Meanwhile, some blocks are composed with reinforcement in one (transverse) or two (transverse and longitudinal) directions to provide a better understanding of the damage influenced by confinement.

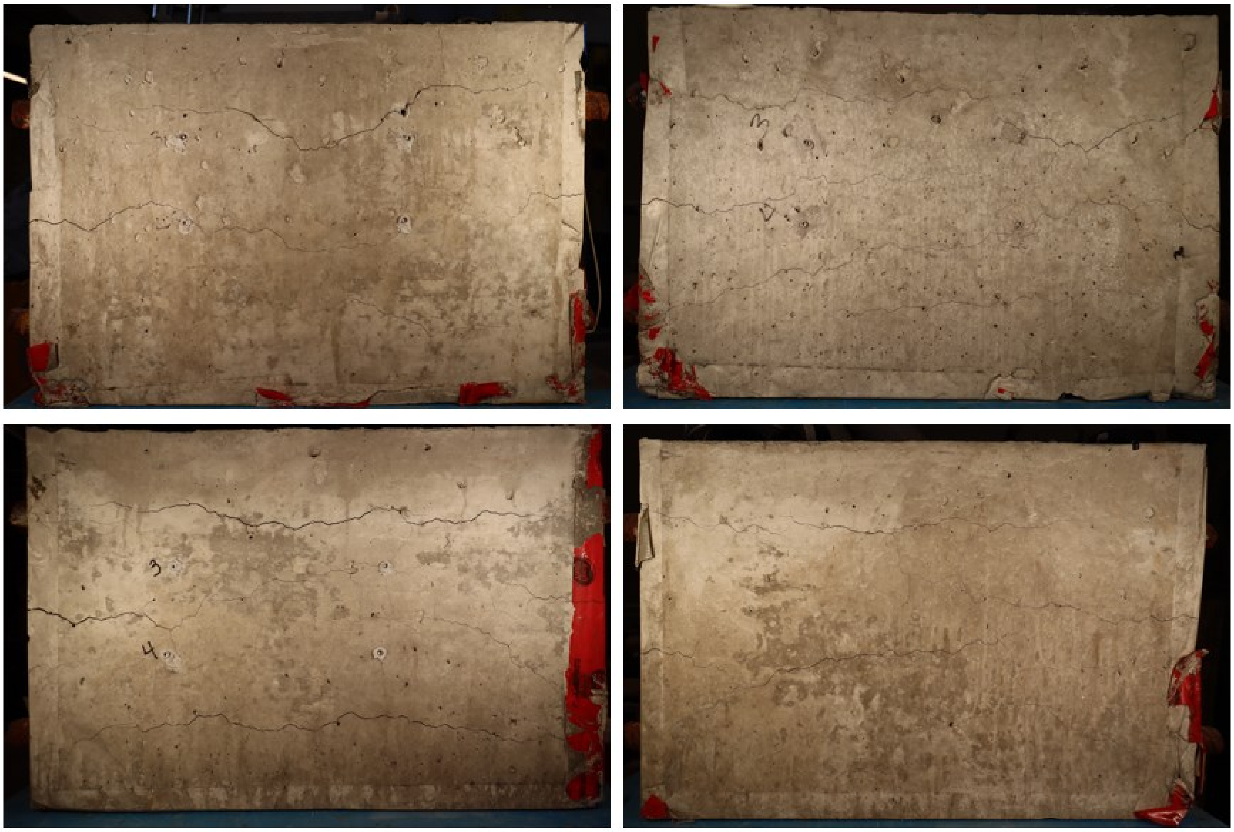

Figure 3.1: four sample surfaces from 7 concrete blocks in laboratory.

Table 3.1: Description of selected concrete blocks, 2D: concrete reinforced in 2 directions. SP: concrete mixture contains Springhill coarse. TX: concrete mixture contains Texas sand [7].

Block title	**Description**	**Measured expansion % up to date**	
		Longitudinal	Transverse
B3	Unconfined, SP	0.817	0.818
B5	Unconfined, SP	0.817	0.818
B12	1D - SP	0.817	0.818
B2D21	2D - SP	0.700	0.710
B2D19	2D - SP	0.700	0.710
B25	2D- TX	0.801	0.826
B2D29	2D - TX	0.801	0.826

Note: SP = Reactive Springhill coarse aggregate; TX = Reactive Texas sand; 1D = reinforcements in one direction; 2D = reinforcements in two directions.

3.3.2. Equipment and Methodology

3.3.2.1. Cracking index (CI)

The cracking index (CI) was used as a tool to measure both the operator variability and the variations when digitizing quantitative damage measurements on the concrete surface. Initially, two operators manually performed the operations (at consecutive times on the same surfaces), followed by a single operator conducting the measurements on digital images. For manual CI measurement, a 3D printed square frame of 0.25 m by 0.25 m is affixed directly on the concrete surface. Operators visually inspected the concrete surface, assessing the width of cracks encountered along each grid line of the reference frame. Subsequently, the operators recorded the measured crack widths and sum them up along each line, yielding a cumulative crack width value for that line. To measure the width of cracks on the surface of the investigated element, a magnifying lens (i.e., 25x or 30x magnification) with a plastic crack comparator card with absolute/discrete values was used (i.e., 0.10 mm to 1.5 mm). The surface grid, marked by four lines, was divided into ten intervals, serving as reference points for the crack measurements. The crack opening is defined as the total sum of all crack widths measured along the grid line in millimeters, while the base length represents the length of the grid line, typically expressed in meters. Alternatively, the base length can be adjusted according to the size of the specimen. The empirical CI formulas are as follows [6]:

$$CI = \frac{\sum Crack\ openings}{Base\ length} \qquad \text{Equation 1}$$

The digital CI analysis involved obtaining images of the same location under manual examination, along with processing them to ensure an accurate representation. Subsequently, the images underwent the annotation process which entailed marking the crack width along the edge of the square area. Following annotation, the image analysis software [57] calculated the pixel area marked with different colors for each of the two directions (i.e., vertical and horizontal). This allowed for the conversion of pixel counts into the actual width of the cracks, accounting for the image scale and distortion for each square segment cropped from the raw image.

3.3.2.2. Image acquisition

The image-collecting process is a crucial step for ensuring the image quality. This section undertakes a comprehensive approach to the image acquisition procedure, wherein the images selected for analysis must exhibit clear feature characteristics based on the goal of the analysis. In this study, cracks caused by ASR are the desired feature and more specifically to quantify their characteristics such as orientation, length, and width to highlight their distribution and pattern. The following will describe the image acquisition configuration used in this study.

Images are expected to demonstrate the features (i.e., cracks), differentiated pixel-wise, which allows the edge of each crack to be segmented from the surrounding background either manually or automatically in subsequent image processing. As such, the visual inspection protocol is expected to be digitized for further analysis. The following equipment and software were employed in the image acquisition process of this study:

1. ***Camera:*** A digital single-lens reflex (DSLR) camera (Figure 3.2a) was used, capturing high-quality images at a resolution of 24.1 megapixels, maximum image size of 6000x4000 pixels, and ISO sensitivity range of 100-25600. The camera was equipped with versatile lens with a focal length range of 18mm to 55mm and up to 1.6x zoom capability (i.e., Cannon’s EOS-T8i EF-S 18-55mm f/4-5.6 IS STM)

2. ***Remote shooting* software**: EOS Utility software (Figure 3.2b) facilitates the connection of the camera to a computer for remote shooting and camera control via a USB cable or Wi-Fi connection. A remote shooting option is preferred during the capturing process since minimizes vibrations. The connection also enables real-time review of captured images on the computer screen serving as a first stage of the quality validation.
3. ***Lighting:*** Compact and portable LED light kits (containing 480 LEDs unit) were used in this study (Figure 3.2c) to enhance the visibility of crack features, with adjustable intensity and color temperature (i.e., 3200k (yellow/amber) to 5600k (white/cold)) control the lighting conditions and reduce shadow noises.
4. ***Reference frames***: A 3D printed reference frame (25 cm x 25 cm) and a 3:2 ratio frame was used for image analysis and perspective distortion correction (The 3D printing source files for the frame can be found in Appendix A.). The frames were placed on top of the interest area and ensured consistent camera-to-surface distance (i.e., not varying zoom ranges and adjusting the reference frame to the picture frame size), minimizing parameters that could affect image quality.

   Each side of the 3D printed square was divided into 10 equally spaced intervals normally used to record the cracking index data and used for scaling purposes (Figure 3.2d). The reference grid was designed to be disassembled for easy compact storage while conserving the 90^o corners. It can then be tapped onto the concrete's surface directly.

   Perspective distortion occurs when the imaging frame of the camera cannot remain parallel to the target plane when taking a photo. As shown in figure 3.2a, this distortion results in the image taking on a trapezoidal shape instead of retaining a square shape as it appears, hence the image fails to display the correct measurement. There are many approaches to mitigate the perspective distortion, the method outlined in this project is to use a frame to assist the adjustment for the camera shooting angle and position, the detailed instruction on how to address the perspective is further illustrated in the image acquisition step-by-step procedure.

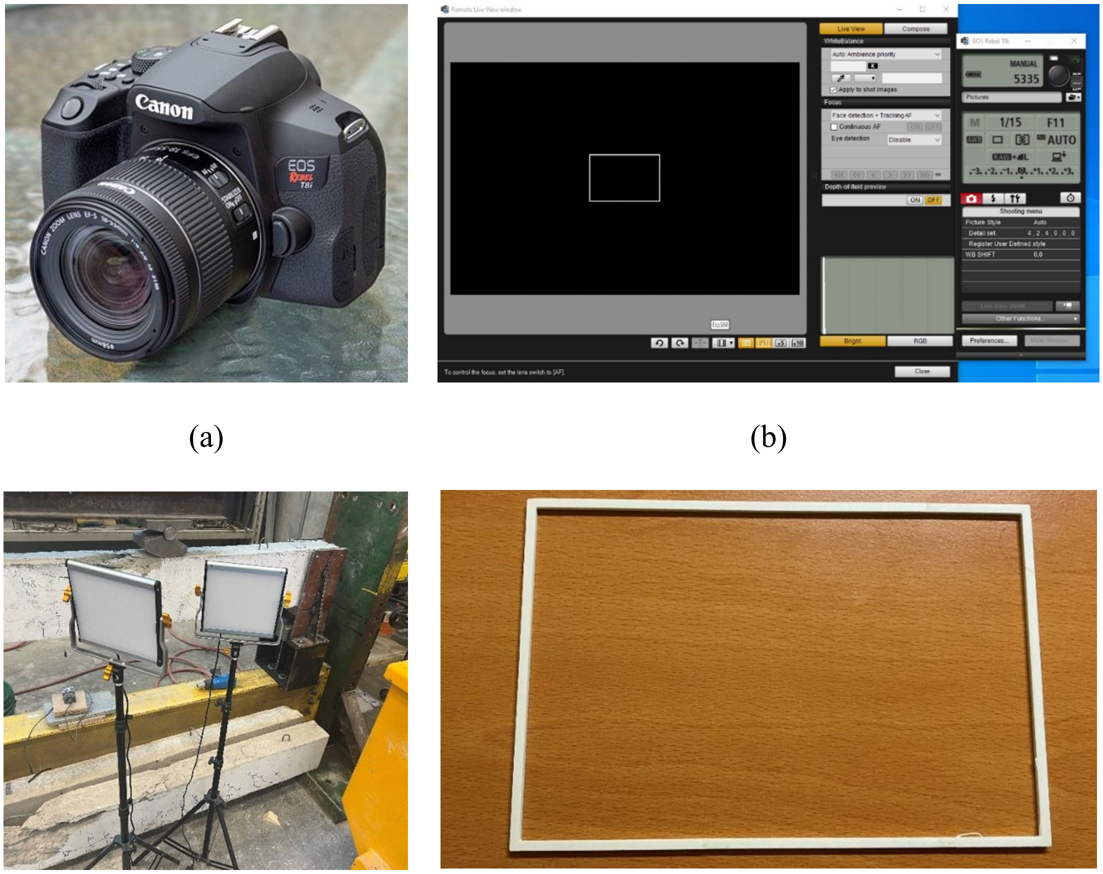

(a) (b)

(c) (d)

Figure 3.2: (a) A typical photographic DSLR camera with lens; (b) EOS utility software, remote shooting interface; (c) LED light Kits; (d) 3D Printed Reference Frames.

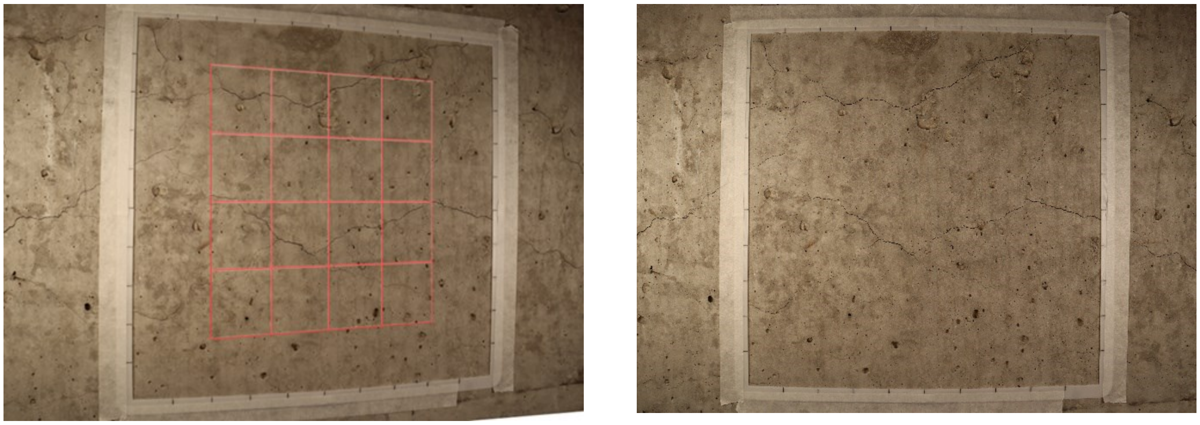

(a) (b)

Figure 3.3: (a) Image with perspective distortion, (b) image after perspective correction. Image (a) has the left side boarder wider than the right side, resulting in scale inconsistency for the whole image.

The image acquisition procedure involved setting up the equipment (Figure 3.4) capturing images under different lighting conditions: white (cold, 5600K), maximum yellow (warm 3200k), and white-yellow (daylight, 4800k). Nonetheless, camera settings and positioning for each image captured were kept consistent.

Figure 3.4: Image acquisition setup.

Figure 3.4 represents the flowchart regarding the step-by-step procedure for image acquisition. It is worth mentioning that the concrete blocks were lifted onto a table to allow for a comfortable working height thus, minimizing human error. The lights were placed on either side of the camera and the camera brought close to the surface of the concrete block until only the reference frame was brought into the field of view. The procedure will ensure that each image captured by camera can be fulfilled by the region of interest (ROI) with the maximum quality.

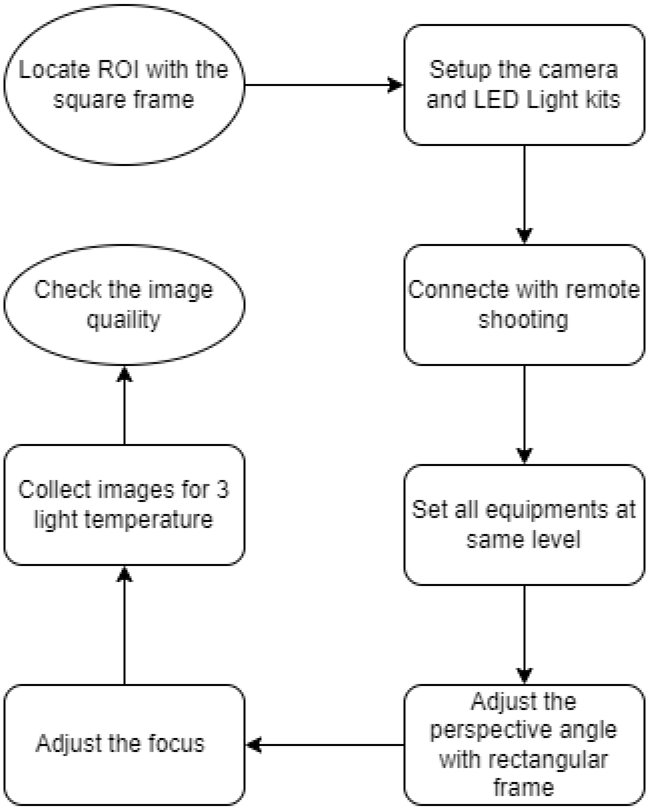

Figure 3.5: Image acquisition procedure flowchart.

1. Frame attachment: Attach the 3D-printed frame and the 3:2 perspective correction frame, as depicted in Figure 3.6, onto the damaged surface. The purpose of the outer frame is to locate the ROI and the inner frame is to aid the camera to mitigate the perspective distortion.
2. Camera setup: Ensure the tripod is stable and sturdy, with the camera securely locked, perfectly horizontal, and aligned with the center of the segment to prevent tilted or skewed images. Set the camera to manual focus mode and manually adjust the lens zoom to the minimum (1.0x). Observe through the camera LTCL screen and adjust the camera's position to ensure the outer frame overlaps with the camera view's border. If multiple ROIs need to be collected on the same surface, measure the distance between the camera lens and the objective surface for further reference.

3. Lighting setup: Set the camera and LED lights' heights lights at 45-degrees angles relative to the subject. These LED lights offer the capability to modify the color temperature within the range of 3200K to 5600K, allowing for a transition from a warm, yellowish color to a colder, white tone. The light temperature is an independent variable, and its control guarantees a consistent color temperature across the entire interest image area. This preservation of the intended color rendition remains unaffected by ambient light conditions.
4. Remote shooting: Connect the remote shooting software on the computer to the camera this allows for full control of the target feature to be captured. Utilizing this software offers an improved view on the computer screen and enables remote image capture, eliminating the need to physically touch the camera and ensuring a stable shooting process.
5. The camera lens should be in the minimum zoomed (1.0x) position.
6. Adjust the camera lens' zoom ring to view the perspective frame. Tune the height and shooting angle to guarantee that all four corners of the frame fit perfectly within the camera's view. Adjusting the camera position and angle until both vertical and horizontal boarder on the camera view is parallel with the edge of the frame. After the adjustment, the camera's shooting angle should be corrected to be perpendicular to the targeted surface.
7. Once ROI is set, adjust the zoom ring to the maximum (i.e., fully zoomed-in) and while watching the camera display though EOS utility software on laptop, adjust the focus ring until a crack or any other surface feature is in focus. This ensures the best image quality.
8. Zoom-out the zoom ring on until the view is back to the original position with the entire reference frame into the field of view and click the trigger button on the remote shooting software, review the image to check the image quality.

9. Adjust the LED light temperature to another color and proceed step 8 again until the 3 different color temperature (warm, cold, and intermediate) images were captured.
10. Review the image quality, relocate the equipment to collect the next ROI segment, repeat step 1 to 9.

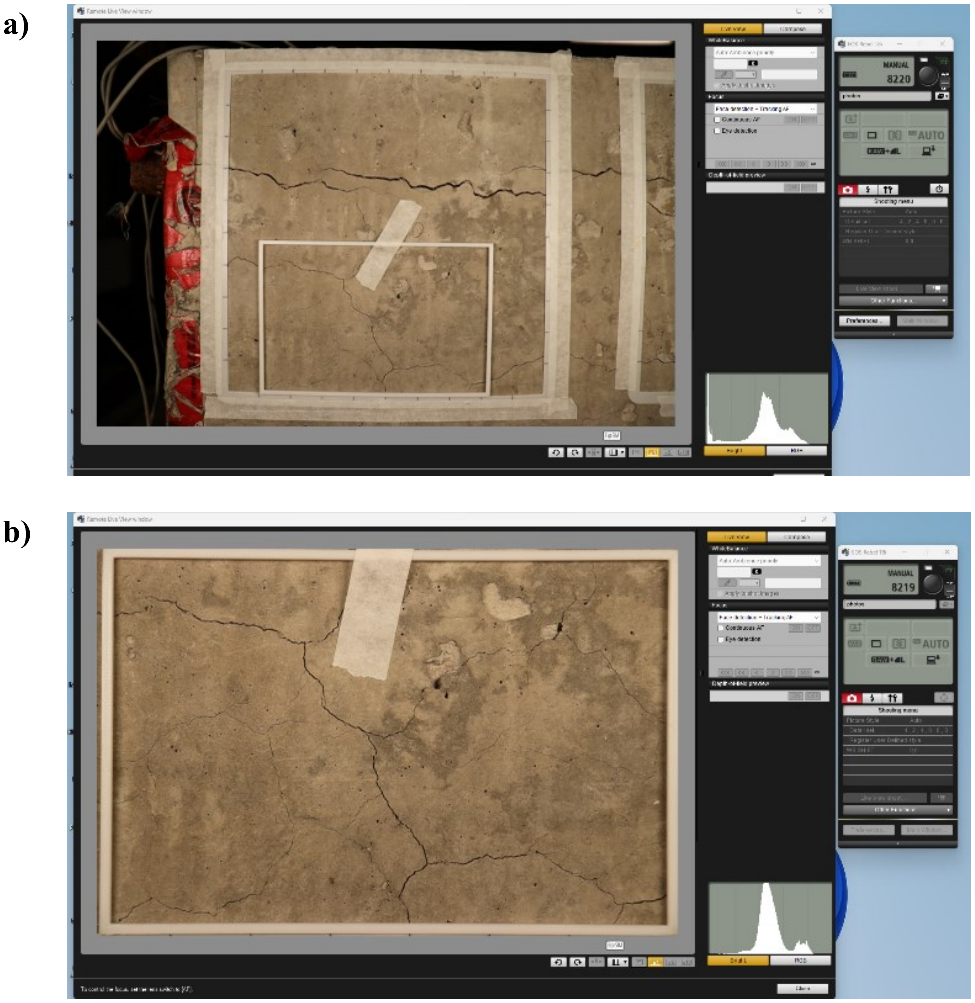

Figure 3.6: (a) A perspective frame affixed at the lower part of the reference frame and (b) the perspective frame in the full field of view after zoom-in.

3.3.2.3. Image processing

After the images are captured, the processing phase is the next stage on the process of data collection.

Correcting for barrel distortion

Other than perspective distortion, images captured by a DSLR camera can always have images distorted due to cameras wide angle lens structure, which arises from aberrations near the image edges. This type of problem has been introduced by Stankiewicz et al. (2018), where lens distortion represents a departure from the theoretical projection outlined in the pinhole camera model [58]. This phenomenon constitutes an optical aberration, causing straight lines within the scene to appear curved or distorted within the resulting image.

a)

b)

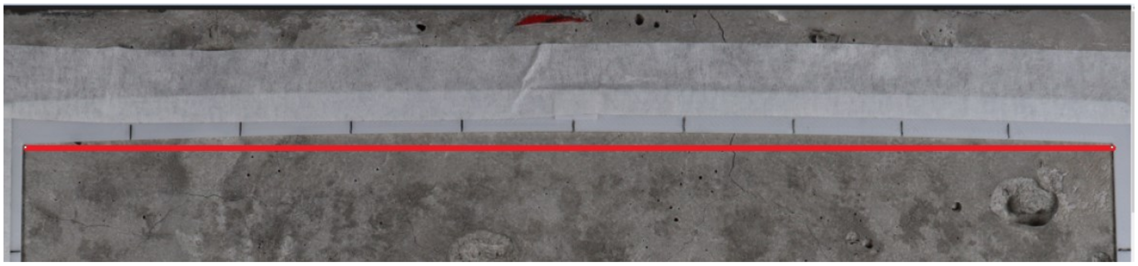

Figure 3.7: Barrel distortion that appears near the edge of the frame that led image has distortion curves outward. (a) shows the full image and (b) shows the upper edge with the outward distortion curve.

As shown in Figure 3.7, an instance of barrel distortion is evident in the sample image captured by the camera employed for this project. This distortion is generated as a bending or curving effect along the edges of the reference frame within the image, which may induce inaccuracies when collecting quantitative data during subsequent post-processing.

To remove image distortion caused by a camera lens, two methods are available: 1) manually correcting the barrel distortion using an open source or commercial image processing software (i.e., Adobe Photoshop) or 2) automating the procedure using a camera calibration algorithm. The most common and practical approach for image analysis purposes is to perform a camera calibration technique using an algorithm on the OpenCV platform [59] , which stands for Open-Source Computer Vision Library. OpenCV is an open-source software library dedicated to computer vision and machine learning tasks. OpenCV offers an extensive range of tools and functions designed for processing images and videos. These include advanced algorithms for detecting features, recognizing objects, stitching images together, calibrating cameras, and much more. OpenCV is available for several programming languages, including Python, Java, and C++, allowing developers to leverage its capabilities across various platforms.

Zhang et al. (2000) has developed a camera calibration algorithm and illustrate the calibration process by a mathematic model. The pin-hole camera model establishes a mathematical relationship between the three-dimensional (3D) coordinates in the real world and their projection onto a two-dimensional (2D) image plane [60].

The calibration process typically involves capturing a set of calibration images, estimating camera parameters, and applying distortion correction to subsequent images. The following is a general overview of the steps involved:

1. ***Capture calibration images:*** Take a series of images (around 20 - 30) of a calibration pattern from different angles and distances within the camera's field of view. Ensure the calibration pattern covers a significant portion of each image. The study from Zhang et al. (2000) indicated that the chessboard/checkerboard pattern (Figure 3.8) is commonly used as a calibration target, which includes a grid that has distinct corner geometry allowing for precise calibration calculations [48]. Chessboards used for calibration shall be printed on a flat surface with very precise, sharp and clear quality on every edge corner, otherwise, the camera calibration algorithm cannot recognize and proceed the computation.

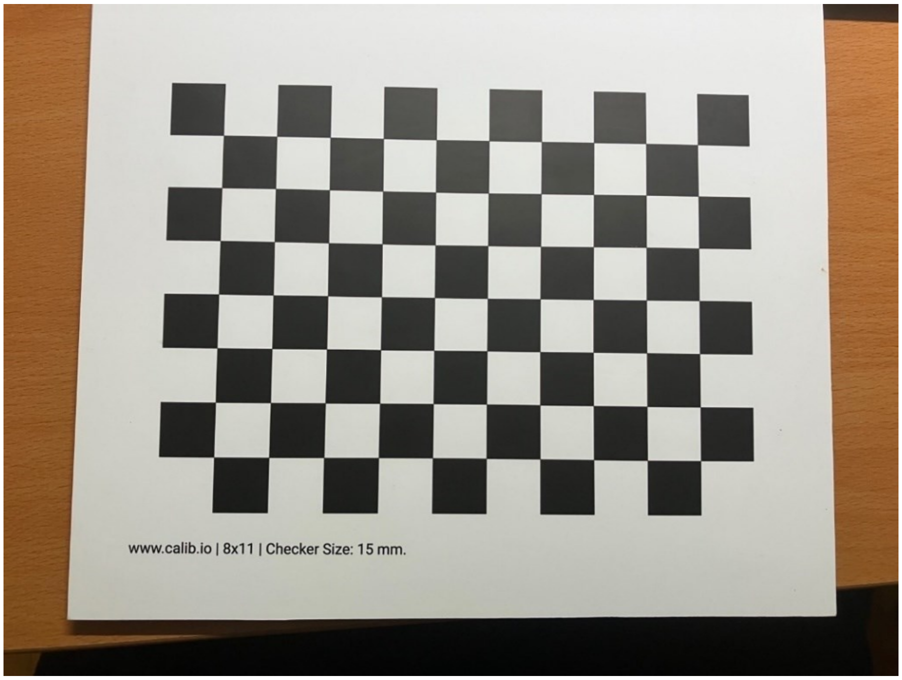

Figure 3.8: A chessboard pattern for camera calibration. The chessboard was professionally printed on an aluminium board by a local photography equipment and service supplier.

2. ***Detect calibration pattern corners:*** Detecting corners of the calibration pattern is accomplished by inputting the calibration image set into a Python code named "calibration," executed within the PyCharm software (Figure 3.9), an integrated development environment (IDE). This code can identify the corners of the calibration pattern in each image by detecting substantial changes in color in pixel wise.

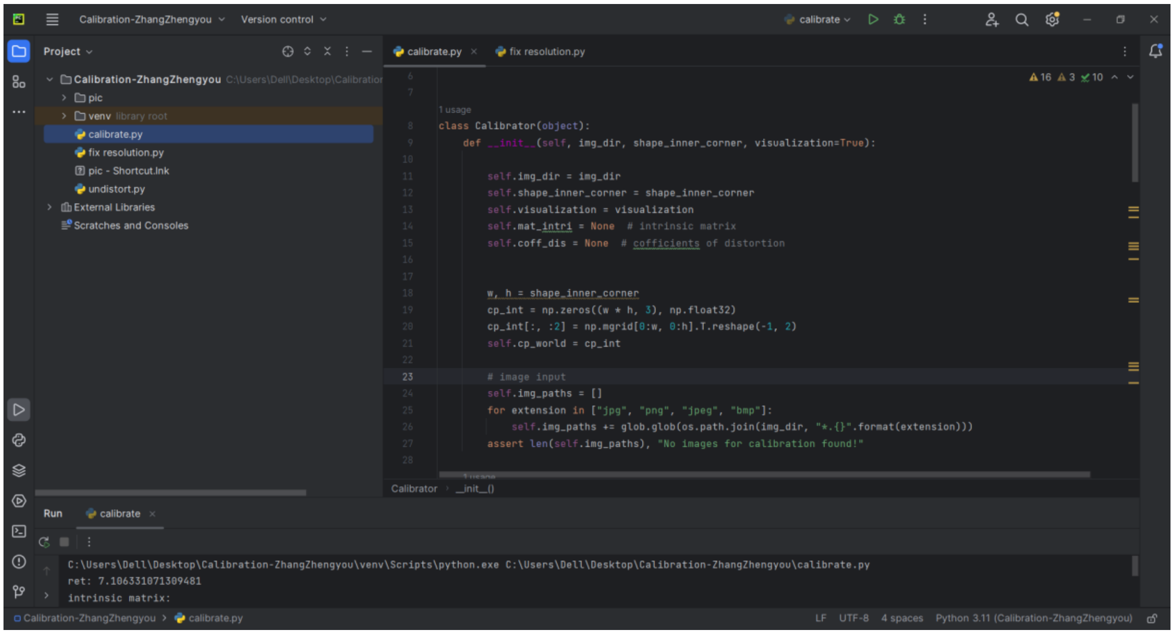

```python
class Calibrator(object):
    def __init__(self, img_dir, shape_inner_corner, visualization=True):

        self.img_dir = img_dir
        self.shape_inner_corner = shape_inner_corner
        self.visualization = visualization
        self.mat_intri = None  # intrinsic matrix
        self.coff_dis = None  # cofficients of distortion


        w, h = shape_inner_corner
        cp_int = np.zeros((w * h, 3), np.float32)
        cp_int[:, :2] = np.mgrid[0:w, 0:h].T.reshape(-1, 2)
        self.cp_world = cp_int

        # image input
        self.img_paths = []
        for extension in ["jpg", "png", "jpeg", "bmp"]:
            self.img_paths += glob.glob(os.path.join(img_dir, "*.{}".format(extension)))
        assert len(self.img_paths), "No images for calibration found!"
```

```
C:\Users\Dell\Desktop\Calibration-ZhangZhengyou\venv\Scripts\python.exe C:\Users\Dell\Desktop\Calibration-ZhangZhengyou\calibrate.py
ret: 7.106331071309481
intrinsic matrix:
```

Figure 3.9: PyCharm interface, an IDE for executing image analysis integrate with OpenCV library.

3. ***Calculate camera parameters***: Calculating camera parameters involves utilizing the calibration algorithm to estimate intrinsic camera parameters as shown in Figure 3.10 (such as focal length, distortion coefficients and principal points) as well as extrinsic parameters (comprising rotation and translation vectors). These estimations are derived from the identified corners within the calibration images.

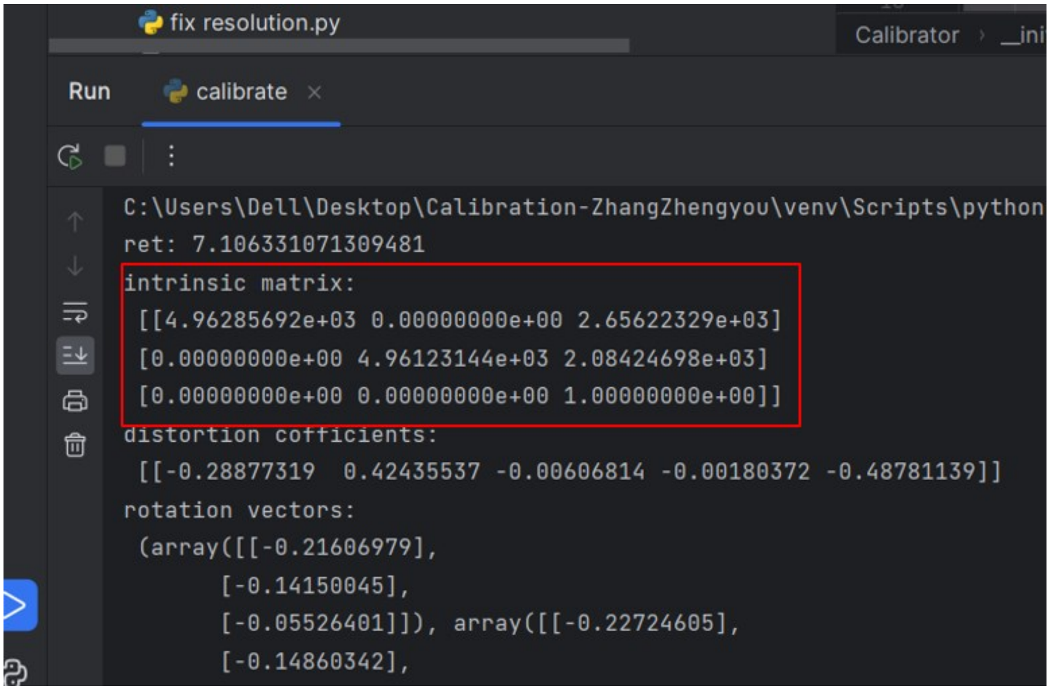

```
C:\Users\Dell\Desktop\Calibration-ZhangZhengyou\venv\Scripts\python
ret: 7.106331071309481
intrinsic matrix:
 [[4.96285692e+03 0.00000000e+00 2.65622329e+03]
 [0.00000000e+00 4.96123144e+03 2.08424698e+03]
 [0.00000000e+00 0.00000000e+00 1.00000000e+00]]
distortion cofficients:
 [[-0.28877319  0.42435537 -0.00606814 -0.00180372 -0.48781139]]
rotation vectors:
 (array([[-0.21606979],
       [-0.14150045],
       [-0.05526401]]), array([[-0.22724605],
       [-0.14860342],
```

Figure 3.10: Intrinsic and extrinsic parameter results calculated by the camera calibration algorithm.

4. ***Undistort images:*** Executing another code named as "undistortion" to fix the image barrel distortion within the assigned folder with the camera parameters (intrinsic and extrinsic matrix) input calculated by "calibration" code from step 2. This code processes all subsequent images, utilizing the intrinsic camera parameters as input. This operation entails applying inverse distortion equations to each pixel, effectively eliminating the distortion effect.

Once the undistortion parameters are applied to the images, the previously displaced pixels within the image will be restored to their original positions. The precision of the undistortion process is influenced by the quantity of calibration images captured with the specific camera. It is only necessary to calibrate a camera once during its lifetime. The camera matrix and distortion coefficients obtained from the calibration can be stored using write functions in NumPy [59], allowing them to be readily accessed for future applications. This calibration process further allows for any device to be used during image analysis thus, an accessible approach to quantify features in images. Indeed, the lower the resolution of the images, the higher the uncertainty of the results which would need to be considered during the analysis.

Image cropping

After addressing the distortion issue, the subsequent step involves cropping the images to fit within the confines of the reference frame (Figure 3.11), ensuring they adopt a square shape, and resizing them to a uniform resolution of 3000 x 3000 pixels. It's important to note that when a camera captures images at varying distances, a phenomenon referred to as scale variation or scale distortion can occur. This arises due to the changing proximity between the camera and the subject during different setups, which impacts the perceived size of objects within the images. In more detail, when the camera is positioned closer to the subject, objects within the scene tend to appear larger within the image. Conversely, as the camera is moved further away, those same objects assume a smaller appearance in subsequent images. To manage this scale variation, resizing the images in alignment with the reference frame serves as a practical approach since the distance within the reference frame is known (i.e., 25 cm). This resizing assists in maintaining a consistent scale, thereby contributing to improved image processing outcomes. At this point, the images are prepared for subsequent stages of image data collection.

Figure 3.11: Cropped, resized image to 3000 by 3000 pixels or 25 cm by 25 cm ready for analysis.

Image analysis for quantitative comparison

To produce the quantification result, this study relies on an image analysis software called ImageJ [57] as shown in Figure 3.12. It is an open-source image processing software widely used for scientific research fields. It provides various functions for image editing, analyzing and processing, enhance the intensity of visualized effects for featuring details in an image. Moreover, ImageJ has various statistic analyzers to generate numerical result in pixel wise of an image.

A new parameter, referred to as "Total Crack Length (TCL)," has been introduced as an indicator to enhance the quantification of concrete damage analysis. TCL is determined by dividing the total crack length by the surface area, and it is a measurement that cannot be feasibly performed manually on-site. Therefore, TCL is proposed as an innovative measurement that is expected to provide more comprehensive information than the Cracking Index method, regarding the extent of damage. To calculate the TCL output, a crack tracing technique is necessary, and the details are explained in the following sections (Figure 3.13).

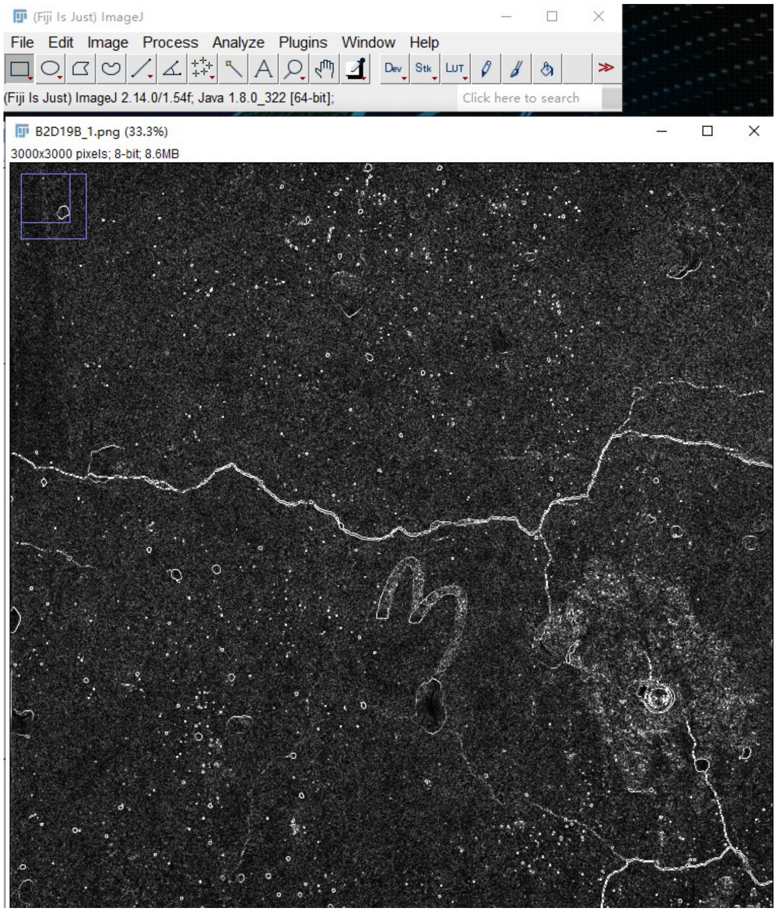

(Fiji Is Just) ImageJ 2.14.0/1.54f; Java 1.8.0_322 [64-bit];

3000x3000 pixels; 8-bit; 8.6MB

Figure 3.12: The interface of Image J.

In this study, a series of images featuring cracks are manually annotated using an image processing software [61] (provided compatibility with the device used during the annotations) and a tablet with pen by tracing the cracks using the pencil function with a known pixel width. The annotation set-up was selected due to availability yet is not limited to this type of set-up. To ensure enhanced quantitative analysis, the cracks are annotated using precise RGB color codes such as red (255, 0, 0), blue (0, 0, 255), or green (0, 255, 0). Meanwhile, it is advocated to use different color for every count of cracks (as shown in Figure 3.13) to help segment between every crack and generate a precise quantification result.

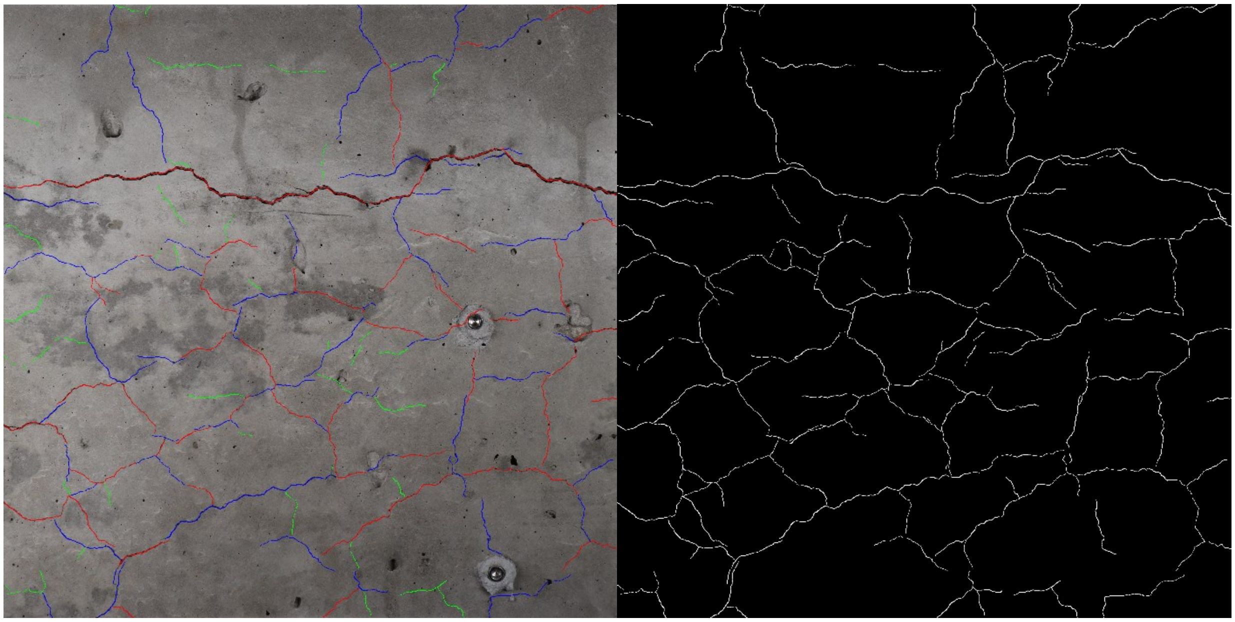

Figure 3.13: A traced image with its mask layer.

In general, cracks tend to propagate linearly and may possibly result in branching and spalling at specific points along their initial course. To enable ImageJ to effectively differentiate between distinct cracks and accurately count them, it becomes imperative to trace the cracks using distinct colors for each branch. For example, two cracks forming a "Y" shape may be recognized as one crack therefore colour segmentation is favourable This approach facilitates the segmentation of individual cracks from one another. Several guidelines should be adhered to during the annotation process, as follows:

1. Enable the use of layers in image processing software [61].
2. Commence crack tracing from a root crack. At a node point, each branch is treated as a separate crack.

3. Utilize a different color for tracing when a crack ceases to continue.
4. Extremely thin cracks can be disregarded. This decision reflects on the disregard of very thin cracks (less than 0.1 mm in width, Figure 3.14) during the cracking index calculation.
5. Avoid using the same color when two cracks are positioned too closely to each other.
6. Use the “mask” layer for further processing (for each colour or for all colours representing all cracks traced).

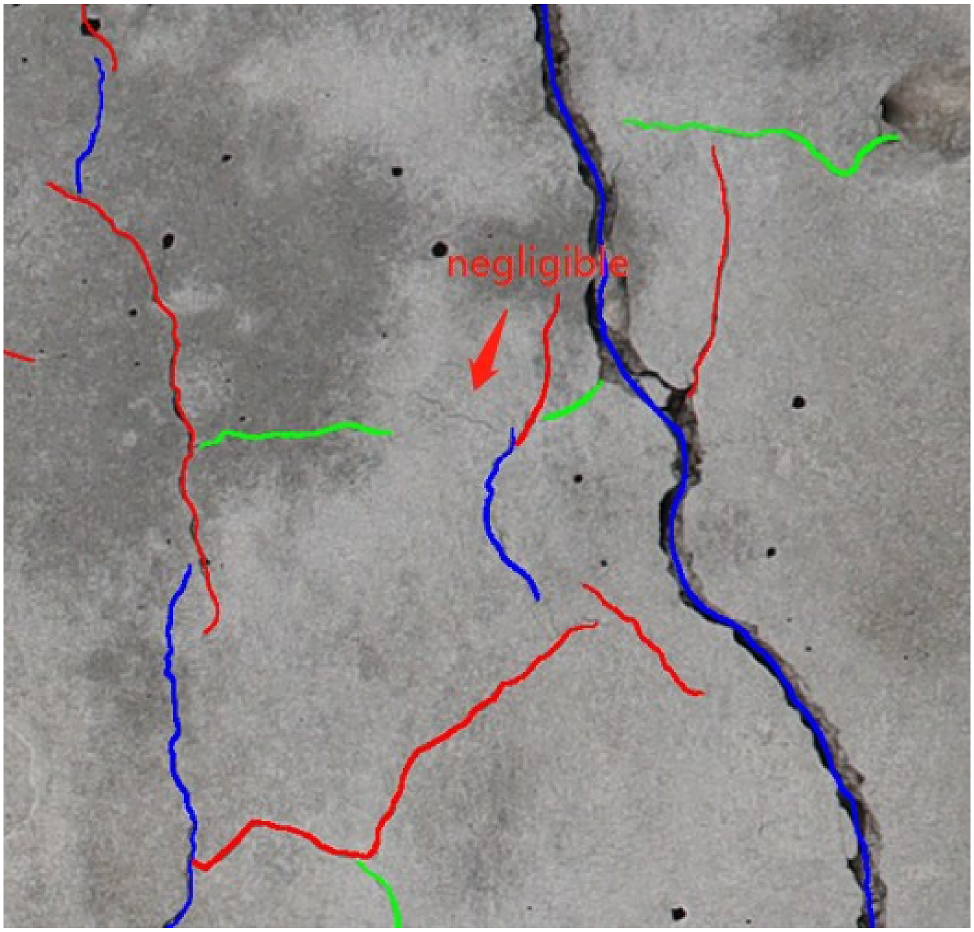

Figure 3.14: Partial of crack tracing and a negligible crack example.

After the images have been processed and annotated following the steps above, they are now prepared for the analysis phase, which involves utilizing ImageJ software to generate results. Figure 3.15 illustrates a procedure for acquiring pixel area using ImageJ's analyzer tool. To achieve this:

1. Import the mask layer to image J and Transform the image to 8-bit grayscale: Choose [Image] → [Type] → [8-bit].
2. Next, establish a threshold value to isolate the colors within the desired range for analysis. Set the threshold: Go to [Image] → [Adjust] → [Threshold], adjust the threshold bar to encompass the relevant color range in the image, and click [Apply].
3. Perform particle analysis: Navigate to [Analyze] → [Particle Analyze]. A spreadsheet will be generated, containing information such as the total area in pixels occupied by cracks, the count of cracks, and the area in pixels for each individual crack. This spreadsheet can then be exported as a .csv file.

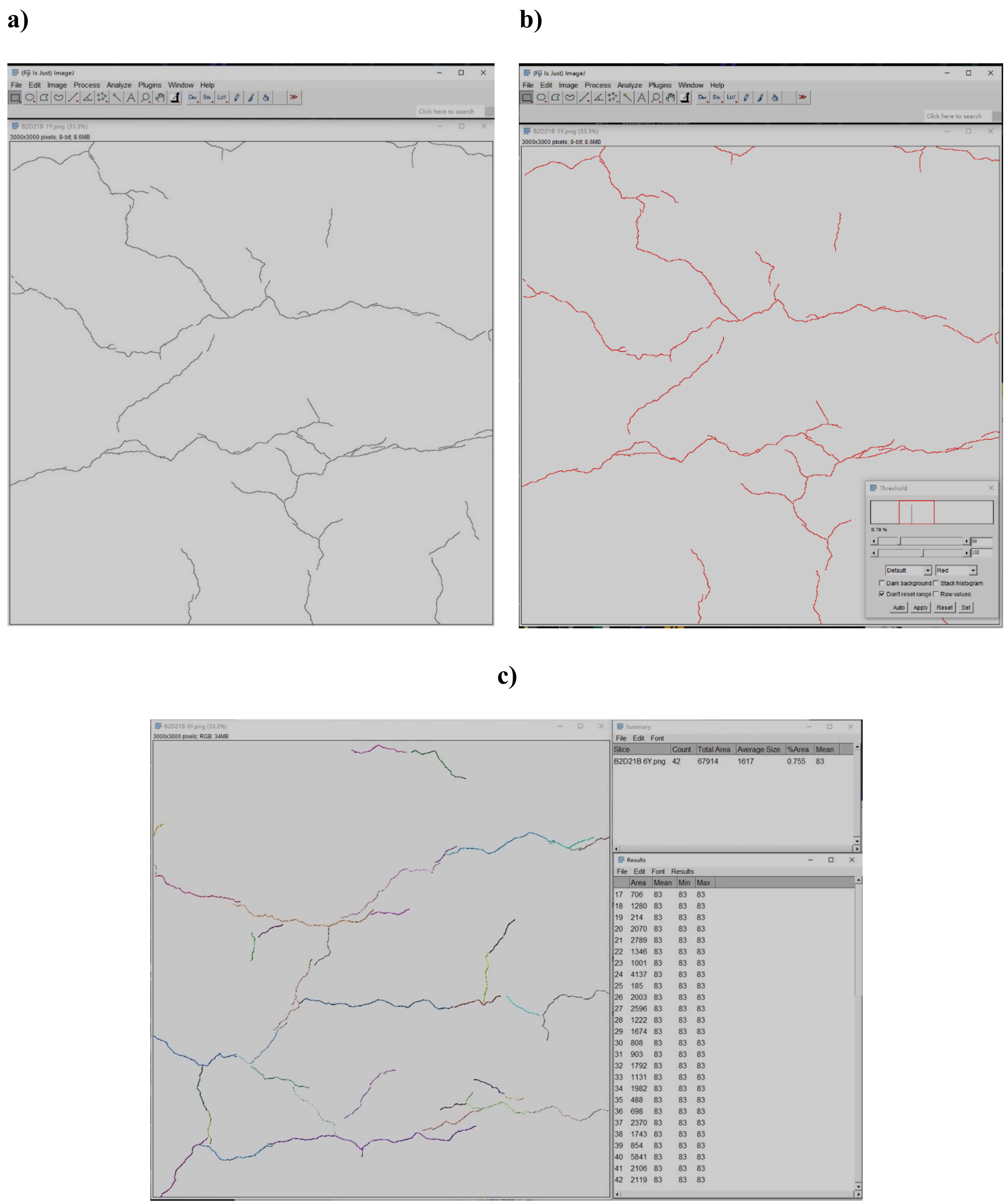

0.78 %

59

132

Default Red

☐ Dark background ☐ Stack histogram

☑ Don't reset range ☐ Raw values

Slice	Count	Total Area	Average Size	%Area	Mean
B2D21B 6Y.png	42	67914	1617	0.755	83

	Area	Mean	Min	Max
17	706	83	83	83
18	1280	83	83	83
19	214	83	83	83
20	2070	83	83	83
21	2789	83	83	83
22	1346	83	83	83
23	1001	83	83	83
24	4137	83	83	83
25	185	83	83	83
26	2003	83	83	83
27	2596	83	83	83
28	1222	83	83	83
29	1674	83	83	83
30	808	83	83	83
31	903	83	83	83
32	1792	83	83	83
33	1131	83	83	83
34	1982	83	83	83
35	488	83	83	83
36	698	83	83	83
37	2370	83	83	83
38	1743	83	83	83
39	854	83	83	83
40	5841	83	83	83
41	2106	83	83	83
42	2119	83	83	83

Figure 3.15: Generating result for crack area in pixel wise. (a)Transform the image to 8-bit grayscale, (b)adjust the threshold bar to encompass the relevant color range in the image, (c) Perform particle analysis, spreadsheet will be generated.

The results exported entail the number of cracks along with their length after which the calculation for the Total Crack Length can be applied (i.e., total crack length over analyzed area). The results are not limited to lengths but can also describe preferential crack orientation and lengths, etc. which will be further shown in the “Results” and discussed in the “Discussion” section. Figure 3.16 summarizes the essential steps used in this study. Crack counts may also be selected for output however, due to the length of cracks, the counts were not part of the metrics used in this study. Nevertheless, this study's methodology aims to enhance the accuracy of crack assessment through image analysis as opposed to manual measurement.

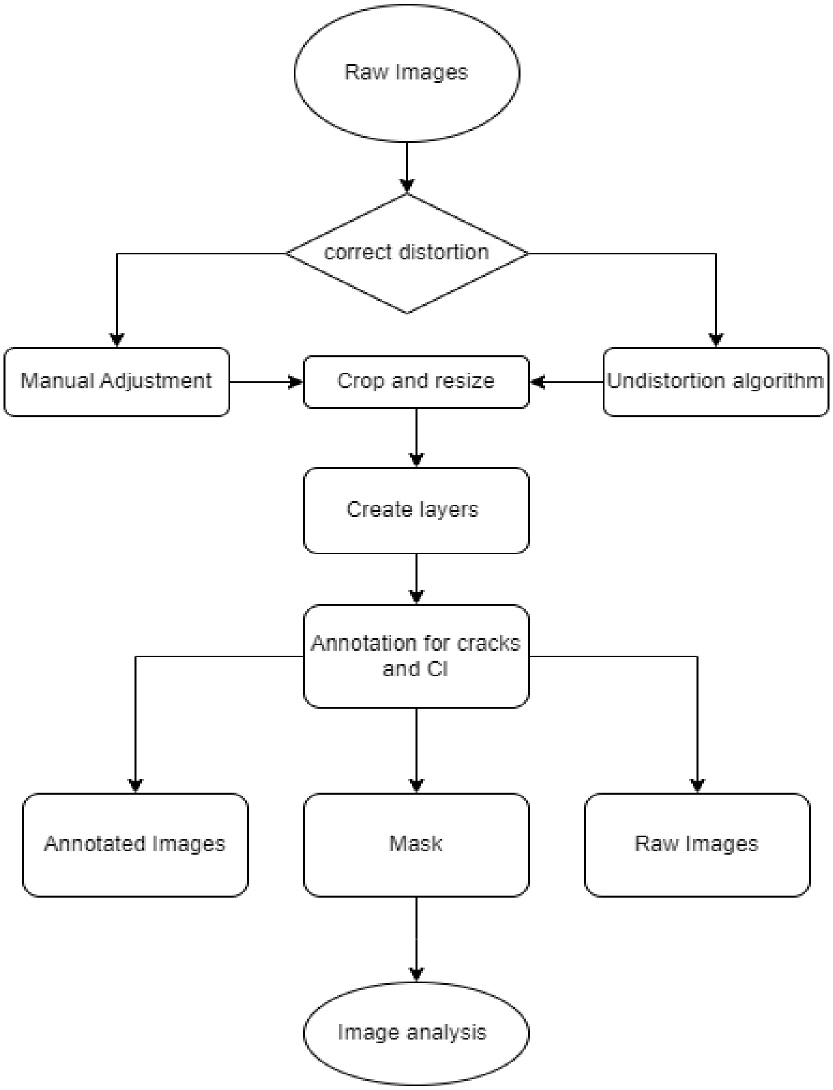

Figure 3.16: Image processing flowchart.

3.4. Results

3.4.1. ASR damage measured through the cracking index (CI)

The cracking index (CI) outcomes for seven concrete blocks were manually recorded by two operators according to Eq. 3.1. The surfaces of each concrete block, provided they were clean, unmarked, and free of artifacts that may compromise the measurement, were divided into 6 portions of 25 cm by 25 cm squares (i.e., segments). The CI is normally performed on a square of 50 cm by 50 cm; however, for this project, the aim was to optimize the number and quality of images; therefore, smaller squares were selected. An example from the result table for one segment collected by manual measurement is presented in Appendix B.1 with the average value of CI calculated for 6 segments, which shows the CI results of a region of interest (ROI) portion of the block B2D21, thus showcasing the crack widths manually measured in millimeters and their corresponding positions, denoted as steps 1 to 10, along each side of the reference frame. After all crack measurements over one square segment were recorded, the CI along one side of the ROI can be calculated by dividing the sum of crack width by the base length (0.25m).

$$CI = \frac{\sum Crack\ openings}{Base\ length} \qquad \text{Equation 3.1}$$

Based on the crack width collected during the CI measurement, the majority of cracks exhibit a width of less than 1.00 mm. All cracks observed on unreinforced blocks have a width range between 0.1mm to 1.0mm. Cracks distributed on reinforced blocks have a relatively wider crack width range, within 0.1mm to 2.0mm mostly. Cracks with widths exceeding 2.00 mm are uncommon, appearing predominantly in blocks with severe expansion (i.e., greater than 0.73% of expansion). Among all 1814 measurements, only one crack on Block B2D29 had a crack width exceeding 2.5 mm oriented in the horizontal direction. CI can exhibit an overlap between different types of blocks, yet some clustering is observed. The CI for 2D-TX blocks can range from 3.5 mm/m to 14.50 mm/m. Furthermore, 2D-SP blocks have the CI can vary from 5.25 mm/m to 12.56 mm/m. In contrast, unreinforced type of blocks has more concentrated value of CI (in 3.1 mm/m to 5.4 mm/m).

3.4.2. Operator sensitivity to damage quantification

To address some variability concerns, two operators conducted the measurement to quantify the variability between them and ensure that any further use of the results such as machine learning training for damage quantification includes results of more than one operator. To assess the statistical significance and relevance of the results obtained from various factors, paired t-test results presented in Table 3.2, which involved 66 square segments of CI measurements from 2 operators, a strong positive correlation with a Pearson correlation coefficient of 0.95 was observed between the two variables. The average CI values obtained from the two operators were 5.74 and 5.88, with variances of 7.51 and 7.08, respectively. The calculated P-value was found to be 0.37, which exceeds the significance level of 0.05. As a result, the null hypothesis cannot be rejected, suggesting that there is no statistically significant difference between the pairs of CI measurements manually measured by 2 operators.

Table 3.2: T-test results between 2 operator's CI measurement.

	Operator 1	*Operator 2*
Mean	5.742424	5.887879
Variance	7.513557	7.088774
Observations	66	66
Pearson Correlation	0.955561	
Hypothesized Mean Difference	0	
df	65	
t Stat	-1.46028	
P(T<=t) one-tail	0.374515	
t Critical one-tail	1.668636	

3.4.3. Effect of light temperature on image analysis result

As the goal of this study was to digitize the visual inspection protocol through digitized imaging, several parameters were tested to understand their effect on image quality. The controllable parameter of artificial lighting conditions exerts a noticeable influence on image quality when compared to no artificial light being used. Optimal lighting conditions enhance crack visibility and reduce background blurring. A comparative analysis of CI and the novel measurement of total crack length (TCL – length over area, mm/cm^2) results was conducted over 72 digitized images performed under three distinct lighting conditions: warm light (yellow - 3200K), daylight (white/yellow - 4800K), and cold light (white - 5600K), as depicted in Figure 3.20. Four out of the 7 blocks were selected for this portion of the study which represent the various components with different reinforcement settings: unconfined, reinforced in one direction (1D, SP), reinforced in two directions with reactive coarse Springhill aggregate (2D, SP) or reactive Texas fine aggregate (2D - TX). A similarity in the results can be observed for each light condition where overlapping results are observed yet the overall trend is conserved. The lowest CI value is captured with the warm (yellow - Y) and daylight (white/yellow – WY) light at 3.12 mm/m while its corresponding

CI value for the cold (white -w) light is 3.75 mm/m. Meanwhile, the largest difference can be observed at between a CI of 6.0 mm/m captured with the warm (yellow – Y) light, 6.63 mm/m for the cold (white – W) light and 8.13 mm/m for the daylight (white/yellow – WY) light. As for the TCL, similar trends are observed.

a)

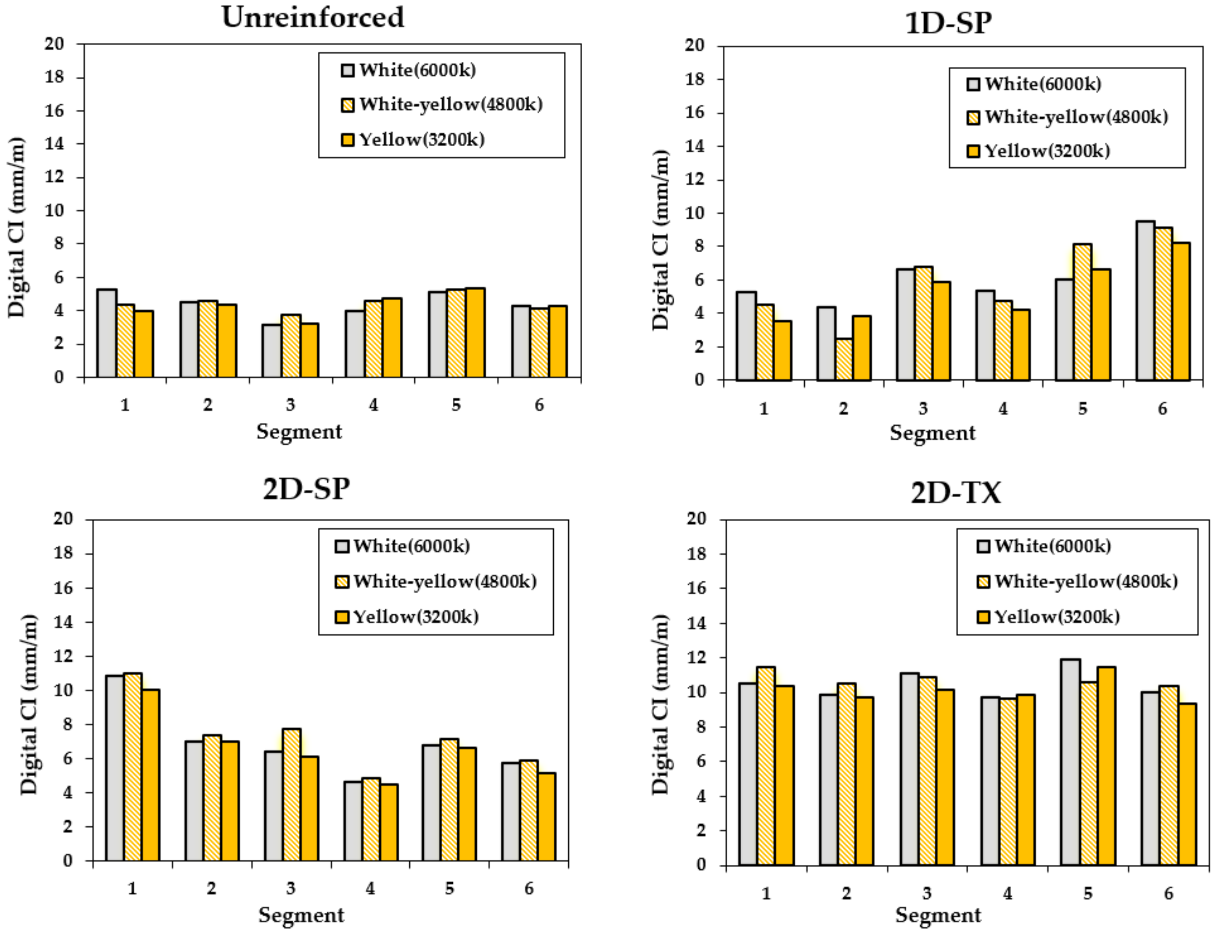

b)

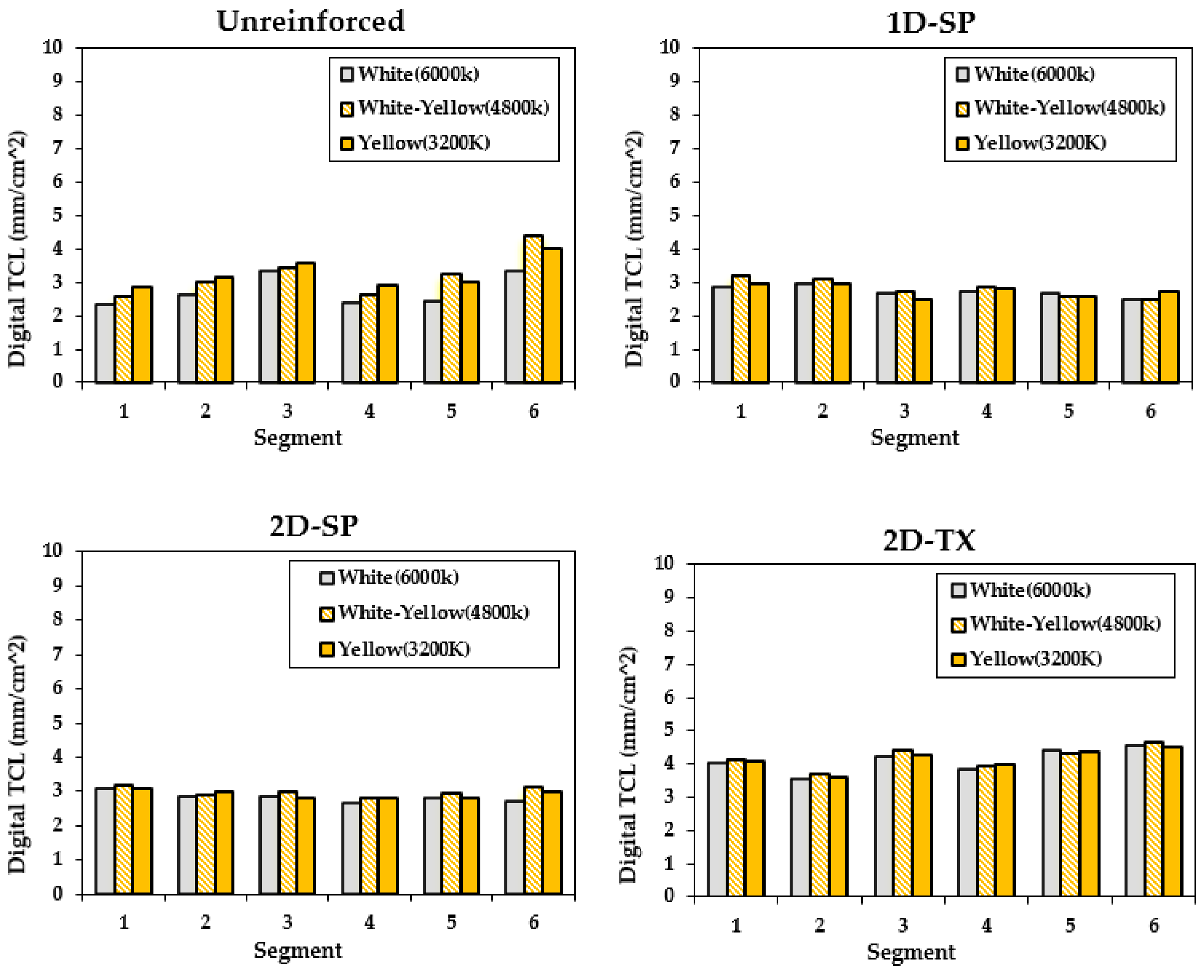

Figure 3.17: Comparison for 3 light conditions among 24 image segments. a) Cracking index (mm/m), and b) Cracking density (mm/m^2).

Due to the varied extent of damage in the concrete blocks, the CI results span from 3.0 mm/m to 12.0 mm/m, reflecting some degree of variance within the group. However, through ANOVA analysis (Table 3.3) across the three sets of data from different lighting conditions, it can be concluded that varying lighting conditions do not significantly affect the CI results obtained from image analysis. Statistically, the obtained P-Value exceeds the significance threshold of 0.05, indicating insufficient evidence to reject the null hypothesis (i.e., no significant difference in results among different lighting conditions). This conclusion is further supported by the fact that none of the "F values" exceed their corresponding "F-critical" values. Similar findings apply to the TCL image analysis results (table 4.3b). TCL values range from 2.4 mm/cm² to 4.7 mm/cm². The ANOVA analysis reveals all P-values are higher than the significance level of 0.05, reinforcing the absence of significant differences among 3 set of light condition results.

Table 3.3: a) ANOVA results for: a) Cracking index, and b) Total Crack Length.

a) ANOVA of Cracking Index in different light condition

	F	P-Value	Critical
Unreinforced	0.21	0.81	3.68
1D-SP	0.56	0.58	3.68
2D-SP	0.23	0.79	3.68
2D-TX	0.05	0.94	3.68

b) ANOVA of Total Crack Length in different light condition

	F	P-Value	Critical
Unreinforced	1.86	0.19	3.68
1D-SP	0.46	0.64	3.68
2D-SP	1.95	0.18	3.68
2D-TX	0.12	0.89	3.68

Based on the comparison, it can be concluded that the light conditions do have an influence on the results, but the effect is minimal and can be considered negligible.

3.4.4. Digital cracking index (CI)

The digital image-based analysis is a different approach to collect the measurement of cracks by using pixel-wise annotations on images. It is to be noted that only one operator conducted the digital CI for this part of the study. Figure 3.22 illustrated the digital CI results from four selected blocks (one from each configuration as aforementioned) for digital image analysis over single light conditions, compares CI results obtained through manual measurements with those derived from the image-based approach under daylight conditions using white/yellow (4800K) artificial light.

The plot represents that the CI collected from each segment varies in value by location, yet every sample closely aligns with the manual CI results as they cluster around the 1:1 line. It demonstrates a positive linear relationship with an R^2 value of 0.91, supporting the effectiveness of CI digitalization. The findings clearly indicate that measurements obtained from images follow a similar trend to the manual method since the difference falls within 10% which is the allowance of manual method due to the variation by different operators.

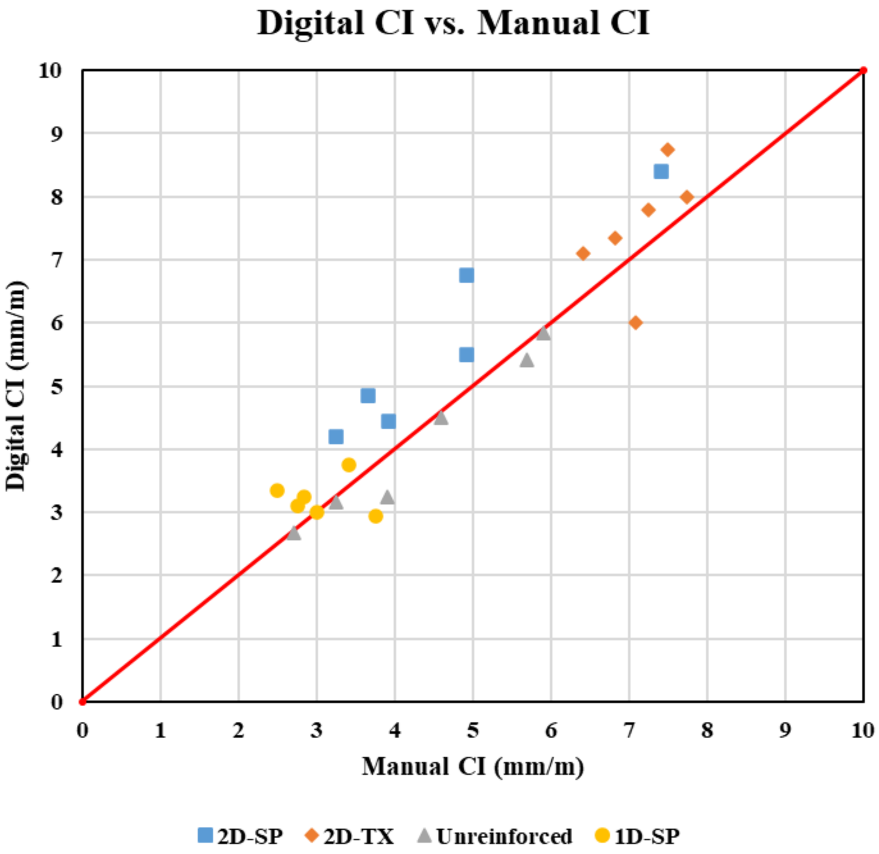

Figure 3.18: Manual vs. digital CI measurement. Marker shape differentiated by concrete reinforcement configuration: (1) reinforced in two directions (2D) with reactive coarse (SP – blue square) or fine (TX – green square) aggregate, reinforced in one direction(1D) with SP coarse aggregate (triangle), and unreinforced with SP coarse aggregate (circle).

3.4.5. Total Crack Length

Total Crack Length (TCL) serves as another quantification indicator, measuring the intensity of cracking that can be linked to the level of concrete damage by assessing the length of cracks within a unit surface area of concrete elements. In this study, TCL has been derived from the pixel amount in images using image analysis software [43], with units in mm/cm^2. The TCL values of four concrete block specimens have been compared across three different lighting conditions in the results section. Previously, it was noted that there is no significant difference in the TCL values under the three different temperature conditions of light (72 measurements). However, for unreinforced specimens, TCL values at different locations exhibit wide variation, whereas for reinforced specimens, they tend to hover around average values. The results also indicate significant differences in average TCL values across different specimen configurations.

Figure 3.23 illustrates the cracking index from digitally recorded crack widths as a function of the TCL over 24 segments under artificial light in daylight conditions (4800k). The data points show a broad distribution without generally clustering into distinct groups. Notably, Block 2D-TX (unreinforced, SP) displays the highest TCL values (3.68 mm/cm^2 to 4.68 mm/cm2) among the four blocks. TCL values within all types of blocks range widely, from 2.50 mm/cm^2 to 4.68 mm/cm^2. However, the correlation was found to have an R^2 of 0.47.

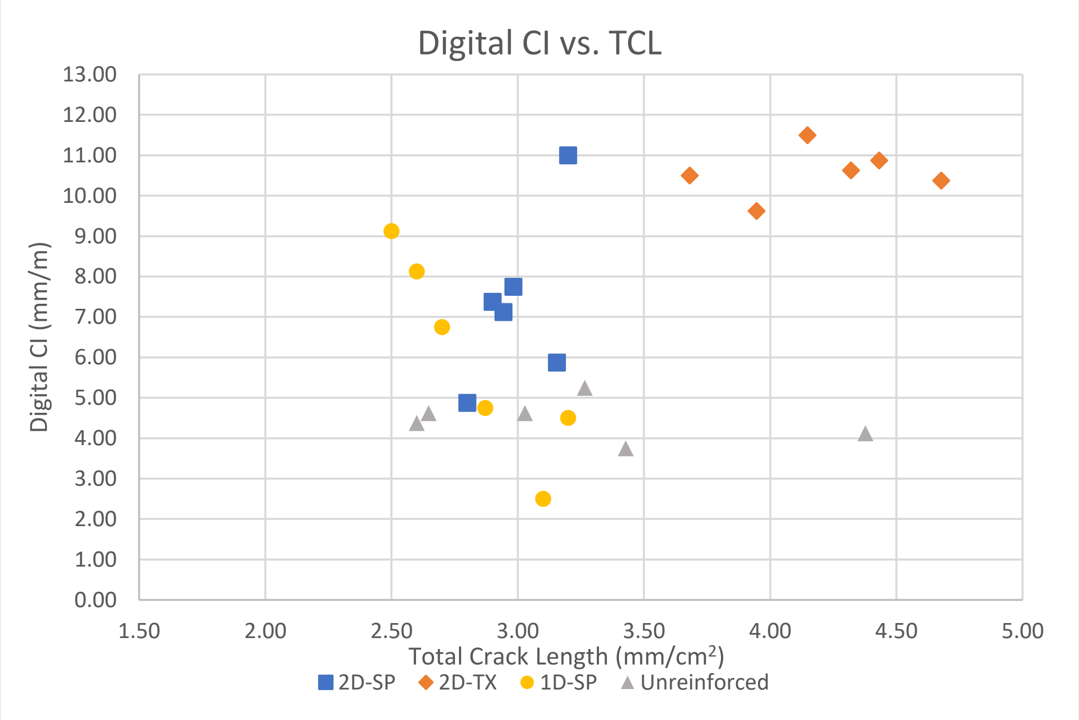

Figure 3.19: Calculated expansion level against the TCL value.

3.4.6. Crack orientation.

Through image analysis, the crack orientation can be obtained as an output which can be further illustrated through histograms to depict the most frequently observed crack directions. In Figure 3.20, a sample of histogram illustrates the percentage frequency of crack occurrences at different angles within a segment of block 1D-SP. This block is reinforced in the transverse direction and consists of reactive coarse aggregate (Springhill, SP) and non-reactive fine aggregate (natural sand). The distribution in the histogram shows a preference for the 0-degree region (horizontal) and a lesser tendency towards the 90-degree region (vertical). This suggests that more cracks are oriented horizontally rather than vertically. More crack orientation angle histogram from different segments can be found in Appendix B.2.

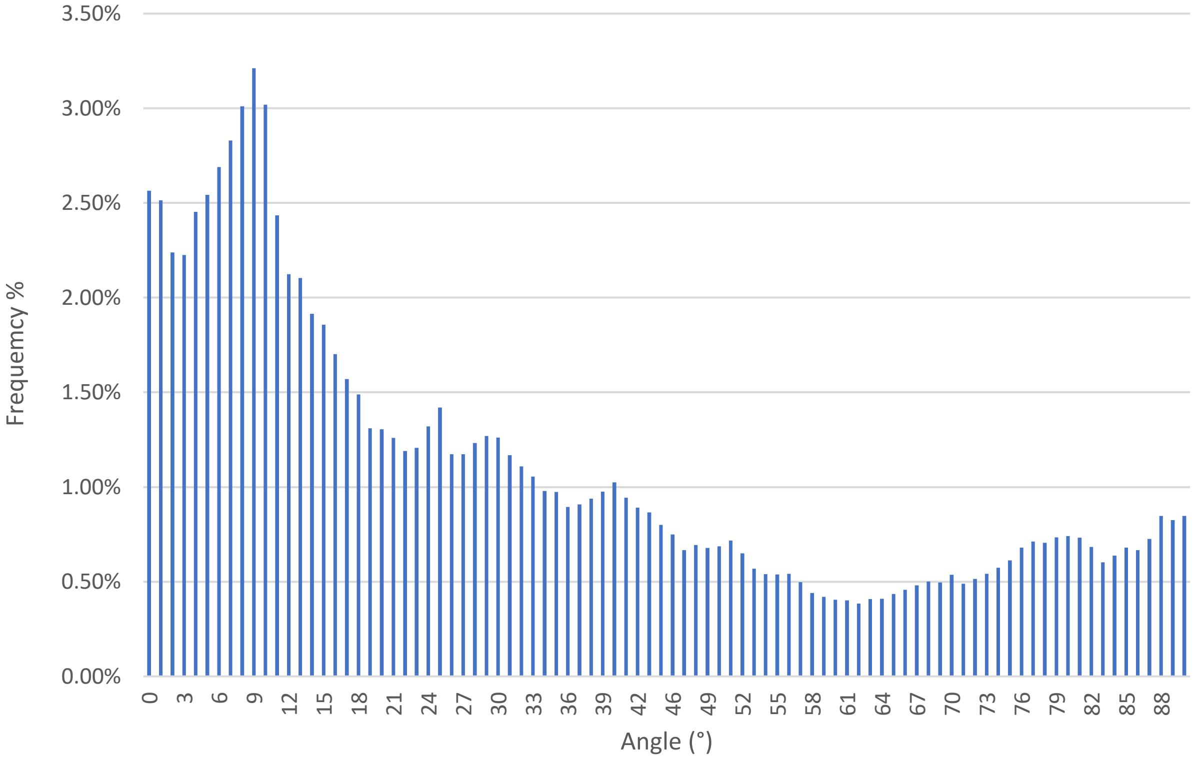

Figure 3.20: Histogram of crack orientation angle from one square segment of block B12.

In contrast, unreinforced block (B5), which is not confined by any specific direction, exhibits from the Figure 3.21, the orientation angle does not concentrate in any range of direction. The mean values closely align with the medians at around 45 degrees, suggesting a distribution of cracks that is not skewed towards either the horizontal or vertical direction.

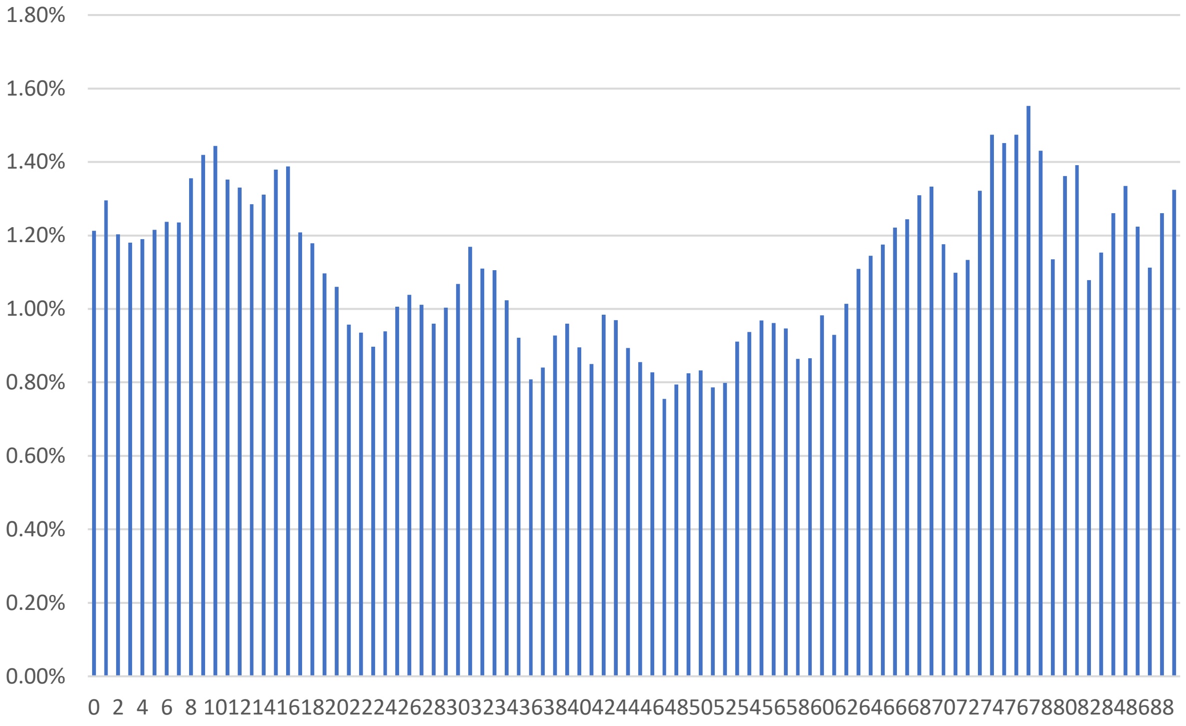

Figure 3.21: Histogram of crack orientation angle from one square segment of block B5.

The mean crack orientation values provided in Table 3.4 illustrates the characteristics of cracks propagation in the reinforced blocks (). These values indicate that the majority of cracks have angles of less than 45 degrees. This implies that most of the cracks are oriented vertically meanwhile, block B5 (unreinforced) exhibits an average crack orientation angle close to 45 degrees. This highlights the fact that crack propagation in this block exhibits an anisotropic feature without restraint in any specific direction.

Table 3.4:Mean value summary of average crack orientation angles from 5 concrete surfaces (in degrees)

Segment	1	2	3	4	5	6	***AVERAGE***
B2D21B	33.32	40.23	25.17	34.82	43.70	35.00	35.37
B12	36.99	35.91	30.38	44.74	43.35	37.83	38.20
B2D29B	40.22	26.09	34.34	33.93	30.34	33.77	33.12
B5A	44.60	44.51	56.42	38.39	42.82	45.99	45.46
B5B	39.45	47.56	41.91	41.04	48.18	39.03	42.86

3.5. Discussion

3.5.1. Variability to consider when digitizing.

It is expected that the highest degrees of variability will be observed during manual operations as more factors can influence the variability as opposed to measurements being conducted while using digitized images. This reasoning stems from the variables often met when performing manual operations on site or in a laboratory in which human error is more prominent. Therefore, cconcerns from operator variability and use of artificial light have often been raised due to the nature of the conducted on-site visual inspections. Through validation in this study, the CI conducted on-site (called “manual CI” in this study) was not deemed sensitive to operator variability when both operators work alongside each other, under the same conditions. Operator variability remained at 0.2 mm/m which is considered negligeable such that, the operators’ variability is lower than that of the range used to indicate the volumetric changes around 1.85 mm/m per year [14]. Meanwhile, it was earlier stated that the artificial light condition had negligeable effect on the outcomes. However, when digitizing the CI, variability may be observed due to image resolution thus a set of t-test results were conducted (Table 3.5). The CI was further divided into the two directions. The average value for manual CI is 3.55 mm/m, while for digital CI, it is 3.90 mm/m. The difference between these averages yields a p-value of 0.051, which is just on the border of the significance level of 0.05. Similarly, a p-value of 0.51 was found in the vertical CI results from both measurement approaches. Since both p-values are very close to reaching statistical significance, it suggests that there is a small chance of observing a significant difference in all measurements. Obtaining more convincing results may require a larger sample size.

Table 3.5: T-test results for comparison between CI results from digital and manual method

Horizontal Direction	*Manual*	*Digital*
Mean	3.55	3.90
Variance	3.01	3.50
Observations	24.00	24.00
Pearson Correlation	0.92	
Hypothesized Mean Difference	0.00	
df	23.00	
t Stat	-2.30	
P(T<=t) two-tail	0.05	
t Critical two-tail	2.07	

Vertical Direction	*Manual*	*Digital*
Mean	1.25	1.29
Variance	0.56	0.56
Observations	24.00	24.00
Pearson Correlation	0.91	
Hypothesized Mean Difference	0.00	
df	23.00	
t Stat	-0.67	
P(T<=t) two-tail	0.05	
t Critical two-tail	2.07	

The conditions affecting the results during each operation are indeed different such that digital CI measurements can be influenced by image quality provided by the camera itself or the screen used to measure such cracks. It is expected that lower image quality will provide a higher variability while a better image quality will provide less variability as the crack features will be more resemblant of what is observed by eye. A parametric study using various image qualities would help to further define the ranges of uncertainty. Furthermore, this correlation is for the observed surfaces used in this study which does not include lower degrees of damage, different types of damage other than ASR and represent laboratory-made and exposed concrete. Further images following the proposed standard protocol through this study are required to refine these correlations and the dataset to draw conclusions beyond the points evaluated in this study. Nevertheless, the CI served as an efficient tool to measure the ability to transfer from manual to digital measurements of cracking at the surface of concrete.

3.5.2. Capturing damage with crack directionality in reinforced concrete

Observations indicate that cracks in unreinforced blocks display a random distribution, while reinforced blocks tend to have more cracks oriented horizontally with wider openings. Considering the apparent observable crack directionality, the CI was divided into two directions to capture horizontal cracking and vertical cracking. The following discussion will explore the impact of confinement on crack distribution and the resulting cracking index, thereby enhancing the effectiveness of image analysis to correlated with manual method for CI measurement. It is to be noted that although the CI calculates cracks in two directions, its final output is a one-dimensional value such that crack widths are measured along a line.

Figure 3.25 presents the average directional CI results from both operators plotted along a 1:1 line, this plot represents that cracking is more significant in the horizontal direction. Note that the x-axis represents the crack CI measurement from cracks aligned in horizontal direction, and vice versa.

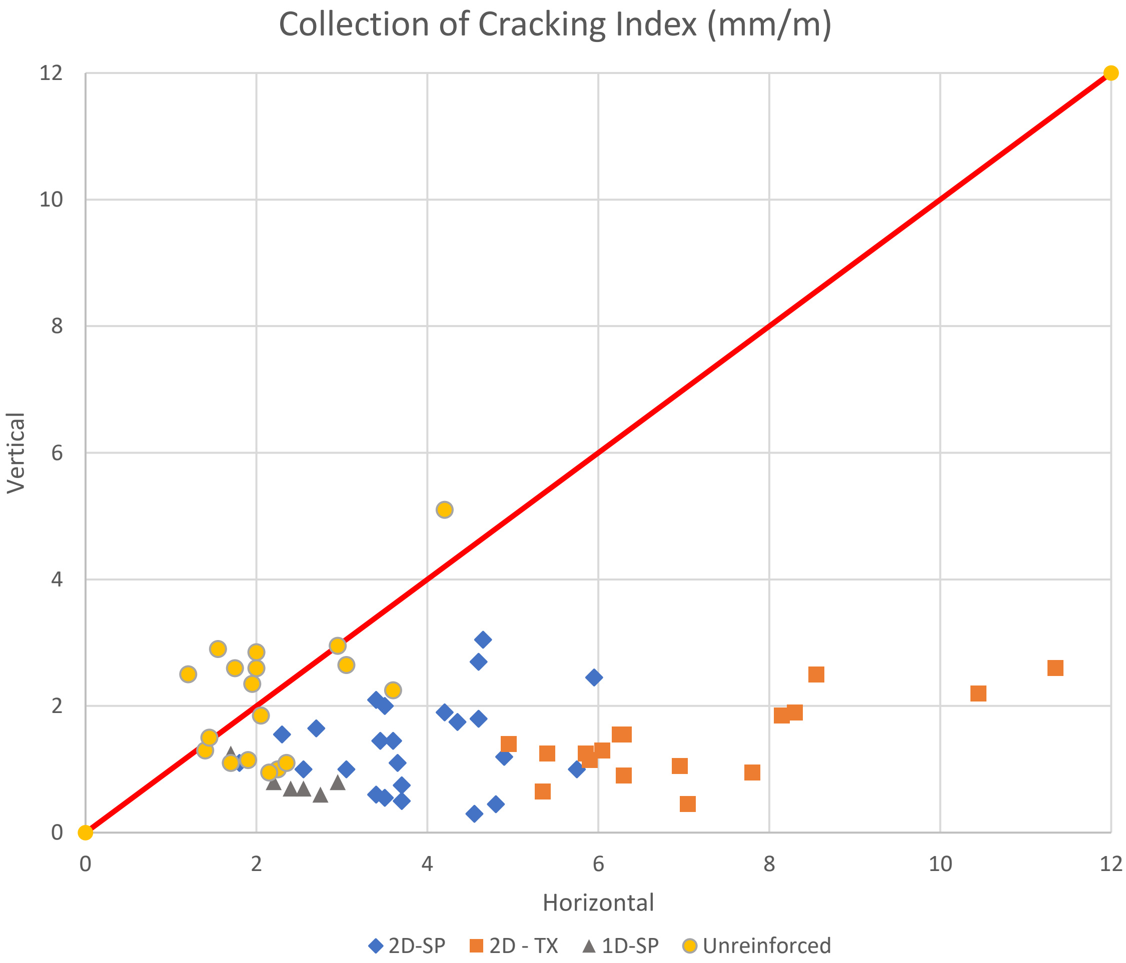

Figure 3.22: Plot of CI measurement collection Vertical vs. Horizontal in mm/m, digitally collected from 4 types of blocks.

By evaluating the data clusters where different types of blocks were grouped to assess the impact of reinforcement on crack patterns, it can be observed that all data points from blocks without reinforcement cluster closely around the 1:1 line, with a highest CI value of 4.20 mm/m for vertical cracking, 5.10 mm/m for horizontal cracking. This suggests that their horizontal CI values closely align with their vertical CI values since these blocks can expand in all directions without restraint. In contrast, all reinforced blocks exhibit CI values in horizontal cracks that are much greater than in vertical cracks. The block reinforced in one direction and has the average CI value at 2.43 mm/m for horizontal cracking, 0.81 mm/m vertical cracking, which are lower than the value observed on blocks reinforced in 2 directions, in both vertical and horizonal cracking directions. For blocks reinforced in 2 directions, 2D-SP have their average CI at 3.86 mm/m in horizontal cracking and 1.39 mm/m in vertical cracking, while 2D-TX have even larger crack width open with 7.458 mm/m in horizontal and 1.439 mm/m in vertical cracking directions.

Based on the 132 observations, it is evident that the average range of CI values obtained by image analysis by horizontal cracking direction is larger than the average range of CI values by vertical cracking direction, especially for reinforced concrete blocks. In figure 3.23, the CI and expansion values of 1D-SP, 2D-TX and 2D-SP type blocks are significantly higher than those of unreinforced blocks. This observation reveals that the presence of reinforcement does impact and leads to increased crack length, width and expansion along the reinforced direction. Corroborating existing literature [9, 49, 50], expansion measurements conducted on different surfaces of the reinforced blocks indicate that reinforced blocks (1D-SP, 2D-SP, and 2D-TX) take longer to achieve the same expansion level as unreinforced blocks. Additionally, under identical levels of expansion, crack openings become larger due to the confinement setting as the propagation of induced expansion can shift from reinforced directions to directions with less or no reinforcement, leading to increased expansion in the direction with the least reinforcement (perpendicular to the main reinforcing bars). Through the cracking orientation analysis, preferential cracking directions are observed with respect to the reinforcements. Therefore, in cases of reinforced concrete presenting cracking directionality, quantifying the cracking orientation may help to refine models used to predict the CI.

3.5.3. Image analysis for damage evaluation

As the primary goal of this research is to automate damage quantification through imaging, the first step was to understand how the machine/algorithm detects features such as cracks and how well. Further training/study is ongoing through this iterative process. However, it was concluded that crack identification must come before being able to measure those considered in the CI calculation such that a crack can only be measured upon its detection. Therefore, a new metric was considered top quantify the intensity of cracking such as the Total Crack Length (TCL) which takes into account the length of cracks (in one dimension) over an area (2 dimensions). The TCL can then be used to measure the machine's ability to measure the length of cracks. While annotated images are used for training of the machine, they can further be used to assess the metrics best describing damage in this context through image analysis.

The TCL alone cannot measure crack directionality therefore, it was compared against the vertical and horizontal CIs, as illustrated Figure 3.26. By comparing the slope of the trendline, TCL may not be able to represent a good correlation with either vertical or horizontal CI value, this can be proved by the residual value analysis displayed in Figure 3.24. As the TCL increases, the value of CI between two directions shows a significant difference, indicating the TCL may not be capable to represent the damage extent in either direction. Moreover, the correlations show an R^2 of 0.39

for the horizontal cracking and 0.06 for the vertical cracking, which is considered as a poor correlation.

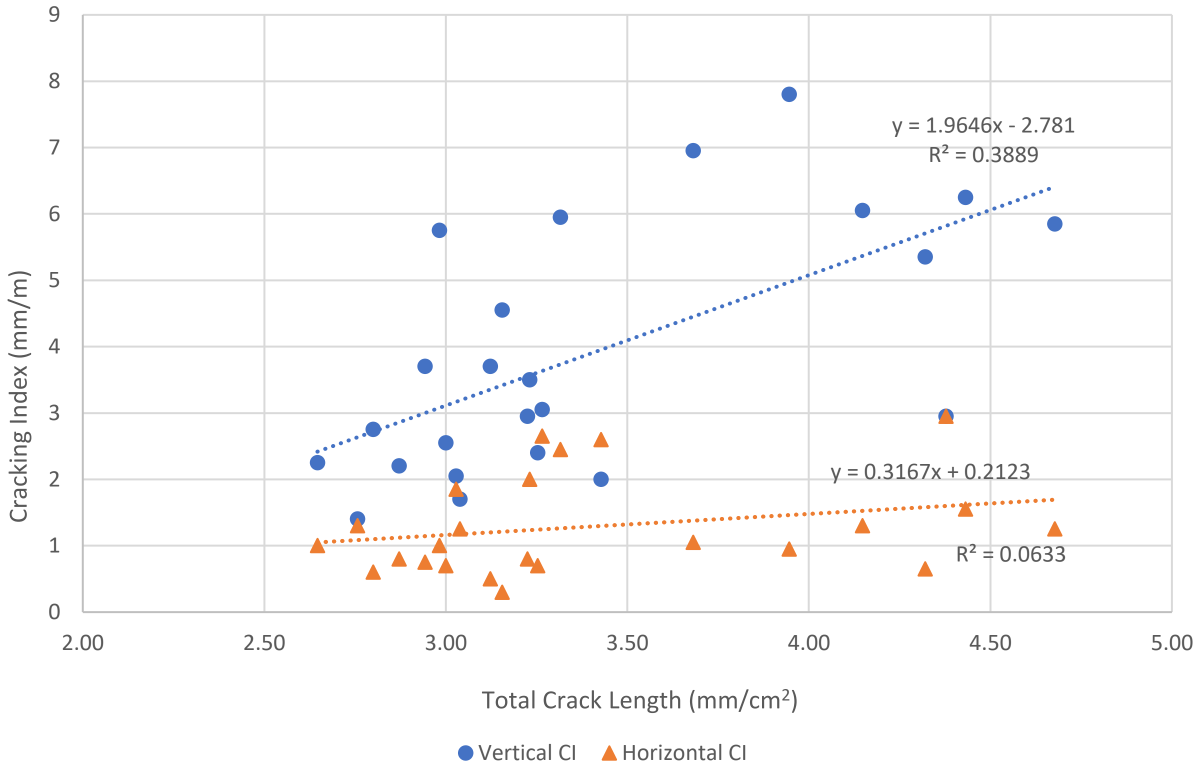

Figure 3.23: Divided CI as a function of TCL.

Further consideration of the influence of crack direction on the damage pattern can be discussed in this work. The orientation angle of cracks can serve as potential indicators. As aforementioned, the configuration of reinforcement in certain blocks may contribute to an increased prevalence of surface cracks in the horizontal direction.

Results of crack orientation displayed in section 3.4.6 claims that the proportion of crack orientation reveals the possibility of indicating the overall crack propagation direction, thus provides a potential solution to convert TCL to a directional CI by assigning coefficients according to the angle within a certain range corresponding to the direction. In this study, following Eq. 3.2

and Eq. 3.3 are defined though linear regression by the image analysis results output within this work.

$$CI_v = 3.271a_v * CD - 0.8698 \qquad \text{Equation 3.2}$$

$$CI_h = 1.7653a_h * CD - 0.3718 \qquad \text{Equation 3.3}$$

Where a_v a_h is the total percentage of crack orientation from 0º to 30º and 60º to 90º, representing cracks propagating in horizontal and vertical direction, respectively. TCL is the Total Crack Length in mm/cm^2, CI$_v$ CI$_h$ are the predicted CI results for vertical and horizontal direction.

Relevant data is further presented in Appendix C. The performance of the regression model can be assessed through residual analysis, as depicted in Figure 3.24 and Figure 3.25. The residual values range from -2.0 mm/m to +2.3 mm/m for the vertical direction and from -1.0 mm/m to +1.0 mm/m for the horizontal direction without a trend of heteroscedasticity observed. Notably, the histograms of the residual values in both directions closely approximate a normal distribution. This suggests that the prediction model (Eq. 3.2 and 3.3) has a good regression with the ground truth values.

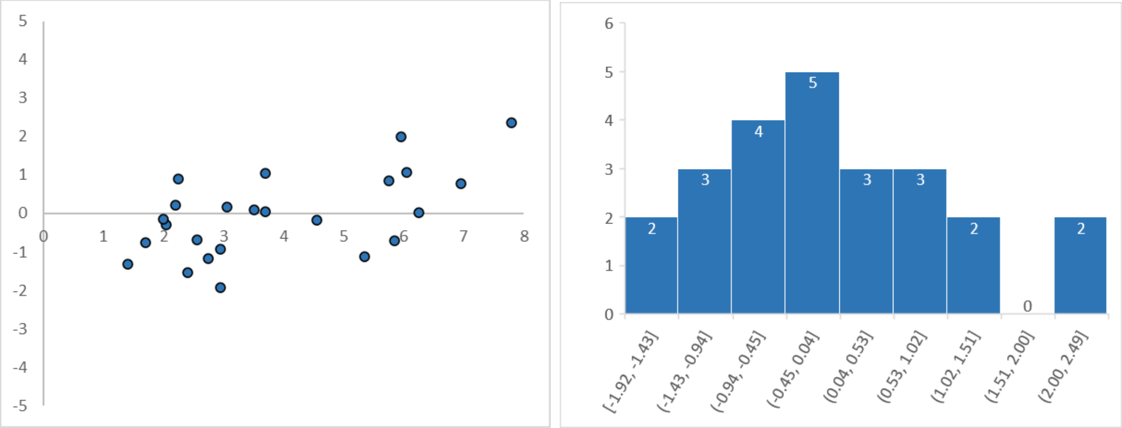

Figure 3.24:Residual analysis, vertical CI prediction though TCL and crack orientation.

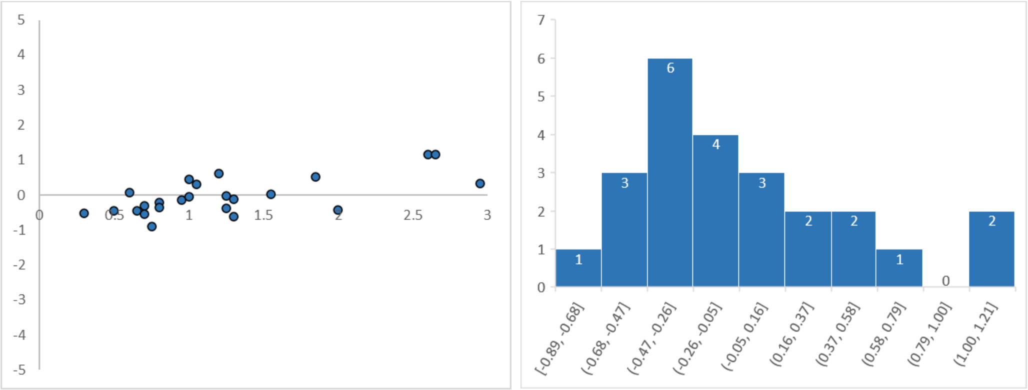

Figure 3.25: Residual analysis, vertical CI prediction though TCL and crack orientation.

The CI, TCL, and crack orientation angle represent three distinct parameters that do not exhibit a direct relationship. Nevertheless, when considering TCL and crack orientation collectively, they can jointly characterize crack behavior in terms of distribution and quantity. Their combined analysis can reasonably describe the cracking intensity in their respective directions, akin to the role CI plays. Additional findings presented in Table 3.6 provide compelling evidence to assess the model's predictive capability. Based on the results of paired t-tests, the predictive outcomes of CI closely align with manual CI results of horizontal cracking, yielding an average p-value of 0.96 and correlation coefficients of 0.82. suggesting that there is no significant difference between the predicted and observed values. Similarly, in the vertical direction, the p-value is 0.90 with a correlation coefficient of 0.79, supporting a similar conclusion of a positive result, 2 plots present in Figure 3.26, is comparing the predicted CI results vs. manual CI in both directions for better determine the regression performance visually.

Table 3.6: The t-test results between predict CI and manual CI results.

t-Test: Paired Two Sample for Means

Horizontal	*Variable 1*	*Variable 2*
Mean	3.90	3.90
Variance	3.50	2.24
Observations	24.00	24.00
Pearson Correlation	0.80	
Hypothesized Mean Difference	0.00	
df	23.00	
t Stat	0.00	
P(T<=t) two-tail	0.96	
t Critical two-tail	2.07	

Vertical	*Variable 1*	*Variable 2*
Mean	1.24	1.23
Variance	0.50	0.20
Observations	24.00	24.00
Pearson Correlation	0.74	
Hypothesized Mean Difference	0.00	
df	23.00	
t Stat	0.07	
P(T<=t) two-tail	0.94	
t Critical two-tail	2.07	

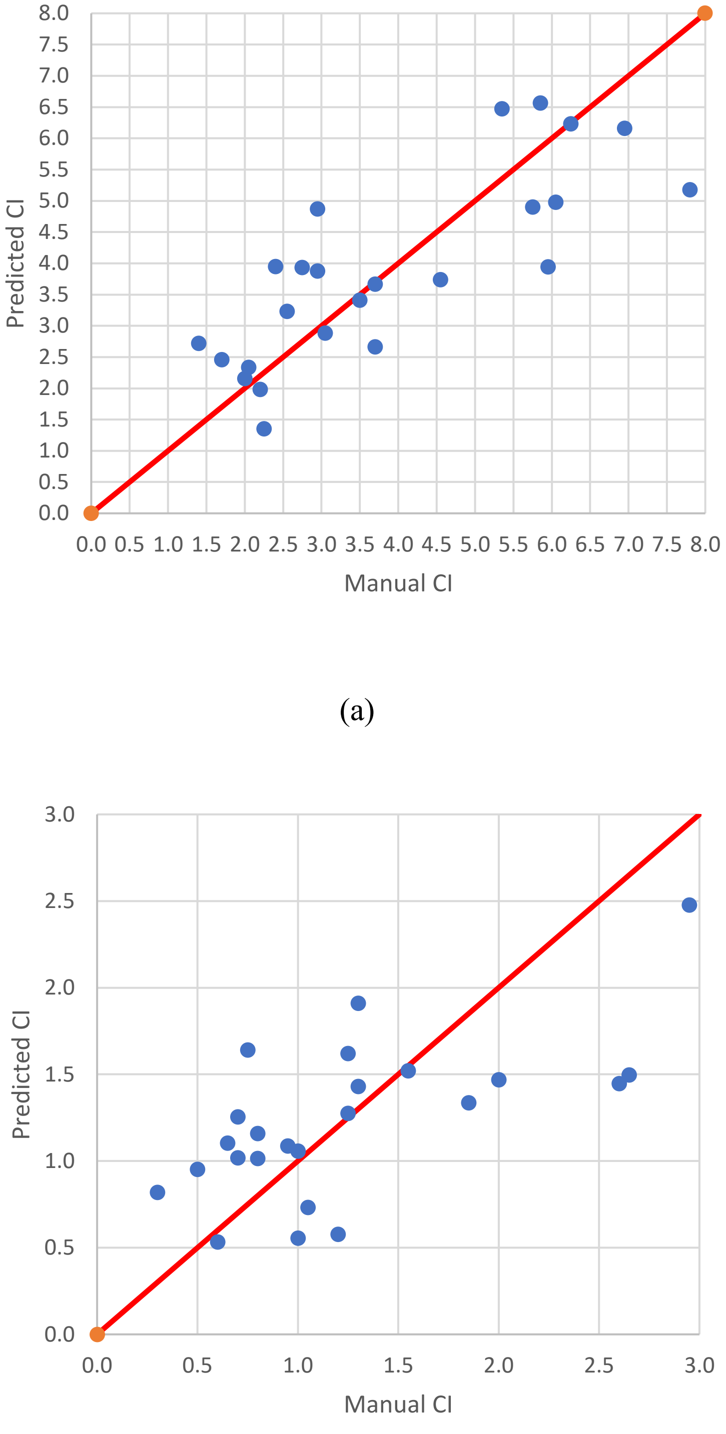

(a)

(b)

Figure 3.26: CI value predicted through TCL-orientation model in the a) horizontal b) vertical directions.

Through the analysis presented above, the combination of Total Crack Length and crack orientation has proven capable of summarizing damage extent results similar to the output of CI under selected concrete surfaces. Since ASR development involves anisotropic propagation in reinforced concrete members, accurately extracting damage from randomly distributed crack patterns can be challenging. However, the model introduced in this section successfully integrates crack quantity and crack propagation direction across the entire area of interest to correlate with an already established metric, the CI, for evaluating crack damage in two directions across the damaged surface.

Chapter 4 : Conclusion and future recommendations

Digitalization of visual inspections is becoming the standard practice in many applications such as assessing the cracking of concrete surfaces. Among the mechanisms causing cracking to concrete, alkali-silica reaction (ASR) causes a distinct map-cracking pattern in which its intensity is quantified to evaluate the overall level of deterioration and its rate. The cracking index (CI) was initially developed as a means to measure this cracking intensity in a practical manner in the field. Since its development, the availability and accessibility of high-resolution digital cameras have transformed visual inspections in which the assessment could be performed on a computer as opposed to on the site thus, reducing some of the variables encountered through such operations. Moreover, the use of automated technologies such as using machine learning to automatically detect, and measure crack characteristics has emerged in the last decade. The following main conclusions are therefore presented as follows:

- Training an automated crack detection model using a machine learning system presents an initial major challenge when quantitatively annotated datasets are unavailable. This challenge prompted the development of a novel procedure to acquire, process, and analyze images for quantitative purposes. This procedure enables the creation of quantitatively annotated datasets featuring cracks on concrete surfaces with known widths (along the perimeter of the image) and known areas for the region of interest (ROI).

- Machine learning is inherently iterative. However, beyond a qualitative evaluation of its ability to detect cracks, more nuanced performance metrics are essential, especially if the aim is to quantify characteristics of entities in the image, such as cracks. As the system learns from annotated images, these same images serve as benchmarks for assessing crack patterns via image analysis. The system, in its learning phase, doesn't detect every annotated crack, meaning it can't measure what it doesn't detect. To address this, image analysis was leveraged to establish a metric called 'Total Crack Length', designed to evaluate the machine's performance starting with crack detection. This metric quantifies cracking intensity by computing the total crack length relative to the analyzed area.

- Variability between two operators was evaluated in the CI computation and was found to be negligible. Among other variable parameters that could be controlled in this study, artificial lighting was probably the most significant factor. All other variables were kept constant, such as the distance between the camera lens and the block surface, the camera zoom set to its minimal value, position in the laboratory, angles adjusted for perspective distortions, and area of analysis. Using three different light settings (all set to their maximum intensity to further reduce variability), image analysis was performed using the digital cracking index (where crack widths were measured on images) and the Total Crack Length (where cracks were annotated/traced on images). It was thus revealed that the lighting conditions did not significantly influence the outcomes. Furthermore, converting the cracking index into a digital technique displayed a strong correlation, thereby validating the digitalization process.

- A thorough protocol for image acquisition, processing and analysis was developed throughout this project to facilitate the creation of similar datasets. Datasets of quantifiable features of concrete cracking are non-existent and crucial towards machine learning developments. The dataset can further serve as a calibration for other developers and the application of the protocol can extend lend itself beyond cracks in concrete caused by ASR.

- By evaluating the expansion as a function of the cracking index, a linear trend was observed however, distinction between the various reinforcement configurations were not apparent when compared to digitally measured crack widths to calculate the cracking index and the Total Crack Length. The division of the cracking index into horizontal and vertical directions aids in comprehending the viability of crack detection through image analysis and enhance the influence of crack directionality on predicting the cracking index using image analysis via total crack length. Nevertheless, the two linear models formulated in this project were constrained by sample size limitations and are only applicable to forecasting crack indices for the concrete samples utilized in this study. Thus, they do not assure a quantitative assessment of crack opening size for all concrete structure surfaces.

- The machine learning model trained by Mask R-CNN that motivated this study is not yet fully optimized and cannot be effectively applied to real structures for quantitative assessment of concrete surface cracks. The primary limitation stems from the dataset created for this project, which comprises only a small number of sample concrete images from a controlled laboratory environment. However, the model requires a larger and more diverse image dataset for robust training. For future research, it is recommended to expand the dataset size by collecting images of actual concrete structures affected by ASR, following the procedures outlined in this project. Additionally, it is highly advisable to verify and optimize the dataset's quality by testing it with different operators and using various image acquisition instruments to migrate the variation from different factors.

References

[1] L.F.M. Sanchez, Contribution to the assessment of damage in aging concrete infrastructures affected by alkali-aggregate reaction, Université Laval, 2014.

[2] E.O. Fanijo, J.T. Kolawole, A. Almakrab, Alkali-silica reaction (ASR) in concrete structures: Mechanisms, effects and evaluation test methods adopted in the United States, Case Studies in Construction Materials 15 (2021) e00563. https://doi.org/10.1016/j.cscm.2021.e00563.

[3] L.F.M. Sanchez, B. Fournier, D. Mitchell, J. Bastien, Condition assessment of an ASR-affected overpass after nearly 50 years in service, Construction and Building Materials 236 (2020) 117554. https://doi.org/10.1016/j.conbuildmat.2019.117554.

[4] M.D. Cohen, J. Olek, W.L. Dolch, Mechanism of plastic shrinkage cracking in portland cement and portland cement-silica fume paste and mortar, Cement and Concrete Research 20 (1990) 103–119. https://doi.org/10.1016/0008-8846(90)90121-D.

[5] A. Zahedi, C. Trottier, L.F.M. Sanchez, M. Noël, Condition assessment of alkali-silica reaction affected concrete under various confinement conditions incorporating fine and coarse reactive aggregates, Cement and Concrete Research 153 (2022) 106694. https://doi.org/10.1016/j.cemconres.2021.106694.

[6] B. Fournier, M.-A. Bérubé, M. Thomas, Report on the Diagnosis, Prognosis, and Mitigation of Alkali-Silica Reaction (ASR) in Transportation Structures, (2010) 156.

[7] A. Zahedi, L.F.M. Sanchez, M. Noël, Appraisal of visual inspection techniques to understand and describe ASR-induced development under distinct confinement conditions, Construction and Building Materials 323 (2022) 126549. https://doi.org/10.1016/j.conbuildmat.2022.126549.

[8] B. Kim, S. Cho, Image-based concrete crack assessment using mask and region-based convolutional neural network, Struct Control Health Monit (2019) e2381. https://doi.org/10.1002/stc.2381.

[9] F. Thériault, M. Noël, L.F.M. Sanchez, Simplified approach for quantitative inspections of concrete structures using digital image correlation, Engineering Structures 252 (2022) 113725. https://doi.org/10.1016/j.engstruct.2021.113725.

[10] Y.-A. Hsieh, Y.J. Tsai, Machine Learning for Crack Detection: Review and Model Performance Comparison, J. Comput. Civ. Eng. 34 (2020) 04020038. https://doi.org/10.1061/(ASCE)CP.1943-5487.0000918.

[11] A. Mohan, S. Poobal, Crack detection using image processing: A critical review and analysis, Alexandria Engineering Journal 57 (2018) 787–798. https://doi.org/10.1016/j.aej.2017.01.020.

[12] H.S. Munawar, A.W.A. Hammad, A. Haddad, C.A.P. Soares, S.T. Waller, Image-Based Crack Detection Methods: A Review, Infrastructures 6 (2021) 115. https://doi.org/10.3390/infrastructures6080115.

[13] T.E. Stanton, Expansion of Concrete through Reaction between Cement and Aggregate, T. Am. Soc. Civ. Eng. 107 (1942) 54–84. https://doi.org/10.1061/TACEAT.0005540.

[14] A. Zahedi, C. Trottier, L.F.M. Sanchez, M. Noël, Evaluation of the induced mechanical deterioration of alkali-silica reaction affected concrete under distinct confinement conditions through the Stiffness Damage Test, Cement and Concrete Composites 126 (2022) 104343. https://doi.org/10.1016/j.cemconcomp.2021.104343.

[15] J.A. Farny, B. Kerkhoff, Diagnosis and Control of Alkali-Aggregate Reactions in Concrete, (n.d.).
[16] M.T. de Grazia, Contribution to the understanding of fresh and hardened state properties of low cement concrete, University of Ottawa, 2018.
[17] S. Multon, F. Toutlemonde, Effect of moisture conditions and transfers on alkali silica reaction damaged structures, Cement and Concrete Research 40 (2010) 924–934. https://doi.org/10.1016/j.cemconres.2010.01.011.
[18] H. Ahmed, A. Zahedi, L.F.M. Sanchez, P.-L. Fecteau, Condition assessment of ASR-affected reinforced concrete columns after nearly 20 years in service, Construction and Building Materials 347 (2022) 128570. https://doi.org/10.1016/j.conbuildmat.2022.128570.
[19] N. Smaoui, M.-A. Bérubé, B. Fournier, B. Bissonnette, B. Durand, Evaluation of the expansion attained to date by concrete affected by alkali–silica reaction. Part I: Experimental study, Can. J. Civ. Eng. 31 (2004) 826–845. https://doi.org/10.1139/l04-051.
[20] L.F.M. Sanchez, T. Drimalas, B. Fournier, D. Mitchell, J. Bastien, Comprehensive damage assessment in concrete affected by different internal swelling reaction (ISR) mechanisms, Cement and Concrete Research 107 (2018) 284–303. https://doi.org/10.1016/j.cemconres.2018.02.017.
[21] CANADIAN STANDARDS ASSOCIATION, A864-00 (R2005): Guide to the Evaluation and Management of Concrete Structures Affected by Alkali-Aggregate Reaction, (2005).
[22] E. Fathalla, Y. Tanaka, K. Maekawa, Effect of Crack Orientation on Fatigue Life of Reinforced Concrete Bridge Decks, Applied Sciences 9 (2019) 1644. https://doi.org/10.3390/app9081644.
[23] L. Kristufek, A. Zahedi, D. Tawil, L. Sanchez, B. Martin-Perez, M. Noël, Preliminary evaluation of Pier cap from an ASR affected bridge in Central Canada, MATEC Web Conf. 364 (2022) 03005. https://doi.org/10.1051/matecconf/202236403005.
[24] P. Oke, Environmental Impact Assessment Registration: Mactaquac Life Achievement Project, (2023).
[25] P. Cotič, E. Niederleithinger, V. Bosiljkov, Z. Jagličić, NDT Data Fusion for the Enhancement of Defect Visualization in Concrete, KEM 569–570 (2013) 175–182. https://doi.org/10.4028/www.scientific.net/KEM.569-570.175.
[26] 221.1R-98 State-of-the-Art Report on Alkali-Aggregate Reactivity, (n.d.).
[27] L.F.M. Sanchez, B. Fournier, M. Jolin, J. Bastien, Evaluation of the stiffness damage test (SDT) as a tool for assessing damage in concrete due to ASR: Test loading and output responses for concretes incorporating fine or coarse reactive aggregates, Cement and Concrete Research 56 (2014) 213–229. https://doi.org/10.1016/j.cemconres.2013.11.003.
[28] J.P. Busel, Specification for carbon and glass fiber-reinforced polymer bar materials for concrete reinforcement, 1st ed, American Concrete Institute, Farmington Hills, MI, 2008.
[29] C. Trottier, R. Ziapour, A. Zahedi, L.F.M. Sanchez, F. Locati, Microscopic characterization of alkali-silica reaction (ASR) affected recycled concrete mixtures induced by reactive coarse and fine aggregates, Cement and Concrete Research 144 (2021) 106426. https://doi.org/10.1016/j.cemconres.2021.106426.
[30] L.F.M. Sanchez, B. Fournier, T. Drimalas, J. Bastien, D. Mitchell, M. Noel, SEMI-QUANTITATIVE CONDITION ASSESSMENT OF CONCRETE DISTRESS THROUGH THE DAMAGE RATING INDEX, (n.d.).

[31] M.A. El-Reedy, Assessment, evaluation, and repair of concrete, steel, and offshore structures, First edition, CRC Press, Boca Raton, FL, 2019.

[32] C. Koch, K. Georgieva, V. Kasireddy, B. Akinci, P. Fieguth, A review on computer vision based defect detection and condition assessment of concrete and asphalt civil infrastructure, Advanced Engineering Informatics 29 (2015) 196–210. https://doi.org/10.1016/j.aei.2015.01.008.

[33] Y.-J. Cha, W. Choi, O. Büyüköztürk, Deep Learning-Based Crack Damage Detection Using Convolutional Neural Networks: Deep learning-based crack damage detection using CNNs, Computer-Aided Civil and Infrastructure Engineering 32 (2017) 361–378. https://doi.org/10.1111/mice.12263.

[34] U.H. Billah, A. Tavakkoli, H.M. La, Concrete Crack Pixel Classification Using an Encoder Decoder Based Deep Learning Architecture, in: G. Bebis, R. Boyle, B. Parvin, D. Koracin, D. Ushizima, S. Chai, S. Sueda, X. Lin, A. Lu, D. Thalmann, C. Wang, P. Xu (Eds.), Advances in Visual Computing, Springer International Publishing, Cham, 2019: pp. 593–604. https://doi.org/10.1007/978-3-030-33720-9_46.

[35] S. Kabir, Imaging-based detection of AAR induced map-crack damage in concrete structure, NDT & E International 43 (2010) 461–469. https://doi.org/10.1016/j.ndteint.2010.04.007.

[36] S.C. Radopoulou, I. Brilakis, Automated Detection of Multiple Pavement Defects, J. Comput. Civ. Eng. 31 (2017) 04016057. https://doi.org/10.1061/(ASCE)CP.1943-5487.0000623.

[37] S.B. Kotsiantis, Supervised Machine Learning: A Review of Classification Techniques, (n.d.).

[38] X. Wu, V. Kumar, J. Ross Quinlan, J. Ghosh, Q. Yang, H. Motoda, G.J. McLachlan, A. Ng, B. Liu, P.S. Yu, Z.-H. Zhou, M. Steinbach, D.J. Hand, D. Steinberg, Top 10 algorithms in data mining, Knowl Inf Syst 14 (2008) 1–37. https://doi.org/10.1007/s10115-007-0114-2.

[39] P. Savino, F. Tondolo, Automated classification of civil structure defects based on convolutional neural network, Front. Struct. Civ. Eng. 15 (2021) 305–317. https://doi.org/10.1007/s11709-021-0725-9.

[40] S. Li, X. Zhao, Image-Based Concrete Crack Detection Using Convolutional Neural Network and Exhaustive Search Technique, Advances in Civil Engineering 2019 (2019) 1–12. https://doi.org/10.1155/2019/6520620.

[41] Chambo, S, Results with AigleRN images, (n.d.). https://www.irit.fr/~Sylvie.Chambon/AigleRN.html.

[42] A. Ahmadi, S. Khalesi, M. Bagheri, Automatic road crack detection and classification using image processing techniques, machine learning and integrated models in urban areas: A novel image binarization technique, (n.d.).

[43] S. Kulkarni, S. Singh, D. Balakrishnan, S. Sharma, S. Devunuri, S.C.R. Korlapati, CrackSeg9k: A Collection and Benchmark for Crack Segmentation Datasets and Frameworks, (2022). http://arxiv.org/abs/2208.13054 (accessed October 24, 2023).

[44] A. Krizhevsky, I. Sutskever, G.E. Hinton, ImageNet classification with deep convolutional neural networks, Commun. ACM 60 (2017) 84–90. https://doi.org/10.1145/3065386.

[45] E. Guerra, J. De Lara, A. Malizia, P. Díaz, Supporting user-oriented analysis for multi-view domain-specific visual languages, Information and Software Technology 51 (2009) 769–784. https://doi.org/10.1016/j.infsof.2008.09.005.

[46] C. Szegedy, W. Liu, Y. Jia, P. Sermanet, S. Reed, D. Anguelov, D. Erhan, V. Vanhoucke, A. Rabinovich, Going Deeper with Convolutions, (2014). https://doi.org/10.48550/ARXIV.1409.4842.

[47] K. He, X. Zhang, S. Ren, J. Sun, Deep Residual Learning for Image Recognition, (2015). http://arxiv.org/abs/1512.03385 (accessed July 18, 2023).
[48] S. Ren, K. He, R. Girshick, J. Sun, Faster R-CNN: Towards Real-Time Object Detection with Region Proposal Networks, (2016). http://arxiv.org/abs/1506.01497 (accessed July 18, 2023).
[49] Yue Zhang, Xinxiang Zhang, Effective real-scenario Video Copy Detection, in: 2016 23rd International Conference on Pattern Recognition (ICPR), IEEE, Cancun, 2016: pp. 3951–3956. https://doi.org/10.1109/ICPR.2016.7900252.
[50] X. Yang, H. Li, Y. Yu, X. Luo, T. Huang, X. Yang, Automatic Pixel-Level Crack Detection and Measurement Using Fully Convolutional Network, Computer Aided Civil Eng 33 (2018) 1090–1109. https://doi.org/10.1111/mice.12412.
[51] K. He, G. Gkioxari, P. Dollár, R. Girshick, Mask R-CNN, (2018). http://arxiv.org/abs/1703.06870 (accessed November 29, 2023).
[52] N. Gehri, J. Mata-Falcón, W. Kaufmann, Automated crack detection and measurement based on digital image correlation, Construction and Building Materials 256 (2020) 119383. https://doi.org/10.1016/j.conbuildmat.2020.119383.
[53] G. Lemaire, G. Escadeillas, E. Ringot, Evaluating concrete surfaces using an image analysis process, Construction and Building Materials 19 (2005) 604–611. https://doi.org/10.1016/j.conbuildmat.2005.01.025.
[54] L.F.M. Sanchez, B. Fournier, M. Jolin, D. Mitchell, J. Bastien, Overall assessment of Alkali-Aggregate Reaction (AAR) in concretes presenting different strengths and incorporating a wide range of reactive aggregate types and natures, Cement and Concrete Research 93 (2017) 17–31. https://doi.org/10.1016/j.cemconres.2016.12.001.
[55] Md.A.-M. Khan, S.-H. Kee, A.-S.K. Pathan, A.-A. Nahid, Image Processing Techniques for Concrete Crack Detection: A Scientometrics Literature Review, Remote Sensing 15 (2023) 2400. https://doi.org/10.3390/rs15092400.
[56] C. ASTM, Standard test method for concrete aggregates by determination of length change of concrete due to alkali-silica reaction, (1995). https://doi.org/10.1520/C1293-20A.
[57] Rasband, W.S, Image J, (1997). https://imagej.nih.gov/ij/.
[58] O. Stankiewicz, G. Lafruit, M. Domański, Multiview video: Acquisition, processing, compression, and virtual view rendering, in: Academic Press Library in Signal Processing, Volume 6, Elsevier, 2018: pp. 3–74. https://doi.org/10.1016/B978-0-12-811889-4.00001-4.
[59] I. Culjak, D. Abram, T. Pribanic, H. Dzapo, M. Cifrek, A brief introduction to OpenCV, (n.d.).
[60] Z. Zhang, A flexible new technique for camera calibration, IEEE Trans. Pattern Anal. Machine Intell. 22 (2000) 1330–1334. https://doi.org/10.1109/34.888718.
[61] GIMP, (2019). https://www.gimp.org.

APPENDIX

Appendix A

3D Print source of tools for image acquisition:

3D Printable Portable Reference Frame 25cm x 25 cm, available at:

https://drive.google.com/file/d/1SY6waz4NGDjgIGVcNC9s7uf2V8YjAcoa/view?usp=drive_link

3D Printable Perspective mitigation Frame, available at:
https://drive.google.com/file/d/1Zawj6utxADef3Rm1am23Ib3fIPmPPJn_/view?usp=drive_link

Appendix B.1

Sample CI results collected by operator 1 (Block B2D21, Segment 1).

B2D21(Operator 1)											
SQ1		Side A	Base length (m)		0.25	Side B					
Square Method						Square Method					
Interval	OA	BC	OB	AC		Interval	OA	BC	OB	AC	Total
1		0.40				1	1.00	0.80			
2	1.00	0.15				2			0.30		
3			0.10			3					
4						4		0.10			
5				0.20		5			0.10		
6	0.10	0.60				6					
7	0.20			0.10		7		0.80			
8			0.10			8	0.25		0.60		
9				0.10		9				0.15	
10						10					
Max width.	1.00	0.60	0.10	0.20	1.00	Max width.	1.00	0.80	0.60	0.15	1.00
Sum	1.30	1.15	0.20	0.40	3.05	Sum	1.25	1.70	1.00	0.15	4.10
mm/m	5.20	4.60	0.80	1.60	12.20	mm/m	5.00	6.80	4.00	0.60	16.40
Cracks	3	3	2	3	11	Cracks	2	3	3	1	9
Avg/Crcak	0.43	0.38	0.10	0.13	1.05	Avg/Crcak	0.63	0.57	0.33	0.15	1.68
C.I.	4.90		1.20		6.10	C.I.	5.90		2.30		8.20
EXP %	0.82		0.24		0.53	EXP %	1.18		0.58		0.88

Sample CI results collected by operator 2 (Block B2D21, Segment 1).

B2D21(Operator 2)											
Side A			Base length (m)		0.25	Side B					
Square Method						Square Method					
Interval	OA	BC	OB	AC		Interval	OA	BC	OB	AC	Total
1		0.40				1	1.00	0.80			
2	1.00	0.15				2			0.30		
3			0.10			3					
4						4	0.10	0.10			
5				0.20		5			0.10		
6	0.10	0.60				6					
7	0.20			0.10		7		0.80		0.10	
8			0.10			8	0.20		0.60		
9				0.10		9				0.20	
10						10					
Max width.	1.00	0.60	0.10	0.20	1.00	Max width.	1.00	0.80	0.60	0.20	1.00
Sum	1.30	1.15	0.20	0.40	3.05	Sum	1.30	1.70	1.00	0.30	4.30
mm/m	5.20	4.60	0.80	1.60	12.20	mm/m	5.20	6.80	4.00	1.20	17.20
Cracks	3	3	2	3	11	Cracks	3	3	3	2	11
Avg/Crcak	0.43	0.38	0.10	0.13	1.05	Avg/Crcak	0.43	0.57	0.33	0.15	1.48
C.I.	4.90		1.20		6.10	C.I.	6.00		2.60		8.60
EXP %	0.82		0.24		0.53	EXP %	1.00		0.52		0.76

Average CI result (B2D21) by 2 operators with expansion level calculated.

B2D21A						
image#	1	2	3	4	5	6
Ave. Horizontal	4.90	4.60	4.60	4.80	1.80	3.60
Ave. Vertical	1.20	2.70	1.80	0.45	1.10	1.45
Expansion % Horizontal	0.82	0.66	0.92	1.20	0.36	0.72
Expansion % Vertical	0.24	0.45	0.36	0.45	0.22	0.24

B2D21B						
image#	1	2	3	4	5	6
Ave. Horizontal	5.95	3.50	5.75	3.70	3.70	4.55
Ave. Vertical	2.45	2.00	1.00	0.50	0.75	0.30
Expansion % Horizontal	1.09	0.41	0.96	1.53	0.62	0.91
Expansion % Vertical	0.55	0.83	0.29	0.25	0.30	0.30

Appendix B.2

Crack orientation distribution diagram for block B2D21(2D-SP), B12 (1D-SP), B2D29(2D-TX)

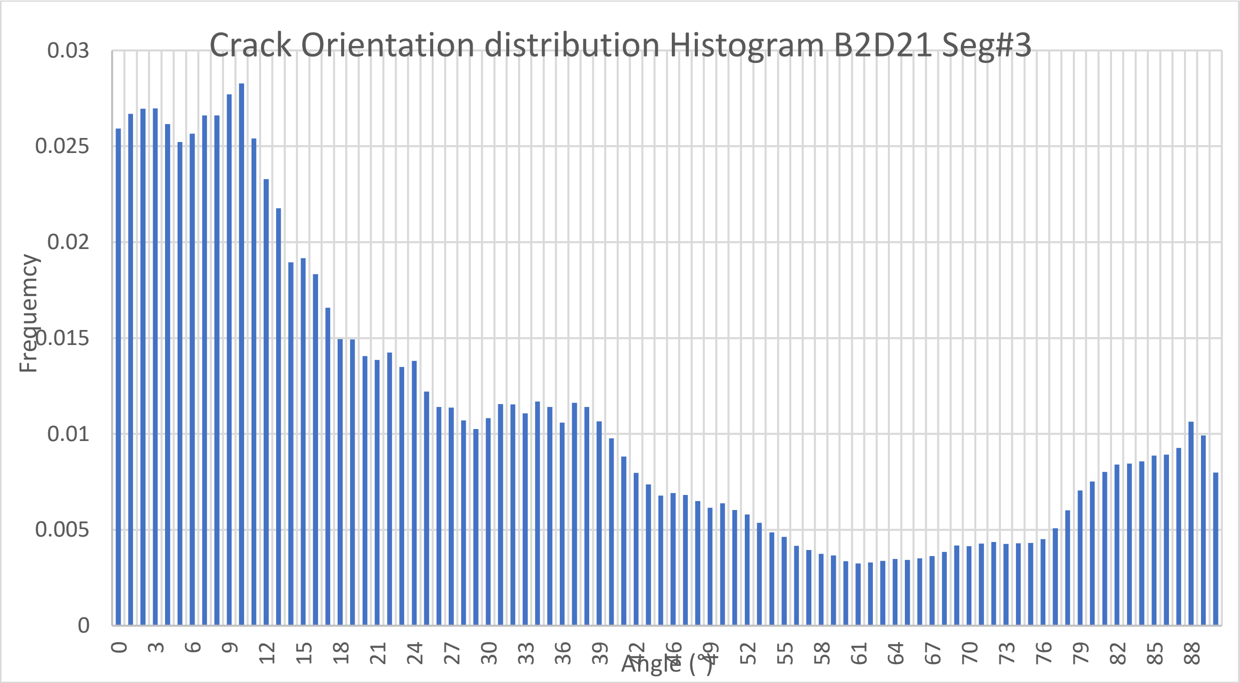

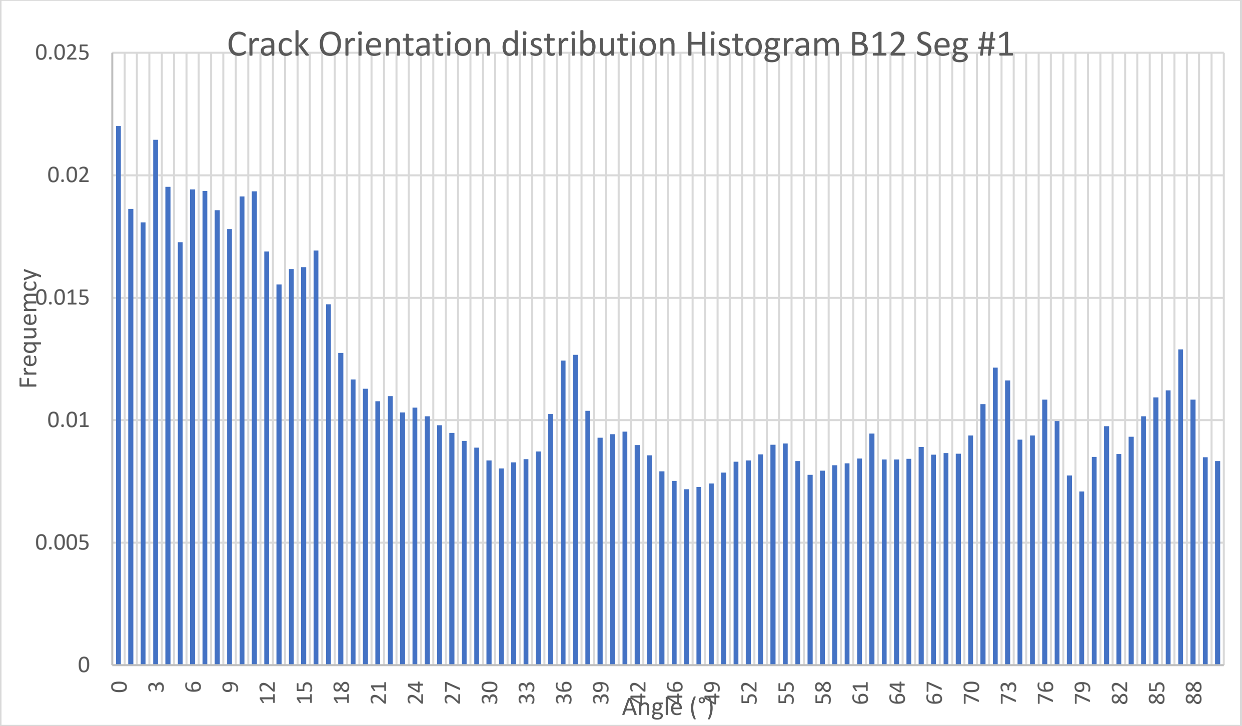

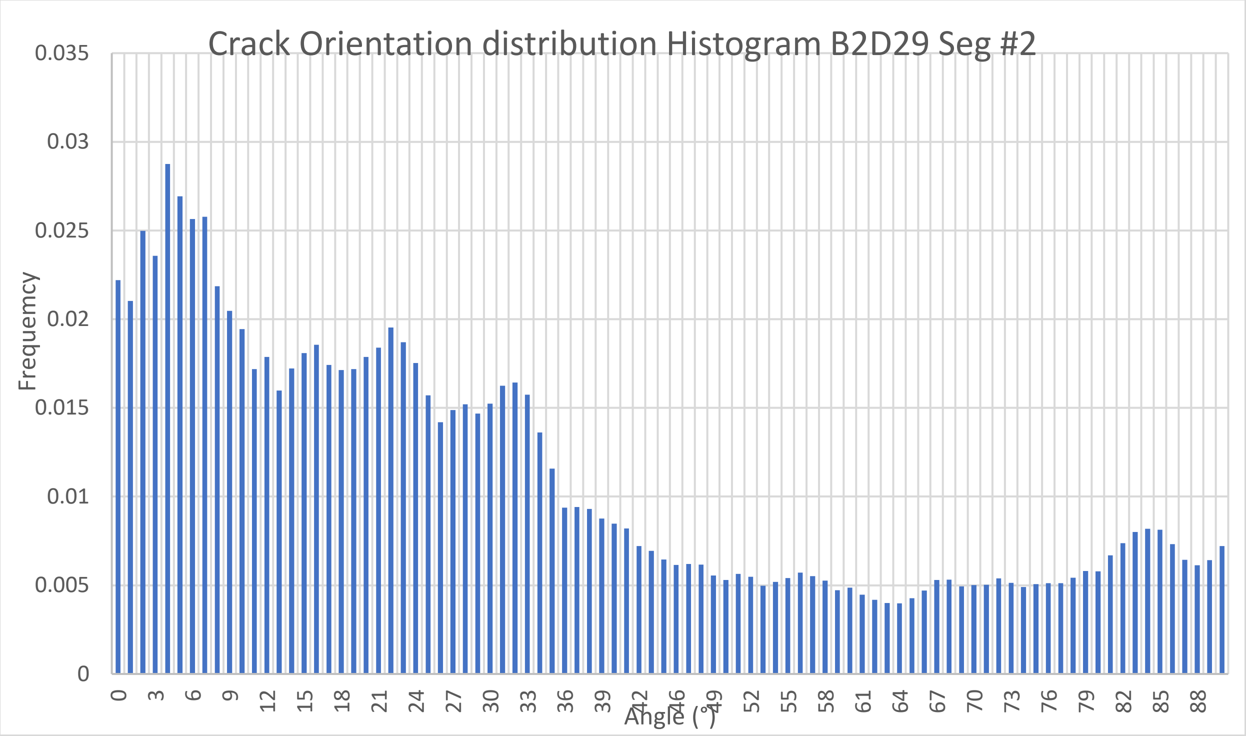
Crack Orientation distribution Histogram B2D29 Seg #2
0.035
0.03
0.025
0.02
0.015
0.01
0.005
0
Frequemcy
0
3
6
9
12
15
18
21
24
27
30
33
36
39
42
46
49
52
55
58
61
64
67
70
73
76
79
82
85
88
Angle (°)

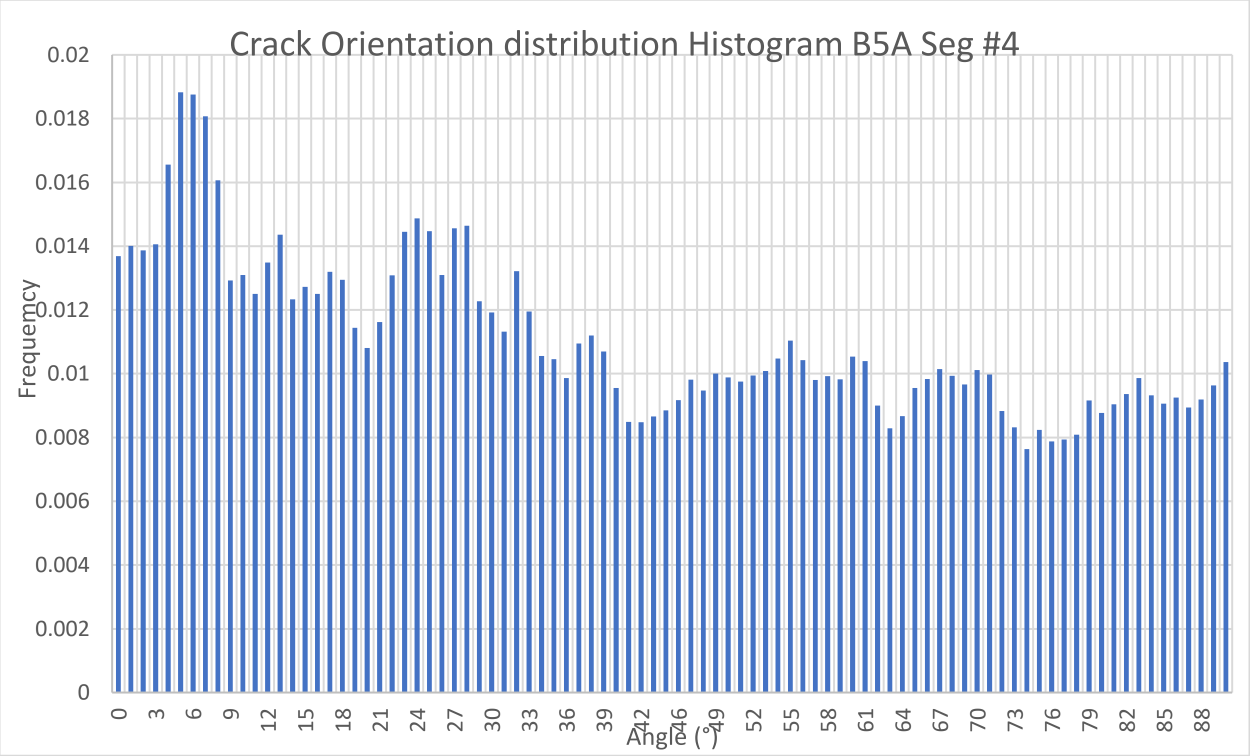
Crack Orientation distribution Histogram B5A Seg #4
0.02
0.018
0.016
0.014
0.012
0.01
0.008
0.006
0.004
0.002
0
Frequemcy
0
3
6
9
12
15
18
21
24
27
30
33
36
39
42
46
49
52
55
58
61
64
67
70
73
76
79
82
85
88
Angle (°)

Appendix C

Coefficient of CI predictions from crack characteristics (TCL x Orientation Angle)

	Angle	15	30	45	60	75	90	TCL*Ori(V)	TCL*Ori(H)
B2D21	1	0.210	0.234	0.221	0.172	0.080	0.083	1.471	0.541
	2	0.216	0.189	0.161	0.109	0.163	0.162	1.308	1.049
	3	0.382	0.209	0.153	0.078	0.058	0.119	1.765	0.528
	4	0.243	0.200	0.223	0.092	0.102	0.140	1.386	0.754
	5	0.221	0.146	0.136	0.107	0.206	0.184	1.080	1.146
	6	0.217	0.229	0.199	0.140	0.120	0.095	1.409	0.679
B2D29	1	0.278	0.153	0.130	0.126	0.125	0.189	1.788	1.300
	2	0.329	0.255	0.163	0.082	0.072	0.099	2.150	0.629
	3	0.250	0.240	0.149	0.118	0.121	0.122	2.171	1.078
	4	0.239	0.230	0.183	0.137	0.121	0.089	1.849	0.831
	5	0.288	0.232	0.177	0.108	0.100	0.094	2.245	0.841
	6	0.292	0.194	0.147	0.125	0.120	0.123	2.272	1.135
B12	1	0.279	0.174	0.141	0.121	0.140	0.145	1.473	0.927
	2	0.271	0.179	0.141	0.164	0.138	0.107	1.451	0.790
	3	0.283	0.241	0.168	0.123	0.092	0.092	1.468	0.515

	4	0.151	0.152	0.177	0.216	0.158	0.145	0.871	0.871
	5	0.165	0.170	0.202	0.154	0.146	0.162	1.018	0.938
	6	0.229	0.189	0.156	0.162	0.145	0.119	1.255	0.792
B5	1	0.193	0.205	0.124	0.223	0.187	0.185	1.097	1.026
	2	0.161	0.163	0.121	0.197	0.162	0.159	0.980	0.972
	3	0.145	0.125	0.106	0.156	0.171	0.131	0.925	1.036
	4	0.129	0.127	0.129	0.150	0.172	0.136	0.679	0.814
	5	0.177	0.175	0.219	0.139	0.146	0.180	1.147	1.065
	6	0.195	0.205	0.301	0.136	0.162	0.208	1.755	1.622